STREAMLINING THE DESIGN AND USE OF ARRAY COILS FOR IN VIVO MAGNETIC RESONANCE IMAGING OF SMALL ANIMALS

A Dissertation

by

WEN-YANG CHIANG

Submitted to the Office of Graduate and Professional Studies of
Texas A&M University
in partial fulfillment of the requirements for the degree of

DOCTOR OF PHILOSOPHY

Chair of Committee,	Mary Preston McDougall
Committee Members,	Steven M. Wright
	Jim X. Ji
	Kenith E. Meissner
Head of Department,	Anthony Guiseppi-Elie

August 2017

Major Subject: Biomedical Engineering

ABSTRACT

Small-animal models such as rodents and non-human primates play an important pre-clinical role in the study of human disease, with particular application to cancer, cardiovascular, and neuroscience models. To study these animal models, magnetic resonance imaging (MRI) is advantageous as a non-invasive technique due to its versatile contrast mechanisms, large and flexible field of view, and straightforward comparison/translation to human applications. However, signal-to-noise ratio (SNR) limits the practicality of achieving the high-resolution necessary to image the smaller features of animals in an amount of time suitable for *in vivo* animal MRI. In human MRI, it is standard to achieve an increase in SNR through the use of array coils; however, the design, construction, and use of array coils for animal imaging remains challenging due to copper-loss related issues from small array elements and design complexities of incorporating multiple elements and associated array hardware in a limited space. In this work, a streamlined strategy for animal coil array design, construction, and use is presented and the use for multiple animal models is demonstrated. New matching network circuits, materials, assembly techniques, body-restraining systems and integrated mechanical designs are demonstrated for streamlining high-resolution MRI of both anesthetized and awake animals. The increased SNR achieved with the arrays is shown to enable high-resolution *in vivo* imaging of mice and common marmosets with a reduced time for experimental setup.

For my parents, Tai-Chung Jiang and Yuan-Ning Fong

ACKNOWLEDGEMENTS

Foremost, I would like to express my sincere gratitude to my advisor Dr. Mary McDougall for the support of my PhD study. Her guidance has helped to motivate my research and writing this thesis. And, I cannot find words to express my gratitude to Dr. Afonso Silva who gives me mentorship and encourages me to learn and develop freely in National Institutes of Health (NIH).

I would like to thank Dr. Steven Wright who shares his immense knowledge with me and has helped with my research throughout the years. In addition, thank you to Dr. Jim Ji and Dr. Kenith Meissner for their encouragement, insightful comments and hard questions given in my proposal exam.

My sincere thanks also goes to Dr. Joseph Murphy-Boesch, Dr. Chern-Chyi (Cecil) Yen, Dr. Stephen Dodd, Dr. Hellmut Merkle and Dr. Vincent Gresham, for their support in hardware designs and animal experiments. My research would have been impossible without their help and mentorship.

I offer my regards and blessings to all of my fellow friends and colleagues in TAMU and NIH for brainstorming and helping with my experiments: Dr. Joseph Rispoli, Dr. Edwin Eigenbrodt, Dr. John Bosshard, Dr. Jiaming Cui, Dr. Neal Hollingsworth, Dr. Daniel Papoti, Dr. Pascal Sati, Dr. Daniel Reich, Kurt Parizek, Stephen Ogier, Jennifer Lefeurve and Nicholas Luciano.

Finally, I would like to thank my wife, Kathryn Brinkman, for her encouragement, incredible patience and help in every aspect. Last but not least, I owe my deepest gratitude to my parents Tai-Chung Jiang (姜泰忠) and Yuan-Ning Fong (馮淵寧) for their support and encouragement throughout my life, and letting me pursue my dreams. Thank you, papa and mama.

CONTRIBUTORS AND FUNDING SOURCES

Contributors

This work was supervised by a dissertation committee consisting of Professors Mary P. McDougall (Chair of Committee) and Kenith E. Meissner of the Department of Biomedical Engineering, Professors Steven M. Wright and Jim X. Ji of the Department of Electrical Engineering and Professor Afonso C. Silva of Cerebral Microcirculation Section (CMS), National Institute of Neurological Disorders and Stroke (NINDS), National Institutes of Health (NIH).

The MRI data in Chapter V was provided by Dr. Chern-Chyi (Cecil) Yen (CMS, NINDS, NIH). The program that generated g-factor maps in Chapter V was modified from Felix A. Breuer's previous work. The MRI data in Chapter VI was provided by people from NIH: Dr. Chern-Chyi (Cecil) Yen and Jennifer A. Lefeuvre. The marmoset phantom presented in Chapter VI was partially developed by Nicholas J. Luciano. The 4-element loop coil array mentioned in Chapter 6 was developed by Hellmut Merkle.

All other work conducted for the dissertation was completed by the student independently.

Funding Sources

Graduate study was supported by fellowships from American Heart Association (Grant Number 0930231N), Texas A&M University (assistantship) and National Institutes of Health (IRTA Pre-doctorial Traineeship and Pre-doctorial Visiting Fellowship).

The works in Chapter III and Chapter IV were made possible in part by American Heart Association under Grant Number 0930231N.

NOMENCLATURE

2D	2-dimensional
3D	3-dimensional
3T	Compound adjective indicating B_0 = 3 Tesla
4.7T	Compound adjective indicating B_0 = 4.7 Tesla
7T	Compound adjective indicating B_0 = 7 Tesla
ACUC	Animal Care and Use Committee
A-P	Anterior-posterior
B_0	Static magnetic flux density
B_1	RF magnetic flux density
C	Capacitance/capacitor
CAD	Computer-aided design
CNC	Computer numerical control
DTI	Diffusion tensor imaging
DC	Direct current
DPP	Dual plane pair
DPPX	Dual plane pair with crisscrossed return paths
ECG	Electrocardiogram
fMRI	Functional MRI
FLASH	Fast low angle shot
FOV	Field of view

GND	Ground
GRAPPA	Generalized autocalibrating partially parallel acquisition
IACUC	Institutional Animal Care and Use Committee
ID	Inner diameter
L	Inductance/inductor
L-R	left-right
MR	Magnetic resonance
MRI	Magnetic resonance imaging
NEX	Number of excitation
NIH	National Institutes of Health
NMR	Nuclear magnetic resonance
OD	Outer diameter
PCB	Printed circuit board
PLA	Polylactic acid
PVA	Polyvinyl alcohol
Q	Quality factor
R	Resistance/resistor
RARE	Rapid acquisition with relaxation enhancement
RF	Radio frequency
RFC	RF choke
Rx	Receiving
S_{11}	S-parameter: Return loss

S_{21}	S-parameter: Power transferred from Port 1 to Port 2
SCI	Spinal cord injury
SENSE	Sensitivity encoding
SMASH	Simultaneous acquisition of spatial harmonics
SNR	Signal-to-noise ratio
T1	Spin-lattice/longitudinal relaxation time
T2	Spin-spin/transverse relaxation time
TAMU	Texas A&M University
TE	Echo time
TR	Repetition time
Tx	Transmitting
V	Voltage

TABLE OF CONTENTS

Page

LIST OF FIGURES

Page

LIST OF TABLES

Page

CHAPTER I

INTRODUCTION

The importance of small-animal MRI

Magnetic resonance imaging (MRI) offers a variety of contrast mechanisms and versatile imaging functionalities that are powerful in scientific research both in human and animal studies. Furthermore, pre-clinical animal testing using MRI is irreplaceable in the studies that pose higher risks to the subjects, such as studies of disease, pharmacological development, treatments for malignancy and brain research.

When considering which animal model to use, small animals are often preferred over large animals as they have a larger litter size and a shorter time to maturity. They are also easier to breed, and more economical. Among small animals, mice play an important role as a long standing and widespread model for pre-clinical studies of human disease, with particular application to cancer [1], cardiovascular [2-6], pharmacological and surgical applications [7-9].

At the same time, methods have been developed which are sometimes better suited for use with non-human primates. The development of functional magnetic resonance imaging (fMRI) [10] in the last 20 years has become one of the most important tools in brain research [11]. While macaques are the major non-human primates used in neuroscience studies with fMRI [12-19], common marmosets (*Callithrix jacchus*), a type of New World monkey, are gaining popularity due to their features of smaller body size, shorter time to

maturity, shorter gestation period and easier breeding. Compared with mice, marmosets also have longer lifespans [20-29].

The importance of MRI in small animal imaging is significant due to the extensive and growing use of MRI in both traditional and newly studied small animal models. More importantly, designing MRI for small animal models needs to be streamlined in order to meet the ever changing needs of the research community.

The challenges of small-animal MRI

To study the above described animal models, magnetic resonance imaging (MRI) is advantageous as a non-invasive technique due to its versatile image contrast mechanisms, large and flexible field of view, and straightforward comparison/translation to human application. However, manipulating traditional human-based MRI techniques to work with small animal imaging presents several major challenges.

The first challenge: lower SNR

The signal-to-noise ratios (SNR) in MRI must be sufficiently high in order to be useful in diagnosis or research. However, there are five main reasons why MRI coil arrays for small animals suffer from lower SNR:

(1) Smaller voxel size: Voxel size is up to orders of magnitude smaller than typical human scans, and, unfortunately, SNR is proportional to the voxel size. For example, the signal received in mouse imaging is 4000-times weaker when the same morphological details are imaged in humans [30]. Averaging repeated

scans can be increased to compensate for this lower SNR. However, using this method alone would require 600 years of time in order to complete a mouse brain MRI that only takes around 20 minutes in humans.

(2) Resistive loss: Every electronic component of a coil has a certain amount of resistive loss. The resistive loss of a conductor is inversely proportional to the cross-sectional area, i.e. a smaller wire, often used in small animal coil arrays, has higher resistive loss. The resistive loss of inductors is measured by Q, whereby the lower the value, the more resistive loss. Generally, inductors of small form-factor have lower Q values. For example, for inductors of similar inductance made by Coilcraft, the Q value of the micro series 0806SQ-19N (typical size used for small animal coils) is 90 and the Q value of the Unicoil 5-mm tunable 164-01A06L with no core (typical size used for human coils) is 145.

(3) Eddy-current loss: In addition to inherent resistive loss, a conductor also experiences eddy-current loss raised from the surrounding conductive structures. While it is true that increasing the size of a conductor reduces resistive loss, larger conductors experience more eddy-current losses in surrounding copper [31]. Small animal coil arrays face this dilemma, except worse (because the distance between conductors shortens quicker for smaller coils), which seeks for larger conductors to reduce resistive loss, yet not too large to prevent eddy-current loss in an “already-too-crowded” situation. In addition, due to the limited size of pre-clinical MRI scanners for small animals,

the transmitting volume coil is usually very close to the receiving coil array. This not only makes decoupling between these two coils more difficult, but also raises eddy current losses.

(4) Coil coupling through mutual inductance: There are three potential concerns about coil coupling: correlated noise, change of coil tuning and inability for accelerated parallel imaging. In fact, modest coupling between coils does not affect image SNR when a noise covariance matrix is incorporated into the combination of array signals [32-35]. In addition, when coils are connected to low-input impedance amplifiers, slightly miss-tuned coils have very little effect on the signal level because of the nature of high-impedance measurement. However, when coils are miss-tuned too much, the impedance changes such that preamplifiers do not experience proper impedance for noise matching, and SNR degrades. Decoupling mechanisms include preamplifier decoupling, active detune traps and RF chokes (if self-resonance frequency is used). However, these mechanisms only work within small bandwidths. Therefore, excessive miss-tune exacerbates coupling between the receiving and transmitting coils. In this case, because noise in the preamplifier can project back into the coil, noise couples to other coils and this added noise shows up on the diagonal elements of the noise covariance matrix. Noise of these diagonal elements cannot be mitigated through the inclusion of the noise covariance matrix [36]. Therefore, geometric decoupling [37] is still necessary to reduce coupling between coil elements even when preamplifier decoupling

is used. Furthermore, better decoupling also means more independent coil sensitivity pattern which is crucial for accelerated parallel imaging. However, because geometric decoupling is determined by the ratio of the overlap and the size of the coil, the implementation of geometric decoupling on small-animal MRI coil arrays requires higher production accuracy and structural stability.

(5) Variation of individual size: Surface coil arrays are effective in terms of increasing SNR. Surface coils should be placed close to the subject for better SNR [37-40], but not too close to prevent the lift-off effect [41, 42]. Therefore, the array coil should follow the contour of the subject with constant and optimal distance to maximize SNR. However, it is difficult to optimize the surface coils for animals with various sizes, because it requires complex mechanical designs which usually take up lots of space that a small-animal MRI scanner does not have.

To summarize, when the coil size becomes smaller, the coil "sees" less body tissue, thus the received signal is weaker. The contribution of signal from each voxel is also smaller because the voxel size needs to be smaller to resolve enough anatomical information. At the same time, smaller coils have higher resistive loss from the conductor and inductor, and the proximity of receiving and transmitting coils increases the eddy-current loss as well. To estimate these effects on SNR, the ratio of losses of the sample versus the components is measured by unloaded to loaded Q ratio. Since $Q = \omega L/R$ for LCR circuits, it is easy to derive $R_{sample}/R_{component} = Q_{UL}/Q_L$ [43]. Usually, the Q ratio of small animal coils is significantly lower than that of human coils. In short, because the

components have higher loss and coils receives less MR signal due to smaller coil size, small animal coils suffer from significantly lower SNR.

The second challenge: complexity of experimental setup

The development of MRI coil arrays is a highly iterative process because of the interaction between high Q components arranged in close proximity. The dimension of the coil, tuning, noise matching, amount of geometric decoupling, preamplifier decoupling, active detune traps and cables traps are repeatedly adjusted on the fly throughout the entire development process. Scattering parameters (or S parameters) such as S_{11} and S_{21} measurements are repeatedly used to determine the amount of adjustments throughout the entire process as well.

Sharing the same iterative nature of coil development, the development of coil arrays for small-animal applications is even more challenging because small animal imaging often requires additional devices. This extra equipment heavily influences the decision making of the design of small-animal coils because the space available in animal MRI scanners is limited. Here is the list of major equipment required in small-animal MRI:

(1) Equipment for reducing motion artifacts: Body motion, cardiac motion and respiratory motion are the three major sources of motion artifacts in animal MRI. To reduce body motion, it is necessary to design an apparatus that makes the animal stay stationary. Common designs are bite bars, ear bars and cradles with straps for rodents. For non-human primates such as marmosets, more advanced designs are often needed. Cardiac motion of small animals is more challenging

than humans because of the higher heart rates (632 bpm for mouse [44] and 230 bpm for marmosets [45]). Part of this challenge can be mitigated by cardiac gating, which is usually done using electrocardiographic (ECG) detection, yet it results in other problems such as inconsistent T1/T2 contrasts. Unlike "breathe hold" which can be ordered during human MRI, the control of respiration artifact for animals is usually done by either respiration gating using respiration sensors, which consequently cause inconsistent T1/T2 contrasts as well, or ventilator assisted respiration gating—all of which add additional complexity to the experimental setup and change the design of the coil.

(2) Equipment for delivery of anesthesia: Anesthesia can help reduce motion artifacts as well as reduce stress to animals. However, anesthesia affects animals' physiology such as cardiovascular functions [46-54], neurovascular couplings (see [55-59] for reviews), and has other physiological effects [60-65]. Recent studies also report that anesthesia-free animals show stronger and faster hemodynamic responses [27, 66]. In short, the use of anesthetics is determined by the scientific problem in question, which influences the decision making of the coil designs.

(3) Equipment for animal safety: Routine anesthesia administered during animal surgery is generally safe. However, some fatality does occur, and many of the deaths are related to human errors, such as lack of close observation [67]. Therefore, monitoring physiological status when anesthesia is administered is very important. A temperature control device is commonly used to prevent hypothermia. Usually, either hot air blown over the subject or a water jacket is

used during MRI scans. Hand warmers are dangerous and should be prohibited in MRI scanners, and electrically heated mats should also be avoided because of its potential safety issues inside of MRI scanners. The physiology signals such as heart rate, respiration, blood pressure, oxygen level, carbon dioxide level, etc., are constantly monitored during MRI scans. ECG electrodes and an air pressure cushion are usually used for monitoring heart and respiration rates, respectively. However, different research facilities have different arrangements for these equipment and different scanners have different bore sizes. As a result, the routing of cables and tubes are arranged in uniquely different ways from one research facility to the other. Therefore, because the arrangement heavily influence the design of the coils and the experimental setups, coils that work in one research lab do not necessarily work in the other.

All of the equipment stated above, along with the coils, need to fit inside of an MRI scanner. However, MRI scanners for small animals do not have the luxury of ample available space that is found in MRI scanners made for human. In addition to the challenge of hardware design, setting up an animal MRI scan is not only more complicated but also more time consuming. Finally, complicated experimental setup not only increases the chance of failure mode, long experimental setup time also raises safety concerns because animals spend more time under anesthesia.

Streamlined design as a solution for small-animal MRI

While the magnetic field of a MRI scanner is usually predetermined and increasing repetition scans is limited in *in vivo* imaging, improving SNR through specialized probes, such as coil arrays, seems to be more available. However, extra equipment required for small-animal MRI not only adds complexity to the coil design but also hinders the experimental setup. In order to fit all of the equipment into a space-limited scanner, the choice of equipment changes the design of the small-animal coils. To properly address all the challenges stated above, two major design philosophies were considered:

(1) Systematic design approach: When designing massively parallel human coil arrays, it is advised to design the array in a systematic way which facilitates the construction and testing [43]. Even the final steps of the array construction need to be considered in the very beginning of the design phase.

(2) Effective user interface: As a general guideline for designing medical devices [68], a good interface design ensures effectiveness, efficiency, and reduced human error which is important in quality assurance programs.

In this work, a streamlined approach was used to develop coil arrays within space limitations, necessary equipment, routing of cables and tubes and workflow of experimental setup all planned as one system in the beginning of the design phase. Computer-aided design (CAD) software, 3D printing and smaller scale prototypes were used to validate the clearance, coil performance and experimental setup prior to the full-scale hardware implementation. New materials, components, assembly techniques and

tools were used to streamline the development process of the hardware and reduce the complexity of the experimental setup in order to meet all the specifications and to achieve the ultimate goal of answering scientific questions.

Scope and dissertation chapters

The objective of this doctoral research was to explore small animal RF array coil designs for different scientific problems in question. The goal is to develop a new approach, highlighting streamlined designs, to improve the efficiency of high-resolution animal MRI scans. To this end, the animal coil designs should have the following features: 1) enable high SNR (to be exploited for improved resolution and/or scan time), 2) have appropriate animal-restraining mechanisms to reduce motion and help obtain reproducible results, 3) be easy to use with integrated life support and monitoring devices, 4) be easy to clean to prevent contamination, and 5) be robust with mechanically-stable coil formers and proper cable management.

This dissertation continues in the following form:

- Chapter II contains a literature survey of existing techniques used in animal MRI coils. The decision-making of using anesthetics is also briefly reviewed in this chapter.

- Chapter III describes a novel receive coil array with a compressible coil former for mouse imaging to address the issues of coil coupling and size variation of mice.

- Chapter IV describes a streamlined design approach for implementing a 6-channel, general-purpose mouse array coil.

- Chapter V presents the application of this streamlined design approach to a 10-channel head array for awake marmoset imaging and

- Chapter VI describes a 12-channel spine array for anesthetized marmoset imaging.

- Chapter VII summarizes the streamlined design strategy and enabling tools used in this dissertation.

- Chapter VIII contains conclusions and future work.

CHAPTER II

BACKGROUND

A successful small-animal MRI coil should be built to reduce preparation time before scans, and to reduce the time required for the MRI scan itself. The former is important because it reduces the exposure of anesthesia to the animal, and can be done through innovative mechanical designs. The latter is even more important because some studies require high temporal resolution to capture dynamic contrasts, such as blood flow in MR angiography and hemodynamics in fMRI. Various parallel imaging techniques have been developed to accelerate the imaging speed of MRI, and this is generally achieved by the combination of receiving array coils and/or special MRI pulse sequence designs. In this chapter, the effects of anesthesia on small animals are briefly reviewed in "Anesthesia, animal physiology and the effects on coil design" section, followed by the review of current coil designs for mice and marmosets in "Coil design technology: the birdcage coil" and "Coil design strategy: coil array and small-animal imaging in mouse and marmoset applications" sections, and finally the basis of parallel imaging techniques is reviewed in "MRI technology: parallel imaging techniques" section.

Anesthesia, animal physiology and the effects on coil design

Anesthesia is commonly used in animal studies to minimize motion artifacts as well as reduce stress to the animals. Although the death rate introduced by anesthesia is low, some studies show that general anesthetics can cause neurotoxicity, especially for young subjects or when excessive dosage is used [67, 69-71]. Routine anesthesia administered

during animal surgery is generally safe. However, some fatality does occur, and many of the deaths are related to human errors, such as lack of close observation [67]. Therefore, monitoring physiological status when anesthesia is administered is very important.

The need for anesthesia also depends on the methodology and science in question [59, 72, 73], and this is because different anesthetics have different temporal and spatial effects on cardiovascular functions [46-54], neurovascular couplings (see [55-59] for reviews), and other effects [60-65]. Recent studies also show that animals have stronger and faster hemodynamic responses in the awake condition [27, 66].

Although awake animals show higher response to external stimulation, awake animal studies are very challenging because data is susceptible to motion artifacts, restraint-related stress/discomfort, and environmental conditions [74, 75]. To reduce artifacts, it is necessary to combine innovative mechanical designs and animal training when anesthesia is not used [27, 74-78].

The following sections will review well-established coil design terminology and technology that will be employed in the rest of this work.

Coil design technology: the birdcage coil

A homogenous B_1 field is usually desirable for medical diagnosis and accuracy in imaging and spectroscopy applications. Hayes introduced the birdcage coil in the mid-80s [79, 80]. For the next decade, it became the go-to coil for imaging and spectroscopy because of its highly homogenous B_1 field—even after Roemer proposed the application of phased array

coils in the mid-90s [37]. A birdcage coil can be seen as a resonant structure built by a series of lumped elements as a balanced delay line on a cylindrical surface. The structure of a birdcage coil consists of two circular conducting loops, parallel to each other, with multiple conducting rungs connected in between. The conducting loops are usually referred to as "end rings" and the conducting rungs are sometimes referred to as "legs" or "rungs." To further explain how a birdcage coil works, it is easier to consider the structure of a birdcage coil as repetitive meshes inductively (low pass) or capacitively (high pass) coupled with adjacent elements. Therefore, it is also convenient to treat a birdcage coil as a periodic structure that represents a transmission line with finite phase shift from each mesh. In addition to the linear mode, the efficiency of a birdcage coil can also be improved by operating it on the quadrature mode. Although birdcage coils have these desirable features, predicting the resonance frequency systematically and easing the design process remained to be improved. Vullo [81] and Tropp [82] propose practical design procedures to help in designing birdcage coils. While it is possible to predict the resonance frequency of a birdcage coil using three-dimensional numerical simulations, Leifer [83] demonstrated the quasi-static approach to predict the resonant and the spatial modes of a birdcage coil. His work is important for designing a birdcage coil because his approach is applicable and accurate enough for both high-pass and low-pass birdcage coils with or without a shield. His approach is also easier to understand and correlate with practical design procedures than simulation-based approaches.

Chin *et al*. published the BirdcageBuilder program [84] and introduced this easy-to-use tool to the community of coil engineers. BirdcageBuilder can calculate the values of

lumped elements based on the dimension of the coil, type of coil (high-pass, low-pass or band-pass) and with/without shield. The BirdcageBuilder program is now available both online and offline.

Coil design strategy: coil array and small-animal imaging in mouse and marmoset applications

The first major challenge to address is the inherent lower SNR due to the small size of a mouse. To offset the 4000-time weaker signal produced in mouse imaging [30], SNR can be enhanced by scan repetitions/averages, higher magnetic fields and specialized probes [85]. However, the number of averages is limited in *in vivo* mouse imaging due to safety concern with extended exposure of anesthesia, especially for diseased mouse models. As the magnetic field of a scanner is usually predetermined and increasing repetition scans is limited in *in vivo* imaging, improving SNR through specialized probes remains an area of opportunity/freedom. Decreasing the size of an RF coil increases local sensitivity where it is close to the coil [85, 86]. Furthermore, when an array of small coils is used, it is possible to cover a larger area of interest and keep high SNR. However, while the imaging depth can be maintained by array design [40], the copper loss (the resistive loss of the conductor itself and eddy-current loss of neighboring conductive components) and shielding effect [31, 87] still limits the minimal size of the loop coils.

Higher heart and respiratory rates, presents a huge concern for *in vivo* mouse MRI in terms of motion artifacts. When motion occurs during the readout gradient, motion-blur rings are introduced in the image [88]. If motion occurs between phase-encoding steps, ghost

artifacts are introduced along the phase-encoding direction in the image [89]. To reduce the level of motion artifacts, a common solution is using the double gating technique. This technique uses blanking during respiration and only sends the trigger signal to the MR scanner when the predetermined cardiac phase is detected. In *in vivo* mouse MRI, cardiac gating is usually done by electrocardiographic (ECG) detection. As for respiratory gating, it can be done directly using additional hardware [90-101] or indirectly using additional acquired MR signal either in real-time or post-processing [90-103].

In addition to the two major challenges stated above, *in vivo* mouse imaging also requires different kinds of fabrication techniques to miniaturize the coil and related systems. Furthermore, as the dimensions of the coils get smaller, the consideration of sample-noise-dominance might pose a limitation to certain types of coil designs. For routine *in vivo* mouse imaging, enabling the use of animal protocols and software also needs to be considered from the early stages of the design process.

Individual technology advancements, which were mentioned above, have made fast mouse MR imaging possible. Several groups have reported work of array coils for imaging mice on clinical scanners as well as high-field animal systems [104-110]. However, the development of high performance coil arrays remains painfully time consuming, and little attention has been made on the user interface which simplifies the experimental setup.

MRI array coils for common marmosets are still a new area of development in animal MR imaging. As a relatively new animal model, in contrast to mice, very few array coils are reported for common marmosets [111, 112]. Common marmoset coils share similar

technological challenges of other small-animal coils. When anesthetized, the heart rate of common marmosets is usually 200-250 beats/min [113], which still poses a challenge for cardiovascular and spinal imaging. Currently, the use of common marmosets is focused on brain studies, and MRI array coils for awake marmosets are the most desirable. To this end, specialized mechanical designs need to be integrated into the array coil to ensure reproducible results.

MRI technology: parallel imaging techniques

Although MRI provides adjustable soft-tissue contrast noninvasively, a long scan time has always been considered a limitation of MRI. Compared with computer tomography (CT) and ultrasound, the imaging speed of clinical MRI is calculated in terms of minutes. This disadvantage not only makes MRI scans uncomfortable for certain patients, it also limits certain applications which focus on organs that move (such as the heart) and contrast that changes (such as flowing blood in angiography). Some sequences allow for a short TR, such as balanced steady-state free-precession, but require strong gradient amplifiers to alter the magnetic field gradient rapidly. A rapidly changing magnetic field also causes a physiological problem because it can induces an eddy current that stimulates peripheral nerves [114-116]. Finally, fast multi-echo sequences, such as fast spin echo, introduce much concern in specific absorption rate (SAR) which limits the shortest TR for *in vivo* imaging [117].

Fortunately, parallel imaging techniques which accelerate imaging speed can mitigate these problems. By combining an array coil and image reconstruction, parallel imaging

not only shortens the scan time or increases spatial/temporal resolution, it also makes heart, MR angiography and many other applications feasible. Parallel imaging techniques are generally categorized as image-domain techniques (such as sensitivity encoding, SENSE [35]) and k-space approach (such as simultaneous acquisition of spatial harmonics, SMASH [118] and generalized autocalibrating partially parallel acquisitions, GRAPPA [119]).

As a Fourier modality, MRI data is acquired in k-space which contains spatial frequency information of the final image, and the final image is calculated through the Fourier transformation of k-space data. To accelerate MRI, therefore, parallel imaging techniques accelerate imaging time by undersampling the acquisition of full k-space data, and reconstruct final images with the additional information provided by array coils. In SENSE, the sensitivity patterns of array coils are used to estimate alias-free images in an image domain. In GRAPPA, an autocalibration signal (ACS) is used to estimate the skipped k-space data, and the alias-free image is reconstructed through Fourier transform of the estimated full k-space data. GRAPPA is considered to be the more robust approach in cases where the sensitivity map is difficult to estimate due to lower signal in lung and sinus areas. The GRAPPA approach is also more suitable for subjects which are more susceptible to motion.

For SENSE, the signal-to-noise ratio (SNR) is defined as:

$$SNR_{PI} = \frac{SNR}{g\sqrt{R}}$$

Where R is the acceleration factor and g is the coil geometry factor, or "g-factor" in short. Acceleration factor means R-times fewer data is acquired. G-factor relates to the geometry of the receiver array and the correlation between array coils. G-factor is always greater or equal to one, and g-factor is larger in areas where the sensitivity of each coil is correlated. Usually, the g-factor is higher at the center of the subject where the coil sensitivity pattern is the most similar. This is also the reason that the accelerated image shows lower SNR at the center of the subject.

When MRI is accelerated through GRAPPA, the SNR can be estimated in the same way that SENSE does. The GRAPPA g-factor, though, is calculated differently from SENSE. The SENSE g-factor is derived from the coil sensitivity profile, and the GRAPPA g-factor is derived from the GRAPPA weights. Although SENSE and GRAPPA g-factors are derived differently, they are usually similar because both factors originate from the coil sensitivities. That said, recently, it has been shown that GRAPPA g-factor can be improved by accelerating in two directions and offsetting k-space sampling points (CAIPIRINHA) [120, 121].

Summary of background and moving forward

Coming from the technology developed for human MRI, the building blocks—from coil array hardware to parallel imaging technology—are ready to tackle the challenges of lower SNR in small animal imaging. Gating, anesthesia delivery, life support and physiological monitoring devices are available to meet basic needs in small-animal MRI. However, as more array elements are used in the limited space inside an animal scanner, the fabrication

methods used on human coil arrays become increasingly challenging. During our investigation, we also found that coil circuits need to be modified in order to work properly in certain extreme conditions. Furthermore, when the size of coil elements approaches the scale of small animals, the difference of loading from one animal to another varies greatly, and this makes optimizing the SNR for one-size-fits-all coil arrays difficult. The complicated experimental setup of small-animal MRI experiments stems from the inability to communicate with animals. The complicated experimental setup not only increases the burden on lab personnel but also increases animal exposure to anesthesia leading to safety concerns.

The goal of this work is to bridge the technology gaps between human coil arrays and small-animal arrays. A streamlined design approach is proposed to facilitate the development of coil arrays using modified coil circuits, new materials and new assembly techniques. Through system-level integration, the experimental setup is also streamlined with reduced complexity.

CHAPTER III

GEOMETRIC DECOUPLING OF A MOUSE ARRAY COIL USING A DUAL PLANE PAIR DESIGN WITH CRISSCROSSED RETURN PATHS AND COMPRESSIBLE COIL FIXTURE*

Receive array coils traditionally employ a combination of active and/or passive detuning configurations in order to decouple from the transmit coil during transmit phase of the MRI sequence [37, 122]. However, in space limited situations, such as working with small bore systems or with array coils on small samples or animals, this requirement can be difficult to realize. Planar pair and dual-plane pair (DPP) coil designs can passively decouple coil elements from the transmit coil due to their counter-rotating flux paths on either side of the element [123]. Therefore, without the need for active detune circuits and PIN diode signal lines, the challenge relating to limited space is alleviated; however, we have noted that for certain element sizes, the loop mode of the receiving element can couple to the volume coil, independent from the imaging mode, and causes signal loss at the peripheral areas of the imaging subject.

This chapter presents a 10-channel array coil with an element design that uses a dual plane pair configuration with "crisscrossed" return paths (DPPX) as the receive element to

*© 2014 IEEE. Reprinted, with permission, from Wen-Yang Chiang and Mary P. McDougall. Geometric decoupling of a mouse array coil using a dual plane pair design with crisscrossed return paths and custom mounting fixture. Engineering in Medicine and Biology Society (EMBC), 36th Annual International Conference of the IEEE, August 2014.

geometrically decouple the array coils from the transmitting volume coil. An approach for an adjustable custom fixture is also described that allows the receive array to maintain close contact with varying sizes of mice while maintaining the decoupling condition in the transmit coil.

Materials and methods

Background of Dual Plane Pair with Crisscrossed Return Path (DPPX)

Our group previously has reported the ability of the DPP element to decouple from the transmit coil without any active detune network due to flux being induced in equal and opposite directions in the two halves of the coil [123], as is illustrated in Figure 1. During our investigation of applying the DPP coil array to mouse MRI, we found that the loop mode of the DPP coil formed by the return paths causes local signal loss due to coupling when the imaging subject is too close to the DPP array. We designed the DPPX array to alleviate this problem.

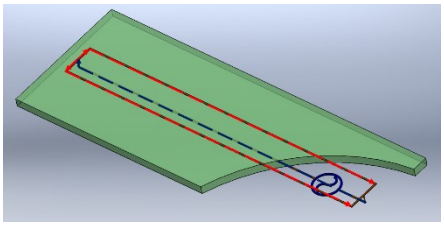

Figure 1. Conventional DPP coil and its static current flow.

Illustration of Loop Mode Effect

To illustrate the issue, we manufactured the traces-only (without lumped elements) of DPP-like coils with three different types of return paths: a conventional DPP coil, a DPP

coil with shorted return paths (intended to change the size of the loop coupling to the transmit field), and a DPPX coil. The trace-only coils with different return paths are shown in Figure 2. We placed each type of trace under a cylindrical $CuSO_4$ phantom and imaged each assembly using our birdcage coil which will be described later. The imaging parameters are shown in Table 1.

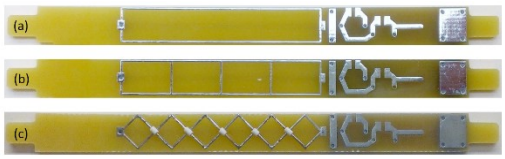

Figure 2. Trace-only DPP-like coils without any capacitors. These coils were built to validate the induced current being cancelled on the return paths of the DPPX coil. (a) Dual plane pair. (b) Dual plane pair with shorted return paths. (c) Dual plane pair with criss- cross return paths.

Static Field Simulation

To estimate the radio frequency field strength (B_1 field) of the DPPX coil, a straightforward static approach was used. We assumed the cross sectional area of the conductor compared with the length of the coil to be small, and therefore approximated the current flow on the conductor to be on an infinitely thin wire located at the geometric center of the conductor.

The DPPX coil was designed in Eagle software, and the trace pattern was exported to our in-house Biot-Savart routine implemented on MATLAB. The trace of the DPPX coil was first discretized into 1-mil (0.0254 mm) filaments, and current intensity and direction were assigned to each filament to simulate current flow.

We simulated the B_1 field of the DPPX coil with currents as shown in Figure 3 enforcing twice the current on the signal line than in either side of the return paths and enforcing 180° phase difference between the signal and return paths.

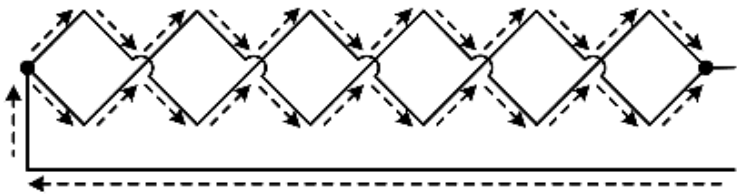

Figure 3. Current directions for the static simulation.

DPPX coil

The PCB of the DPPX coil was manufactured by Sunstone (Mulino, OR, USA) as shown in Figure 4(a) and (b). The trace width of the signal line was 30 mil (0.76 mm) and the trace width of the return path was 16 mil (0.41 mm). The width of each crisscrossed loop was 198 mil (5.03 mm), and the length of the signal line was 1855 mil (47.12 mm). In Figure 4(C), capacitor C1 = 18 pF (Passive Plus, Huntington, NY) was carefully chosen to ensure the difference of current phase between the signal line and the return paths is 180°. To choose the value of C1, we varied the values until there were no null-spot artifacts in the MR images. The variable capacitors C2 and C5 (1-5 pF, Johanson Manufacturing, Boonton, NJ, USA) were used for adjusting the tuning and the matching of the DPPX coil.

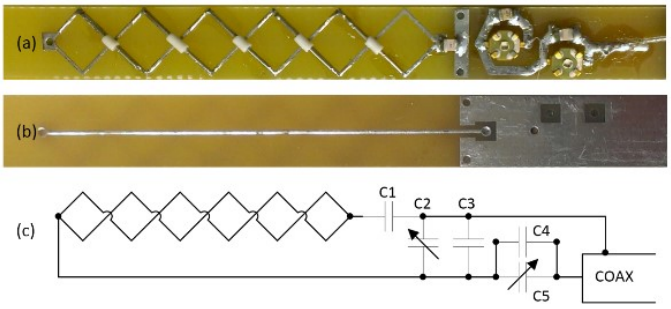

Figure 4. DPPX coil. (a) top side showing the crisscrossed return paths, (b) bottom side showing the signal line, and (c) schematic of single DPPX coil. The coil is tuned by C2 and C3 and matched by C4. The value of C1 was carefully chosen to make sure the current phase between the return paths and the signal line was 180°.

Adjustable Coil Holder

An adjustable coil holder was designed to accommodate different sizes of mice as shown in Figure 5. The ten DPPX coils were placed on two pieces of fixtures—five DPPX coils on the top of the mouse and five on the bottom of the mouse. Each set of five DPPX coils were arranged on a cylindrical surface with curvature of 0.75” (19.05 mm). To better control the coil-to-coil interactions and minimize off-centered loading problems, we designed a scissor-jack-like mechanism which lets the top five DPPX coils and the bottom five DPPX coils move equal distance from the center of the birdcage coil. In addition, this design allowed the DPPX array on the top, the DPPX array on the bottom, and the birdcage coil to always be parallel to each other regardless the travel of the DPPX array coils. This demonstrates how human cardiac arrays can be applied to mouse-sized arrays while reducing the chance of coupling to other birdcage modes such as end-ring mode. Flexible micro coax (K_01152-07, Huber+Suhner, Switzerland) was also used to allow the coil holder to move without obstruction.

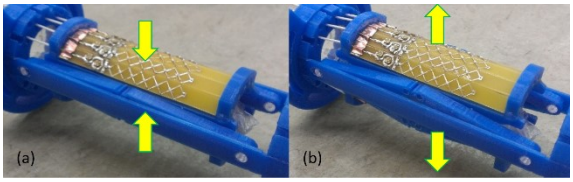

Figure 5. The scissor-jack-like mechanism of the transformable coil holder for the DPPX receive array. This mechanism can adapt to difference sizes of specimen. (a) Position for the smallest specimen and (b) position for the largest specimen.

Pre-amplifier

WanTcom pre-amplifiers ("preamp" in short, WMA4R7A, Chanhassen, MN, USA) were used to for preamp decoupling which reduces the interactions between receive and transmit coils [37]. The preamps were placed parallel to the B_0 field to increase stability. The preamps were installed on a propeller-like former as shown in Figure 6(a). Because of the ground plane under each preamp, this arrangement reduced the interference between each preamp compared with traditional same-plane arrangement.

Traditionally, a coil is connected to a pre-amplifier using either pin headers or an RF connector. This allows the coil to be disconnected from the pre-amplifier when adjusting tuning and matching of the coil is needed. However, repeated coupling of RF connectors might damage the junction between an RF connector and the coaxial cable—especially for semi-rigid cables. And, when pin headers are used, preamp decoupling might be slightly compromised if the pin headers are not inserted in a consistent manner. To this end, we incorporated switching connectors (R199006813, Radiall, Rosny-Sous-Bois, France) on the preamp module, as shown in Figure 7 and Figure 6, to help adjusting the tuning and matching of the array coil. The mechanical switch inside of the switching

connector directs the coil signal to the preamplifier by default; while it redirects the coil signal to the network analyzer when the external connector is plugged in. This allowed us to tune the DPPX coil without compromising the stability of the optimal length for preamp decoupling, and the coaxial cables were also permanently soldered on the preamp module for increased stability.

During our previous investigation, we found that a stable power source to the preamps is critical for multi-channel array MRI. When 10 preamps (200281, MicroWave Technology, Inc., Fremont, CA, USA) are used simultaneously and supplied by a bench-top power supply, the supplied voltage input can drop as much as 6 V during the receiving stage of MRI. This voltage-drop resulted in inconsistent image quality and hence limited the minimal repetition time (TR). To increase the stability of the preamps, voltage regulation and vent holes were incorporated on the array coil. According to WanTcom, the p-p voltage variable of the power source of the preamps should be less than 5 mV to ensure the stability of the preamps. However, because the voltage resolution was limited to 18 mV for ±12 V of dynamic range on our oscilloscope, we were only able to achieve 18 mV of peak-to-peak variation when C3 and C4 in Figure 7 were properly chosen.

The stability of the preamps was tested by powering-on the preamps for over 24 hours and checking the preamp decoupling afterwards. The stability of the voltage regulation was tested by monitoring the voltage output of the power supply during MR imaging.

The power supply of a preamp is usually mixed with the RF output line on commercial MR scanners. The advantage of this design is better cable handling and prevention of

interference between the DC power supply line and the RF signal line. WanTcom preamps allow users to choose either supplying the power source through the RF output port or through the dedicated DC port. We chose to supply the power source through the DC port to simplify and streamline the development process. This way, we did not need to build Bias tees for all the preamps when testing on the bench. In order to use the dedicated DC port, an RF choke was used between the bypass capacitors C3 and C4 in Figure 7. Bypass capacitor C5 was also needed after the output port of the preamp to protect the preamp and the receiver.

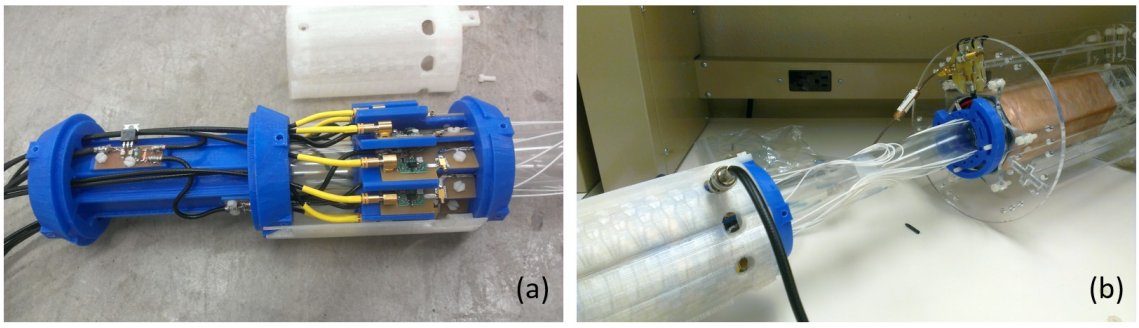

Figure 6. Preamplifiers with RF switching connector. The covers were removed to show the voltage regulator and the 10 preamplifiers. (a) The power supply of the preamps was regulated by the voltage regulator, shown on the left, before entering the preamps shown on the right. The 10 preamps were arranged on a propeller-like former to minimize the overall space required for the 10 preamps. Because of the shielding plan under each preamp, this arrangement could also reduce the interference between each preamp compared with traditional same-plane configuration. This design also posed a better angle for coupling with the RF switching connector. (b) One coaxial cable was connected to the RF switching connector on the preamp module to measure the S_{21} between the receive coil and the transmit coil. The circular cutouts provided easy access to the RF switching connector on the preamp module. This design made the tuning/matching of the array coils easier.

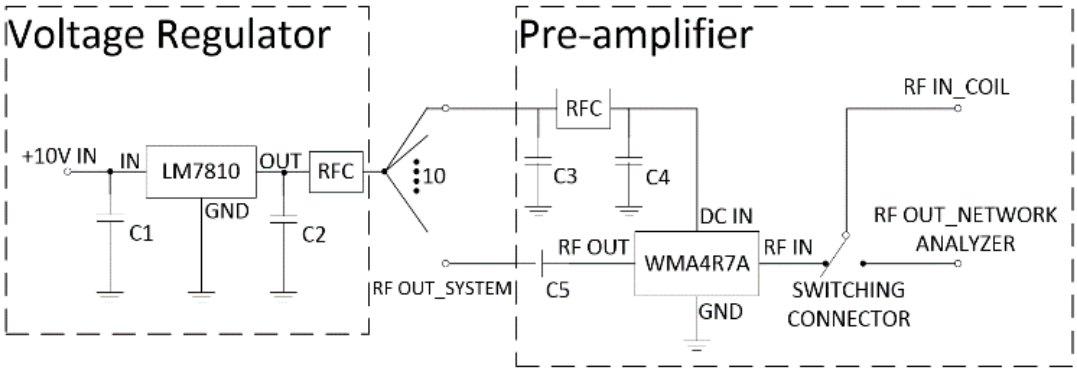

Figure 7. Voltage regulator, preamplifier and switching connector.

Linear Birdcage Transmit coil

Ensuring equal and opposite flux induced in the two halves of the elements to achieve decoupling from the transmit field requires the element to be operating in a very homogeneous field. The trombone tuning design was used to ensure the homogeneity of the transmit coil used here [124-127]. A 60-mm diameter, 16-rung, high pass birdcage was constructed using ¼" and 3/16" laser-cut acrylic sheets. Each length-adjustable rung consisted of one fixed copper tube (ID/OD/Length: 0.125"/0.156"/3.8"; K&S Engineering, Chicago, IL, USA) and one mobile copper tube (OD/Length: 0.156"/3.8"; K&S Engineering) which were coupled together. To tune the frequency of the birdcage coil, one Nylon screw rod (1/2"-13) and two Nylon nuts (1/2"-13) were used to fine tune the length of the rungs.

Imaging

Imaging experiments were carried out in the Varian Inova 4.7 T system. A cylindrical CuSO4 phantom and a euthanized mouse were used to validate the decoupling between

the adjacent DPPX receive elements and the coupling between DPPX coil and the transmit birdcage coil. Each imaging subject was loaded between the DPPX arrays first, and the arrays along with the imaging subject were inserted into the transmit birdcage coil together. The imaging parameters are shown in Table 1. Sum-of-squares was used to reconstruct the array image.

Table 1. MRI parameters for imaging the $CuSO_4$ phantom and the euthanized mouse.

Imaging Parameter	Imaging Protocol	
	Checking loop Mode of Different Kinds of Traces Using CuSO4 Phantom	***Array Imaging of CuSO4 Phantom and Euthanized Mouse***
Sequence	Spin Echo	Spin Echo
Echo Time (TE)	30 msec	30 msec
Repetition Time (TR)	1000 msec	1000 msec
Field of View (FOV)	50 mm x 50 mm	40 mm x 40 mm
Matrix Size	256 x 128	256 x 128
Slice Thickness	1 mm	1 mm
Number of Excitation (NEX)	1	1

Results and discussions

The frequency of the maximum preamp decoupling was checked after the preamps were powered-on on the bench for over 24 hours. No frequency shift was observed and this showed that the preamps were stable. There was no voltage change at the output of the power supply during MR imaging, and this showed that the voltage regulation can handle the power consumption when 10 channels of preamps were used simultaneously.

An artifact formed by the return paths of the loop mode is illustrated in Figure 8(a-b). As shown in Figure 8(c), the DPPX trace, however, did not have any visible artifacts on the phantom image. The static B_1 field of the DPPX coil was simulated and normalized as shown in Figure 9. The B_1 field was mainly distributed on the bottom (signal-line side) of the coil as shown in Figure 9(b)-(e). The B_1 field close to the DPPX coil was not

homogenous along the long axis; however, the difference in imaging depth was fairly consistent, especially considering the volume under the middle four crisscrossed loops.

During bench measurement, as shown in Figure 6(b), we found that the position of the transformable coil holder had very little effect on the tuning or matching of the DPPX coils or the birdcage coil. When the DPPX array was loaded with the CuSO4 phantom and placed inside of the transmitting birdcage coil, the S_{21} between each DPPX coil and the birdcage coil was -19 dB (for the DPPX coils on the sides of the array) to -54 dB (for the DPPX coils at the center of the array).

Phantom images are shown in Figure 10. The images received by the individual DPPX coils showed localized imaging profiles seen in Figure 10(a). The SNR comparison between the DPPX coil and the transmit birdcage coil is shown in Figure 10(c). As would be expected, the sum-of-square image showed high SNR = 160 on the outside of the phantom and decreased rapidly to SNR = 15 at the center of the phantom. The SNR of the volume-coil image showed consistent SNR = 35. The SNR inside of the sum-of-square image showed lower SNR than the volume coil, one indicator of high copper losses in the elements. The homogeneity of the transmit-coil image with the array in place, as shown on the right of Figure 10(b), is worth noting as an indicator of a lack of interaction between the array and the transmit coil.

The MR images of a euthanized mouse are shown in Figure 11. Similar to the images of the $CuSO_4$ phantom, the SNR of the sum-of-square image was higher on the outside and lower at the inside of the euthanized mouse.

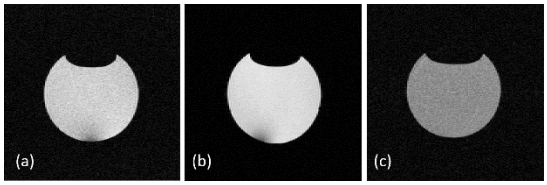

Figure 8. Images of a CuSO4 phantom with trace-only coils taped underneath. We taped each trace-only coil under a cylindrical CuSO4 phantom (OD = 27 mm, wall thickness = 300 µm), and we imaged the assembly inside of the transmitting birdcage coil. Because the wall thickness of the phantom was so thin and the coils were taped right on top of the phantom, any induced currents on the coils would de-phase the phantom signal and show shaded artifact on the image. Figure (a)-(c) show phantom images when (a) traditional DPP trace, (b) traditional DPP trace with shorted return path, and (c) DPPX trace were individually placed under the phantom

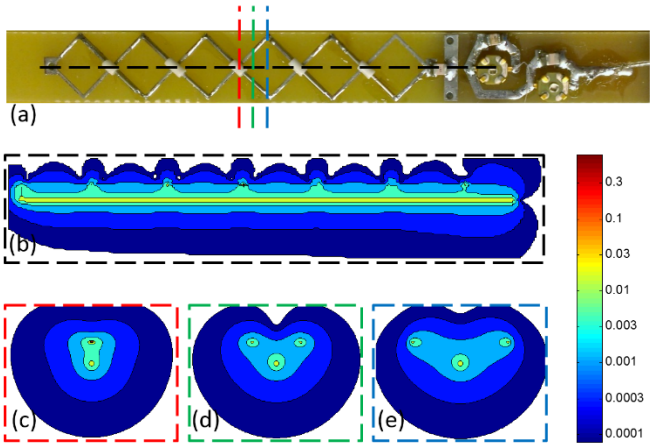

Figure 9. Contour plot of simulated static field of DPPX coil. The B_1 field was normalized to the maximum value inside of the 3-dimensional volume of interest. (a) The top side of the DPPX coil. Dashed lines were color coded to indicate the location of the B_1 field at the (b) sagittal plane, and (c)-(e) different axial planes.

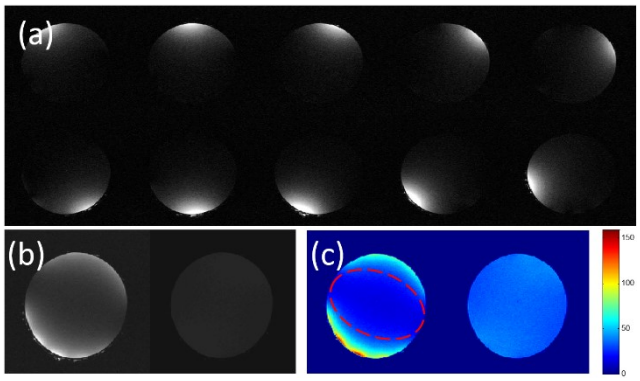

Figure 10. CuSO4 phantom image acquired by the DPPX array and the transmitting birdcage coil. (a) Phantom images acquired from individual DPPX coil. (b) (left) The composed array image using sum-of-square method. (b) (right) The volume image acquired by the birdcage coil when the DPPX array was inside of the birdcage coil (image intensity was increased by five times for visualization). (c) (left) The SNR of the sum-of-square image. (c) (right) The SNR map of the volume image. The red dashed line represents the SNR lower than the SNR received by the birdcage coil.

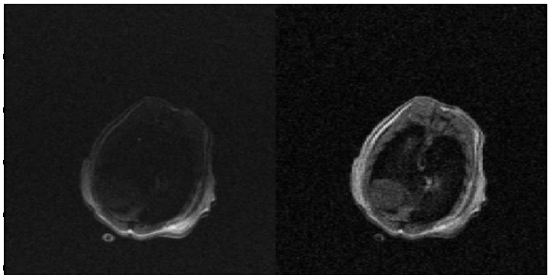

Figure 11. MR images of the mouse heart of an euthanized mouse. The image on the left shows the sum-of-square image received by the DPPX array. The image on the right shows the image received by the birdcage coil.

Conclusion

In summary, the array is extremely robust in regards to loading conditions, compact, and mechanically adjustable to accommodate differently sized specimens. As intended, the DPPX design successfully eliminated the coupling of the loop mode to the transmit coil. Furthermore, the homogenous volume image of the phantom demonstrated that DPPX

element is able to geometrically decouple from the transmit coil without the use of active-detuning circuits. The images received by individual DPPX array elements also show good decoupling between receive elements.

However, the copper losses from the DPPX elements will limit the use of this particular array to surface applications. In addition, the characteristics of the elements might prove useful when scaled to a larger size where sample loss dominance is more likely.

CHAPTER IV

STREAMLINED DESIGN OF 6-CHANNEL ARRAY COIL FOR GENERAL-PURPOSE MOUSE IMAGING*

The signal-to-noise (SNR) benefit of using of array coils for mouse and other small animal imaging is appealing for several reasons. Most foundationally, the increase in SNR can be exploited to achieve the small voxel sizes required to resolve small animal features in a reasonable scan time. A whole-body scan is usually not required in most popular neuroscience, cardiovascular, muscular or abdominal studies, however, and the use of an array coil can also provide the convenience of a one-size-fits-all solution, achieving the SNR of a targeted surface coil for a variety of anatomies without moving the animal or re-positioning a surface coil.

Several groups have investigated the design of array coils for mouse imaging. Keil *et al*. have reported the design of a state-of-the-art, 20-channel, whole-body mouse array coil based on a human 3T system [110]. The 20-channel coil array consists of 4 tiers of 5 circularly arranged receiving coil elements which provide both whole-body volumetric coverage and parallel-imaging capability along any directions. While the 20-channel array coil is versatile, the large coil size does not fit in high-field animal scanners and high-

* Part of the data reported in this chapter is reprinted, with permission, from Wen-Yang Chiang and Mary P. McDougall. Streamlined construction of a six-channel mouse array coil with 3D printing. *Proceedings of the 23rd Annual Meeting of ISMRM*, Toronto, Ontario, Canada, May 2015.

channel-count receivers are not widely available. Instead of full-body coverage, the eight-channel mouse coil array reported by Lanz *et al*. focused on the local mouse anatomy on a high-field 9.4 Tesla preclinical system [106]. The 8 receiving coils tightly encircle a mouse (up to 30 g) and provide excellent parallel-imaging capability for local anatomy of interest. The 4-channel one-dimensional receiving array reported by Garies *et al*. [105] provides a simple solution for mouse spinal imaging with enhanced SNR. However, while SNR is increased for tissue adjacent to the receiving coil array, the SNR suffers greatly for tissue further away.

Fabrication of array coils for small animal imaging is challenging for several reasons. Geometric decoupling [37] in small-animal array coils is more susceptible to human error and inter-coil inconsistency—due to the fact that sub-millimeter changes of overlap between adjacent coils can affect geometric decoupling greatly. Although printed-circuit-board-based coils can reduce this kind of fabrication error, wire construction is preferred for a higher unloaded-to-loaded Q ratio [87, 110]. Traditionally, the outlines of wired coils are either hand-drawn, milled by a milling machine or transferred from a stencil onto the coil former. Regardless of the ways to place fiducial marks on the coil former, the dimension of the coils and amount of overlap are adjusted iteratively and manually. The process is usually time-consuming, and it is also difficult to maintain consistency among all the coils.

In addition, it can be difficult to maintain sample noise dominance when constructing small coils and the construction of high-Q elements is of increased importance. Another

significant challenge in the construction of arrays for small animals is the limited space in standard (small bore higher field) animal scanners for traditional hardware such as baluns/cable traps, active decoupling networks, and low input impedance preamplifiers.

This work describes mitigating these challenges in making small-animal MRI coils by discussing the design and construction of a six-channel array coil for imaging mice in a 4.7T/40cm scanner. 3D printing was used to allow for 1) repeatable and optimized geometric decoupling, 2) ease of coil construction with wire elements for better unloaded/loaded Q ratio, and 3) stable and repeatable field patterns from each element. A sliding-bed mechanism was introduced to provide the ability to image any part of the mouse anatomy without increased complication in the set up procedure. Custom designs for integrating and managing the ECG/ respiratory gating wires and the delivery of maintained anesthesia were also easily realized and integrated in a limited space.

Materials and methods

Calibration of 3D printer

A consumer-level 3D printer (Replicator 2, MakerBot Industries, Brooklyn, NY) was used to help construct the mouse array coil. A calibration pattern was designed in SolidWorks 2013 (Dassault Systèmes SolidWorks Corporation, Waltham, MA) as shown in Figure 12(a). The actual dimensions of the printout were measured using a caliper, and the calibration curves in x-, y- and z-directions were plotted in Figure 12(b-d). Linear regression was used to estimate the scaling factors in the x, y and z directions. Based on the calibration curves, Netfabb (Parsberg, Germany) software was used to scale the

original 3D models by 100.69%, 100.35% and 100.45% in x, y and z directions, respectively, before the 3D model of the coil former was printed using the Replicator 2 3D printer.

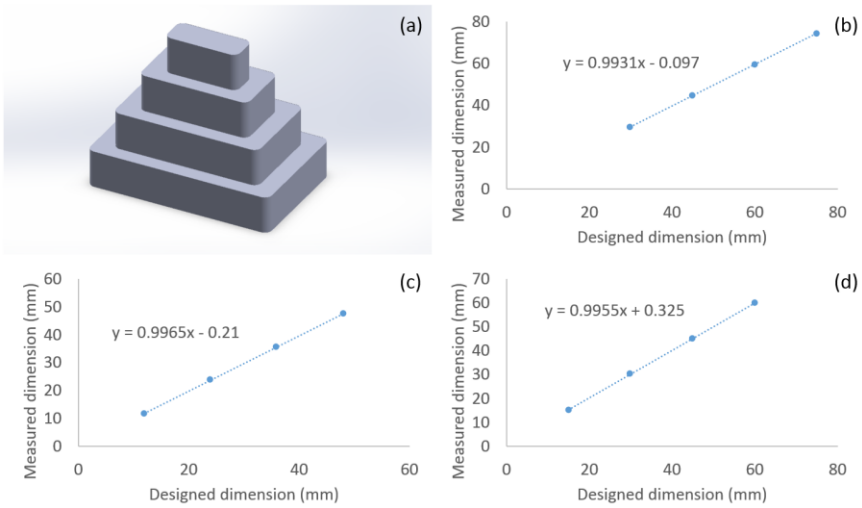

Figure 12. Calibration of Replicator 2 3D printer. (a) Custom design of calibration pattern, and (b-d) calibration curve in x-, y- and z-directions.

Design and construction of 6-channel array coil

Geometric decoupling assisted by 3D printing

To demonstrate the precision/utility of 3D printing for geometric decoupling, coil formers (ID = 31.75 mm and OD = 38.1 mm) were designed in SolidWorks 2013 (Dassault Systèmes SolidWorks Corporation, Waltham, MA) CAD software as shown in Figure 13. The pattern of the 6 loop coil was drawn on a 2D sketch plan, and the sketch was etched on the cylindrical coil former using the "wrap" feature. The diameter of each loop coil was calculated based on the predetermined percentage of overlap as follows:

$$Diameter\ of\ loop\ coil = \frac{circumference\ of\ coil\ former}{6(1 - percentage\ of\ overlap)}$$

A total of 4 formers with 23%, 25%, 27% and 28% of overlap were designed. The corresponding diameters of the coil elements were 25.91 mm, 26.60 mm, 27.33 mm and 27.71 mm, respectively. After the CAD designs were exported as STL files from SolidWorks, Netfabb software was used to scale the 3D models according to the calibration values mentioned above in x, y and z directions. The models were printed using an in-house modified Replicator 2 3D printer using polylactic acid (PLA) material. Standard quality (2 shells, 10% in-fill and 0.2 mm layer height) was used for 3D printing. Tetrahydrofuran was lightly applied on the coil formers to remove minor surface defects which are commonly seen on parts printed by consumer-level 3D printers. During our investigation, we found that the hardness of PLA treated with tetrahydrofuran change slightly over time. To minimize error resulting from the changes in the material properties, each former was rested in a well-ventilated location for more than 48 hours before coils were installed on the coil formers. The tuning/matching boards of the coil elements were made by a milling machine (H100, LPKF Laser & Electronics AG, Garbsen, Germany), and fixed on the coil formers with double-sided tape. AWG 22 wires were pushed inside of the grooves on each coil former. For each coil former, only two adjacent coils were populated. To determine the optimal overlap, each pair of adjacent coils was connected to a network analyzer. S_{11} measurement was used to observe mode splitting in the heavily coupled condition, and S_{21} measurement was used to quantify the interactions between lightly coupled adjacent coils. After the optimal overlap was determined, six array coils

were fully populated on the final former with the same amount of overlap as shown in Figure 14.

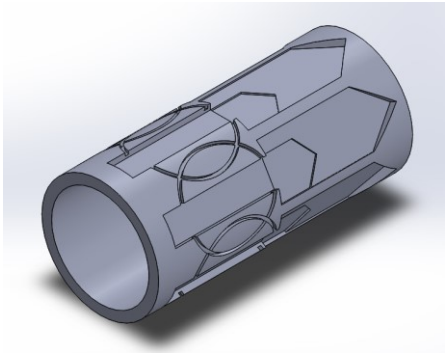

Figure 13. Coil former with the etched pattern of coils and tuning/matching boards. The dimensions of the coil former are ID = 31.75 mm and OD = 38.1 mm. The 3D model shown here uses 27% of overlap for geometric decoupling. The triangular etched pattern is to help in 3D printing without requiring a support structure.

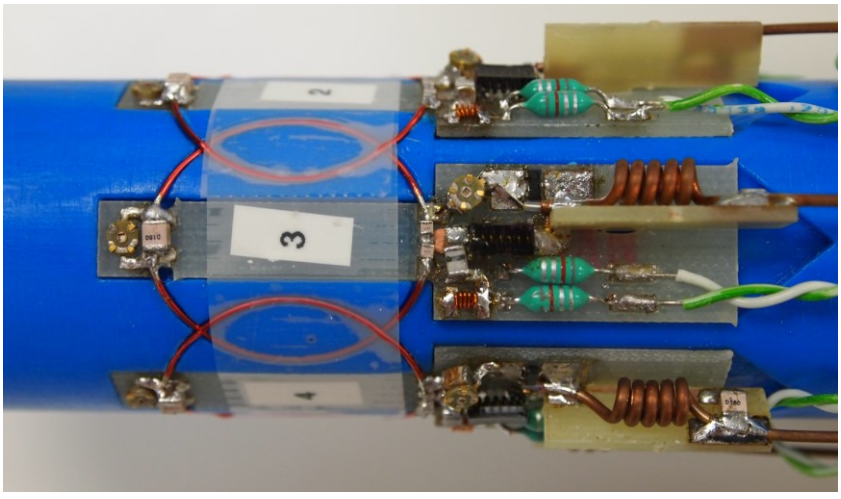

Figure 14. The construction of the 6-channel receive array. The variable capacitor on the left side of the coil is for tuning, and the variable capacitor on the right is for noise matching. A fixed capacitor is soldered under the latter variable capacitor to save space. The cable trap is mounted on a vertical printed circuit board. The PIN diode signal is fed through white-and-green twisted pairs in line with RF chokes in green.

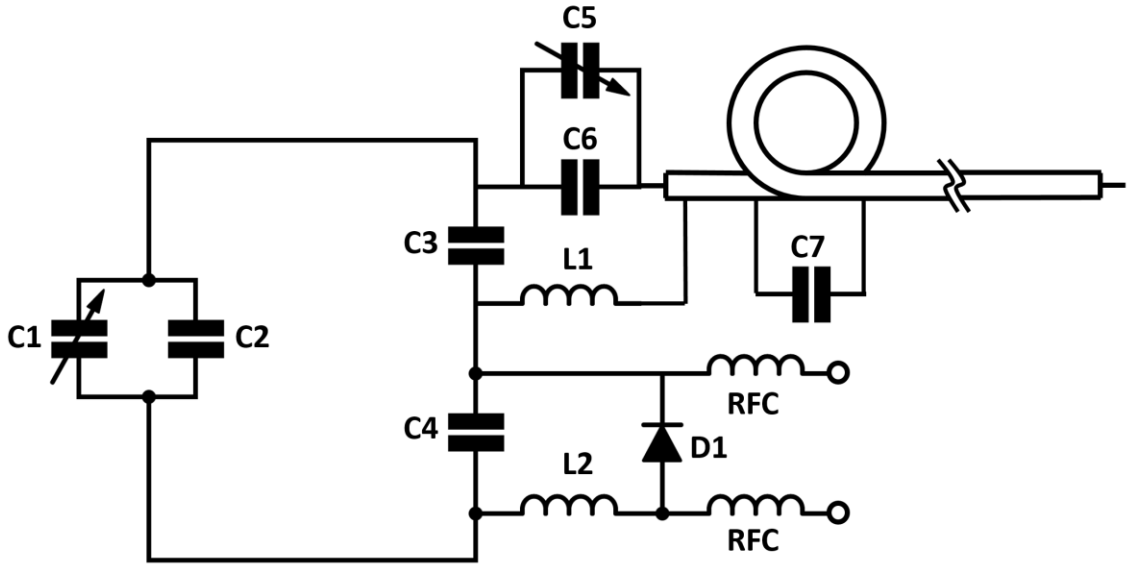

Figure 15. Circuit schematic for each coil element. Capacitors C1 and C2 are for tuning. Capacitors C3 and C4 are of equal value and serve as an impedance divider at the coil output. Because the impedance at the coil output is small, the inductor L1 is used along with capacitors C5 and C6 for easier noise matching to 50 Ω. Active detune is done by forward-biasing diode D1 therefore C4 and L2 are resonated at Larmor frequency. The semi-rigid coaxial cable was wound for 5 turns on a #38 drill bit and resonated with C6 to suppress common mode currents. The length of the semi-rigid cable is adjusted until the low-input impedance of the preamplifier (not shown here) is presented to the coil. (C1 = 6-25 pF, C2 = 15 pF, C3 = C4 = 39 pF, C5 = 6-25 pF, C6 = 15 pF, C7 = 15-20 pF, L1 = 22 nH and L2 = 17 nH.)

Tuning/matching of array coil

The circuit schematic of each coil element is shown in Figure 15. The variable capacitor C1 = 6-25 pF (9702-6, Johanson Manufacturing, Boonton, NJ, USA) and the chip capacitor C2 = 15 pF (Passive Plus Inc., Huntington, NY, USA) were used for tuning. Compared to placing the tuning capacitor at the coil output, moving the tuning capacitor to the far side not only presented better quasi-static condition of the coil, but also optimized the usage of the limited coil former footprint. The chip capacitors C3 and C4

served as the impedance divider at the coil output. The variable capacitor C5 = 6-25 pF, the chip capacitor C6 = 15 pF and the inductor L1 = 22 nH (B07T, Coil Craft, Cary, IL, USA) were used for noise matching to 50 Ω. The inductor L2 = 17 nH was used to resonate the capacitor C4 as the active detune trap when the PIN diode (MA4P7470F-1072, M/A-COM Tech, Lowell, MA, USA) was forward-biased. PIN diode signal was fed through a twisted pair of wires and two RF chokes (Bourns, Riverside, CA, USA). Each PIN diode signal line could be individually controlled by a PIN header for testing purposes. Because the PIN diode signal was not mixed with the RF line, no specialized interface boxes or bias tees were needed for bench testing, and the design of the active trap was independent from the matching capacitor/inductor.

An unshielded cable trap was constructed to suppress the common mode current for each coil element. The cable trap was soldered on a separate, printed circuit board which was mounted vertically to the coil. This allowed the cable trap to be tuned individually. The semi-rigid cable (EZ 47-Cu-TP, EZ Form Cable Corporation, Hamden, CT, USA) was wound on a #38 drill bit for 5 turns, and a 15-20 pF capacitor was used to tune the cable trap to the Larmor frequency. Although the cable traps were unshielded, no coupling between coils or between cable traps was observed.

Preamplifier and preamp decoupling

Preamplifiers were used for preamp decoupling. The design of the preamplifier modules, as shown in Figure 16 , was based on the design presented in Chapter III and our previous report [128]. While the original design supported up to 10 preamp modules, only 6 out of

10 preamp modules were used because there were only 6 receiving elements in this mouse array coil. One PIN diode signal input was added to support the active detune traps on the 6 receiving array coils.

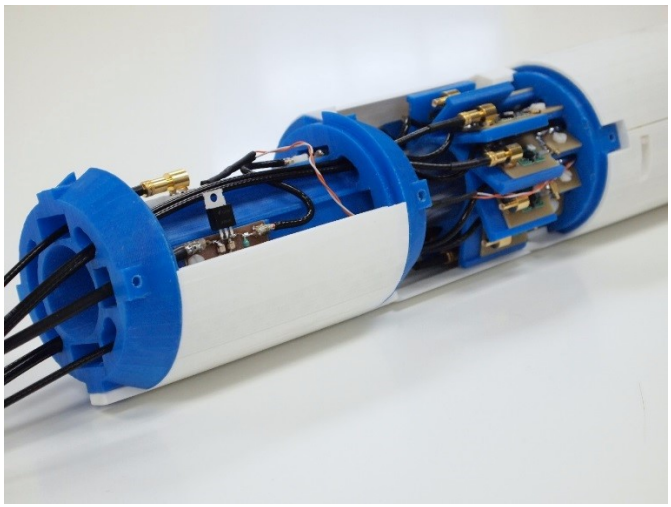

Figure 16. Preamp modules and voltage regulator. The covers of these two compartments were partially removed to reveal the internal constructions. (left) The right-angle SMB connector shown on the top was the input for the PIN diode signal which controlled the active detune trap on the array coil. Because the power source of the preamp modules was supplied by a bench-top power supply, it was necessary to regulate the power input through a voltage regulator, shown in the middle, to increase the stability of the preamps. (right) The 10 preamp modules were arranged in a propeller-like former to 1) reduce the footprint, 2) pose a better angle for the RF switching connector and 3) increase the isolation between the preamp modules. While this design is applicable to general receiving array coils up to 10 channels, only 6 out of the 10 preamp modules were used here.

Bench measurement

A shielded transmitting birdcage coil (ID = 5.5 cm, nominal OD = 9 cm and length = 12 cm) with four active detune traps was built as shown in Figure 17. A cylindrical phantom (100 mM NaCl, ID = 27.5 mm, length = 57 mm) was made as the load. A network analyzer

was connected to the RF switching connector on the preamp module to tune and match the array coil using S_{11} measurement. The array coil was tuned to Larmor frequency and noise matched to 50 Ω when the array coil was loaded with the phantom and placed inside of the birdcage coil while the birdcage coil was detuned. The preamp modules were supplied by 10 V, the outputs of the preamps were loaded with 50 Ω terminations, and all the array elements were enabled during the S_{11} measurement. The S_{21} measurement followed immediately after the S_{11} measurement in order to estimate the coupling between each pair of coils. During the measurements, only the two testing coils were enabled while the other four coils were detuned. Each pair of coils were connected to a network analyzer through RF switching connectors on the corresponding preamp module. A pair of double probe overlapped for cancelation of flux from mutual coupling [129] was used to measure unloaded to loaded Q ratio of the receiving coils.

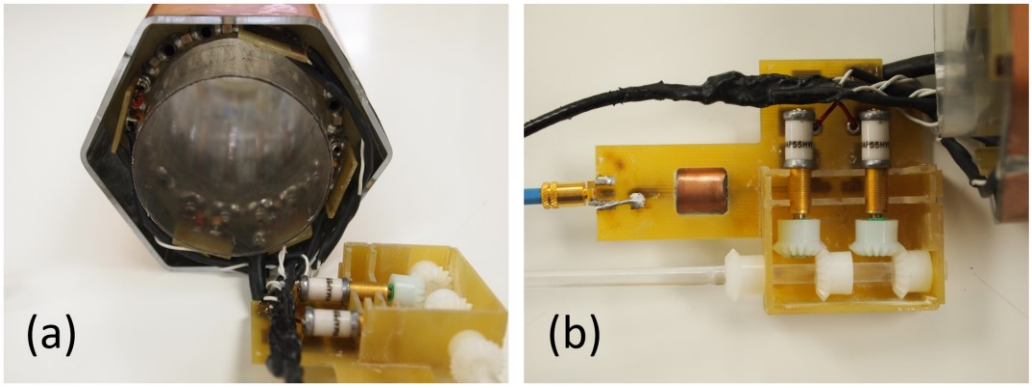

Figure 17. Transmit birdcage coil for mouse receiving array coil. (a) Four active detune traps were installed at 45°, 135°, 225° and 315° to the coil output (bottom right). The PIN diode signal to the active traps were supplied by twisted pairs in line with RF chokes. The active traps were soldered and tuned on separate printed circuit boards before being installed vertically to the end ring of the birdcage coil. (b) Balanced matching capacitors and a cable trap were used to reduce common mode. The variable capacitors were installed with a set of gears to ensure the capacitor values of the two variable capacitors remained equal when the matching rod (transparent rod shown on the bottom) was turned.

Mechanical designs for animal handling

To streamline *in vivo* mouse imaging, we designed a new mouse bed with integrated air ducts for anesthesia delivery as shown in Figure 18. By integrating the traditional nose-cone-like design into the mouse bed, the space inside of the array coil was better utilized and the assembly was also simplified. The nozzle on the rear end of the mouse bed, as shown in Figure 19(a), connected to the hot air hose which kept the body temperature of the mouse at normal level. The mouse bed also supported a commercially-available mouse sled with built-in cardiac/respiratory gating sensors (Dazai Research Instruments, Toronto, Ontario, Canada and SA Instruments, Inc., Stony Brook, NY, USA). Bite bars and ear bars were not needed because the mouse sled also served as the body constraint for the mouse. As shown in Figure 19(b), a disposable transparent lining was used to wrap

around the mouse bed for easy cleaning. Because the mouse bed was 3D printed, it was also disposable and could be replaced easily after repeated use.

A twist-n-lock mechanism was designed to reduce the complexity of setting up *in vivo* mouse imaging experiments as shown in Figure 20. By sliding the blue collar on the mouse bed, this new mechanical design could securely position the mouse bed in the receive coil when different parts of the mouse were imaged as shown in Figure 21. Prior to imaging, the blue collar, shown in Figure 21(a), was moved to a designated position on the mouse bed, and the area of interest was automatically positioned at the array coil when the mouse bed was inserted as shown in Figure 21(b-c). Once the mouse bed was fully inserted, the user twisted the mouse bed clockwise to lock the mouse bed in the array coil as shown in Figure 20(c, d).

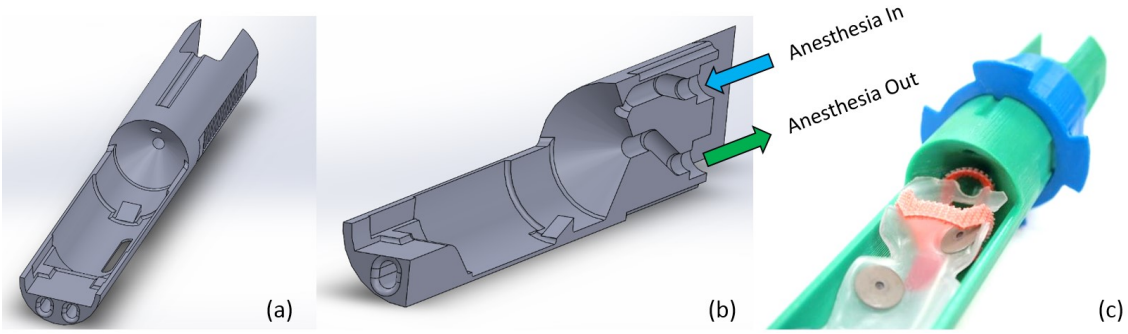

Figure 18. The design of the mouse bed for delivery of anesthesia and respiratory/cardiac gating. (a) The CAD design of the mouse bed with integrated nose cone for the delivery of anesthesia and structures for securing the mouse sled. (b) The cut-away view shows the air duct for the delivery of anesthesia. (c) The actual mouse bed with cardiac/respiratory gating sled made by Dazai Research Instruments.

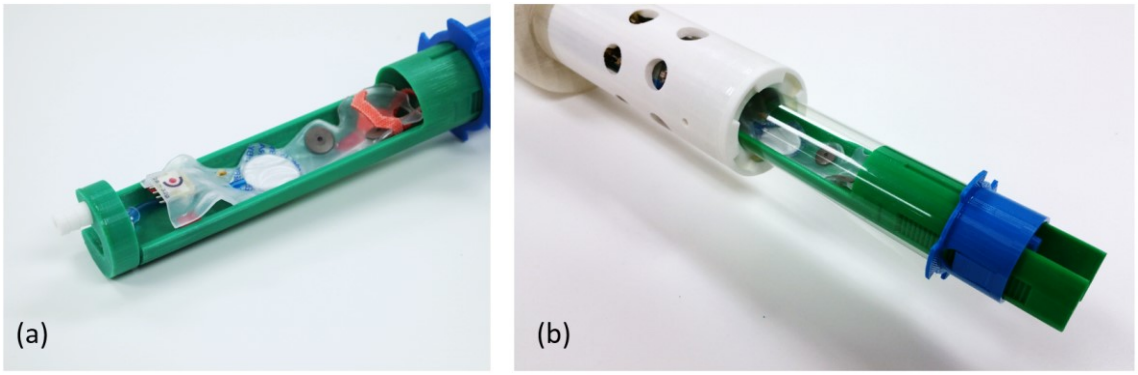

Figure 19. Mouse bed and body restraint using mouse sled. (a) The mouse sled served as the restraint for the mouse, therefore, other types of restraints such as a bite bar or ear bars were not needed. While the anesthesia was delivered from the integrated nose cone shown on the right, the hot air, which maintains the body temperature of the mouse, was delivered through the air tube (not shown in the photo) that was connected to the white nozzle on the left. (b) A piece of transparent liner was wrapped around the mouse bed before it was inserted into the array coil. This design simplified the cleaning process after each mouse imaging.

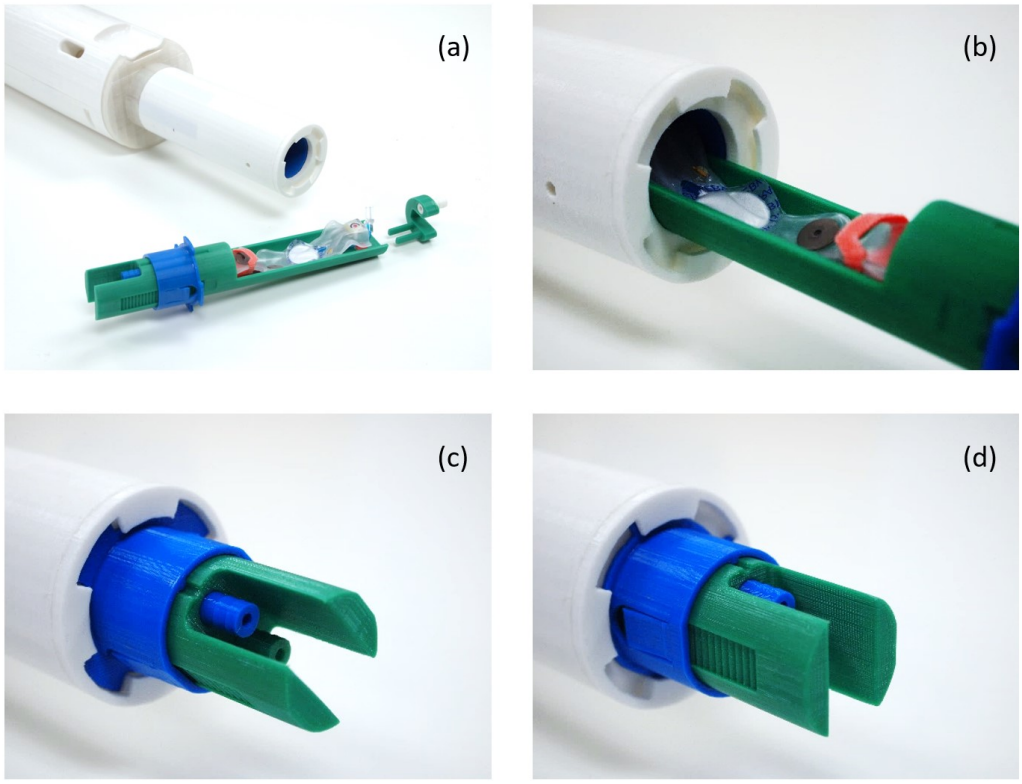

Figure 20. Twist-n-lock mechanism for reducing complexity of setting up an *in vivo* mouse imaging experiment. (a) The 6-channel mouse receive array is inside the white cylindrical cover shown on the top. The mouse bed in green with SAII's mouse sled are shown on the bottom. The separate green and white piece behind the mouse bed was the clip that secured the hot-air hose. (b-d) The twist-n-lock mechanism helped the user to load the mouse into the receiving array coil easily and consistently.

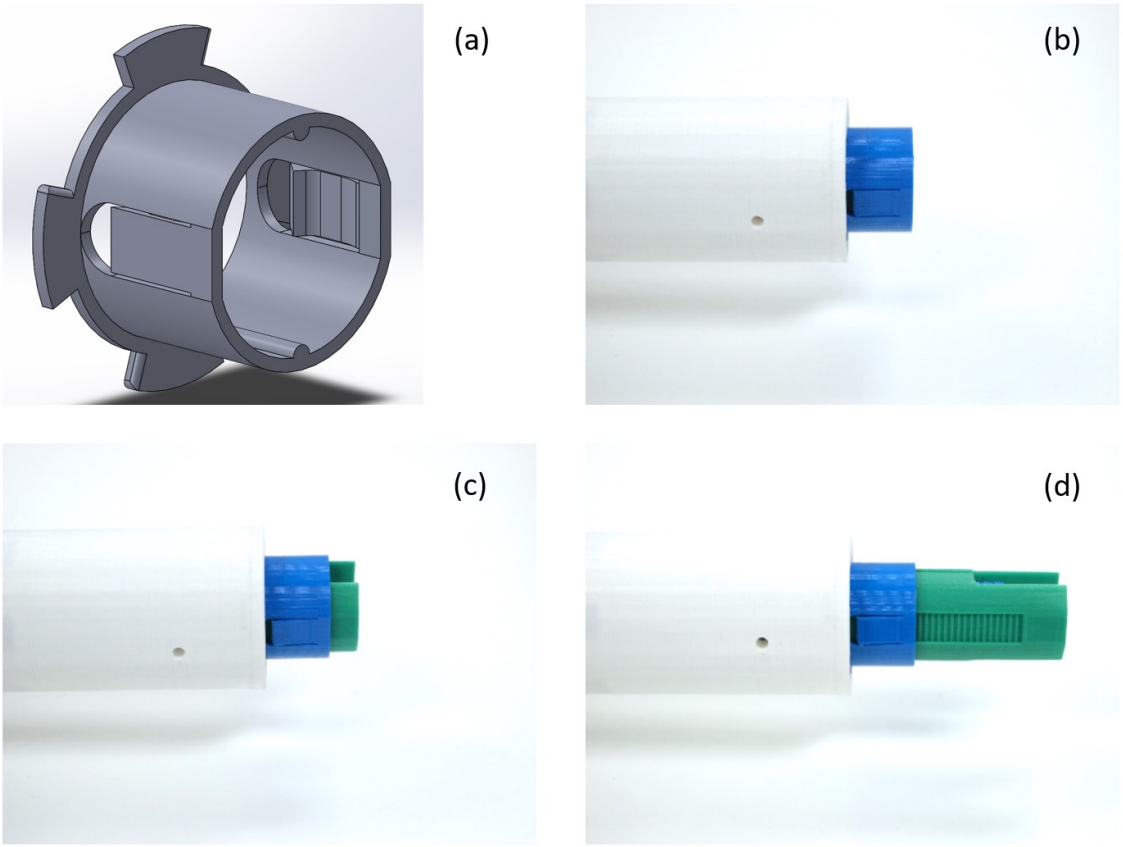

Figure 21. An integrated locking mechanism allowed the position of the mouse bed to be adjusted easily for imaging different parts of the mouse. (a) The collar on the mouse bed was designed with two flexible flaps on both sides. Each flap has one tooth to lock the collar to the array of teeth on the side of the mouse bed. The half-cylindrical rails at the inner surface of the collar couple to the reciprocal grooves on the mouse bed and prevent the collar from rotating when the position of the collar is adjusted along the mouse bed. (b and d) These three positions demonstrate three common imaging positions for brain, heart and abdominal imaging.

Phantom and in vivo mouse imaging

Phantom and *in vivo* mouse imaging was performed on a Varian INOVA 4.7T/40-cm system to validate the proposed 6-channel mouse coil array. One cylindrical phantom (1 g/L CuSO4 and 5.4 g/L NaCl, ID = 27.5 mm, length = 57 mm) was used for phantom imaging. The imaging parameters were as follows: TE = 30 ms, TR = 1000 ms, FOV = 50

mm x 50 mm, matrix size = 256 x 128 and slice thickness = 1 mm. To avoid the variation of noise figure and gain between the stock INOVA receiver and our in-house built multi-channel receiver, the SNR comparison between volume coils and the proposed coil array was performed via the stock INOVA receiver. The signal of each receive coil element was received one-by-one.

The SNR achieved by the six-channel array was compared with 1) the transmit coil – a linear birdcage coil built in-house (ID = 55 mm, OD = 84 mm) with 16 rungs and four active detune traps, and 2) a commercial Varian 3.5-cm-diameter quadrature birdcage coil. Inter-element consistency was shown by rotating the individual field patterns of each element into alignment with one another. The intensity of the images received by individual receiving elements were linearly normalized from 0 to 1, and the standard deviation of the normalized intensity was calculated voxel-by-voxel. The fiducial marks on the edge of the phantom were excluded in the analysis to prevent artifacts.

A previously reported [130] multi-channel receiver was used for acquiring multi-channel MR data. Noise correlation matrix was used to evaluate coil coupling. The 6-channel coil array was loaded by the phantom stated above, and noise-only images were acquired without transmitting RF power. Noise correlation was estimated by in-house developed MATLAB script and built-in CORRCOEF function, and the noise correlation between any two channel i and j is defined as

$$\psi_{ij}^{corr} = \frac{\langle (N_i - \mu_i)(N_j - \mu_j) \rangle}{var(N_i) var(N_j)}$$

where $\langle \quad \rangle$ is the expected value operator, $var(\,)$ is the variance operator, N_i and N_j are noise-only images from channel i and j.

In vivo mouse imaging was performed under the animal use protocol approved by Institutional Animal Care and Use Committee (IACUC) of Texas A&M University. The mouse was restrained on a mouse sled (Dazai Research Institute, Toronto, Ontario, Canada) and transferred onto the proposed mouse bed as shown in Figure 19(a). 1.5% of Isoflurane was administered during the *in vivo* mouse imaging. The mouse vitals including cardiac/respiration cycles and body temperature were monitored (Small Animal Instruments, Inc., Stony Brook, New York, USA), and the concentration of Isoflurane was adjusted accordingly to ensure mouse safety. Cardiac and respiration motion was not gated to avoid variation of tissue contrasts. To reduce motion artifact without involving advanced off-line gating techniques, four acquisitions were repeated, and the data was combined in image domain. Three different parts of one mouse were imaged in one session to demonstrate the ability of mouse handling and *in vivo* mouse imaging. The position of the mouse bed was adjusted inside of the coil array, and sagittal images were used to localize the location of anatomy of interest, and the axial images were followed. This process was repeated 3 times for the *in vivo* imaging of mouse brain, kidney and bladder.

Results and discussions

The coils built on the coil formers with 23% and 25% overlaps were quickly discarded because the S_{11} measurements showed significant mode split which indicated large coupling between adjacent coils. The best-case geometric decoupling out of the four tested

cases was S_{21} = -17.4 dB at 27% overlap, when the diameter of the loop coils was 27.32 mm. As an example of the fine-tuning of geometrical decoupling enabled by 3D printing, the S_{21} between the adjacent channels became -9.3 dB when the overlap was slightly increased to 28%—even though the change in diameter was only 0.4 mm. The final receive array coil was finished on the former with 27% of overlap as shown in Figure 14 and Figure 22. Table 2 shows the S_{21} between each pair of coils when the other four coils were actively detuned. For some adjacent coil pairs, we were able to further reduce the coupling between the adjacent coils to -19.9 dB by tweaking the soldering spots of the AWG 22 wires on the tune/match boards. One should note that, because preamp decoupling could not be used during the S_{21} measurement, the actual isolation between the next-to-the-nearest elements was underestimated. Preamp decoupling provided an additional 15-18 dB of isolation when the array coil was used for imaging in the MRI scanner.

For one single loop coil mounted on the coil former with 27% overlap, the unloaded to loaded Q ratio was 143/102= 1.40. The unloaded to loaded Q ratio was measured again after the full 6 receiving array coils were populated, and it slightly decreased to 1.30±0.03.

The phantom images received by the individual loop coils show clearly isolated and consistent field patterns, as shown in Figure 23. In addition, as seen in Figure 24(a), the homogeneity of the transmit coil image verified the absence of coupling between the transmit coil and the receive array. Figure 24(b-c) indicates the sum-of-squares array reconstruction showed an average SNR increase over the Varian quad birdcage of 2.64 times (max = 4.08, min = 1.21), slightly inflated by the sum-of-squares reconstruction

from single-channel imaging (versus parallel reception with correlated noise). The mapping of the normalized standard deviation between the field patterns of the six elements is shown in Figure 25, indicating highly consistent/repeatable patterns from each element (mean standard deviation = 0.15, max standard deviation. = 0.23, min standard deviation = 0.07).

Noise correlation matrix demonstrated good isolation between receive elements in Figure 26 The maximum noise correlation coefficient was 15.5%, and the average noise correlation coefficient was 3.7%. This demonstrated the efficacy of preamplifier decoupling on top of geometric decoupling.

The capability of *in vivo* mouse imaging over different parts of a mouse is demonstrated in Figure 27.

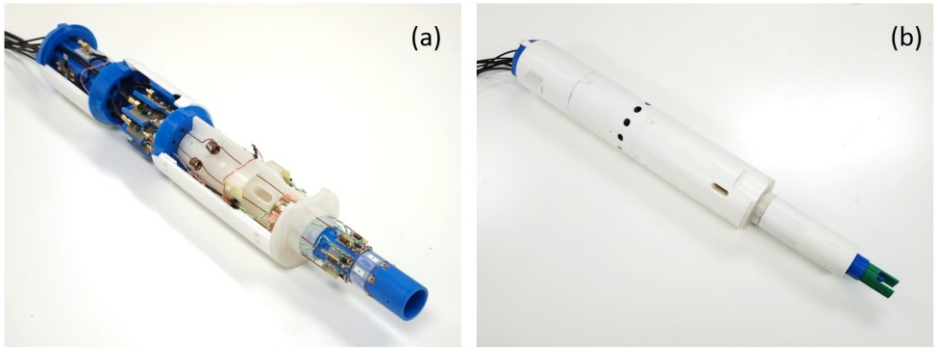

Figure 22. Over view of 6-ch mouse array coil. (a) The covers were partially removed to reveal the internal construction. The array coil was divided into four compartments: (from top left to bottom right) voltage regulator, preamp modules, half-wave length cables and the 6-ch receiving coil array. (b) 6-ch mouse array coil with mouse bed (blue and green at the bottom right) inserted. The holes on the covers were for (from top left to bottom right) venting of the voltage regulator, access windows for the RF switching connectors and access windows for respiratory/cardiac gating sensors.

Table 2. S_{21} measurement of 6-ch mouse receiving array coil.

	Ch 1	Ch 2	Ch 3	Ch 4	Ch 5	Ch 6
Ch 1		-14.5	-4.3	-5.5	-4.8	-19.9
Ch 2	-14.5		-16.9	-4.6	-5.0	-4.5
Ch 3	-4.4	-16.8		-17.7	-4.7	-5.6
Ch 4	-5.1	-4.2	-17.1		-15.2	-5.2
Ch 5	-4.5	-4.6	-4.7	-15.2		-15.2
Ch 6	-19.6	-4.3	-5.4	-5.2	-15.3	

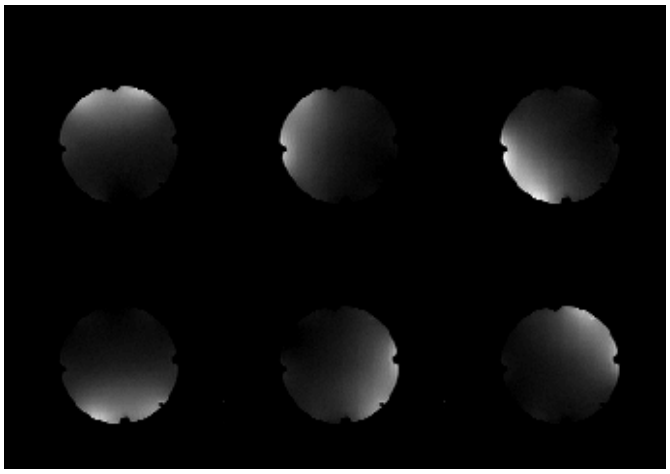

Figure 23. Phantom images received by individual loop coils showing decoupled field pattern.

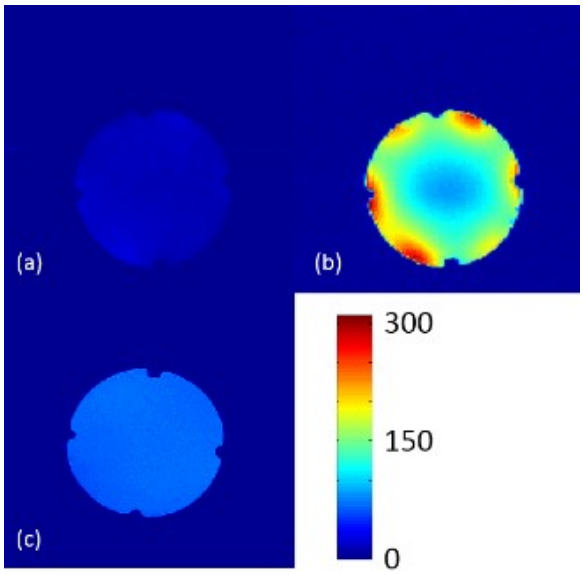

Figure 24. Comparison of phantom images. The phantom images were received by: (a) linear transmit coil, (b) 6-ch mouse array, and (c) Varian quadrature mouse birdcage coil

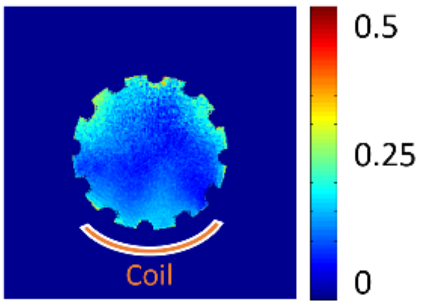

Figure 25. Standard deviation of the normalized field patterns of the six receiving elements. Each individual receiving coil had very similar sensitivity pattern, especially for where it's closer to the coil, and this demonstrated that the sensitivity pattern was repeatable when the coil former was made by a 3D printer.

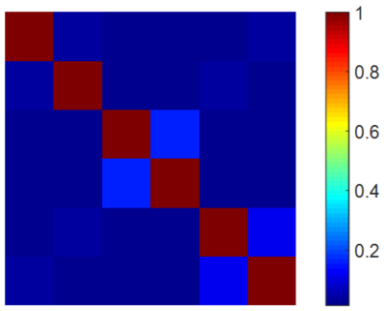

Figure 26. Noise correlation matrix of 6-channel mouse coil array. The maximum noise correlation is 15.5%, the minimum noise correlation is 1.3%, and the average noise correlation is 3.7%. This demonstrated effective geometric decoupling and preamplifier decoupling.

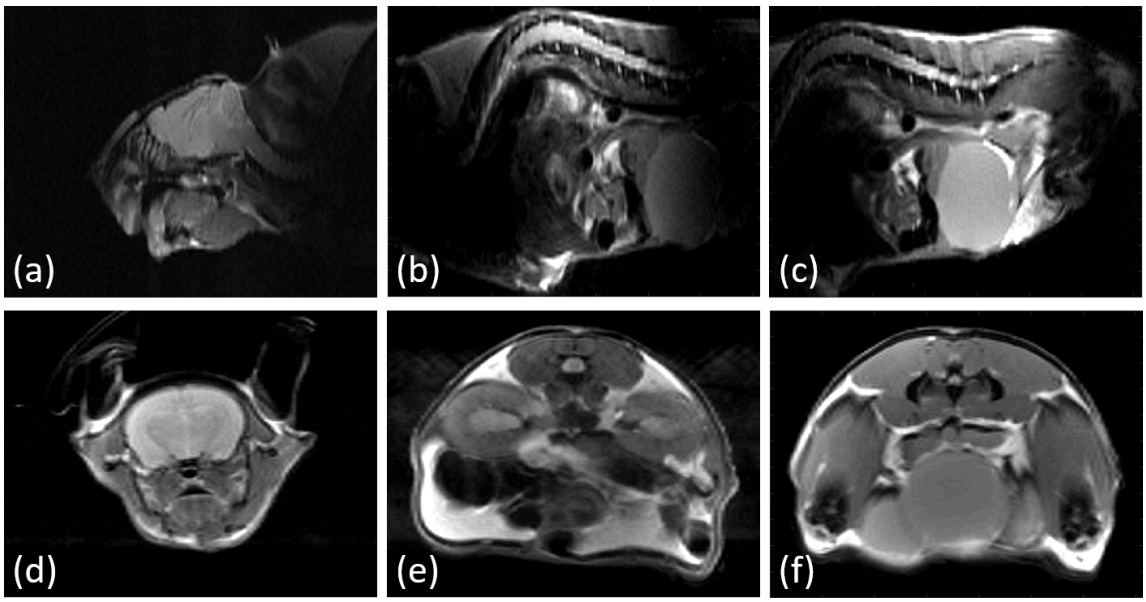

Figure 27. *In vivo* mouse imaging using 6-channel mouse coil array. The array images are combined with root of sum-of-square reconstruction. The brain, kidney and abdominal areas are imaged individually. Mid-sagittal images of the mouse (a-c) are used to localize the anatomy of interest, and the acquisition of corresponding axial images of brain (d), kidneys (e) and bladder (f) are followed. Motion artifact is largely reduced with four averages except in (e) where the image quality of kidneys is affected. Along top-to-bottom direction, roughly 3-pixel of chemical shift is visible due to relatively short readout bandwidth (195.3 Hz/pixel). Good contrast between gray matter, white matter and muscle is observed in all three segments of the mouse.

Conclusion

Our work shows that we can build an MRI receive coil array of good geometric decoupling and consistent coil sensitivity using solid wires with the help of a consumer-lever 3D printer. We were also able to, with a 3D printer, streamline the process of designing an MRI coil array and systematically optimize geometric decoupling which leads to a reduction in the number of iterations.

Higher unloaded/loaded Q ratio could be further improved by using thicker wires, copper wires coated with silver or tubular conductors. Nonetheless, our design shows a new method of designing an array coil with good unloaded/loaded Q ratio systematically. We demonstrated the application of 3D printing to building a one-dimensional receiver array for mouse imaging, but this method can also be applied to 2D arrays or even human-sized head arrays.

Instead of a 3D printer, it is also possible to build a coil former with the same features using a computerized milling machine. However, 5- or 6-axis CNC milling machines are required to manufacture coil formers with complex geometries. To achieve the same functionality and quality, milling machines are usually bulkier, less cost effective and less easy to use.

The limitation of consumer-level 3D printers is the precision. As demonstrated earlier, the actual dimensions of the printed object were 0.69%, 0.35% and 0.45% off from the original CAD design along the x-, y- and z-directions, respectively. While the error was seemingly small, it did affect the geometric decoupling. This error could be corrected by

either changing the firmware of the 3D printer or pre-compensating the dimensions in the CAD file, and we chose the latter for convenience. Before the dimensions of the CAD file were pre-compensated, the S_{21} of adjacent loop coils varied by up to 9 dB—depending on the location where the loop coils were installed. We were able to reduce the variation of the S_{21} of adjacent coils to 5 dB after the dimensions of the CAD design were pre-compensated. We believe that, with this kind of calibration, one can achieve more consistent performance if the coil former is outsourced using professional CNC machines or 3D printers for final production.

Finally, we demonstrated that using a 3D printer allows us to miniaturize the form factor of the coil assembly by integrating the array coil, the mechanical support, commercial auxiliary devices such as anesthesia delivery and respiratory/cardiac gating, and animal-handling mechanisms together. This is also very important because animal MRI scanners usually have a smaller bore size.

CHAPTER V

10-CHANNEL ARRAY COIL FOR AWAKE MARMOSET BRAIN IMAGING*

Synopsis

A 10-element head RF coil array was developed for imaging the brain of awake marmosets. A soccer ball design was used to improve whole brain coverage and parallel imaging acceleration of our previous designs. Coil clips and PLA cement were introduced to help with assembling small coil elements on irregularly shaped surfaces, and to optimize geometric decoupling. The proposed matching network provided independent adjustments of tuning, matching, active detune traps and preamp decoupling, which greatly simplified the construction of coil arrays in space-limited applications and enhanced image signal-to-noise ratio. Finally, molded-in foam padding was introduced to provide additional comfort during awake marmoset imaging, and motion-artifact-free images with enhanced cortical coverage were achieved for awake marmoset brain imaging.

Introduction

The common marmoset, *Callithrix jacchus*, is gaining popularity in neuroscience and pre-clinical research [131-136]. Functional neuroimaging studies require awake animals to allow the animal to actively attend to functional tasks, and to avoid the confounding effects

of anesthesia on neurovascular coupling [55-59]. Indeed, anesthesia-free animals show stronger and faster hemodynamic responses [27, 66].

We previously reported the development of individualized mechanical restraints and coil arrays for awake marmoset brain MRI [112, 137, 138]. Because each marmoset has a different skull size and shape, custom-made helmet systems, in conjunction with animal training, are used to stabilize the head position during awake marmoset imaging. A sheet of thin foam padding is glued inside of a helmet for the comfort of the marmoset. Individualized tailor-made coil arrays [112] and a one-size-fits-all coil array [137] are built between the foam padding and the helmet and outside of the helmet, respectively. However, it is difficult to apply a planer foam padding uniformly inside of the irregularly shaped helmet. Furthermore, after repeated use, we found that the thickness of the foam padding does not recover fully. In order to address these issues, the helmet is designed to be 1 mm tighter to compensate for the heterogeneous thickness distribution and the gradual thickness reduction of the foam padding. However, this extra tightness makes the marmoset less comfortable when a new helmet is being used.

As more array elements are used in the limited space inside an animal scanner, the use of traditional coil fabrication methods becomes increasingly challenging. Moreover, in our previous matching network design, shown in Figure 30(a), one inductor is shared between the noise matching and active detune trap, and it is sometimes difficult to optimize for both. For example, the inductor value is sometimes small (~3 nH) when the inductor is optimized for noise matching. Such a small inductor value compromises the performance

of the active detune trap because of the lower Q. In addition, the forward-biased PIN diode presents a short at the input of the preamplifier after half-wave cable, and this, when the matching capacitor fails or the transmit power is coupled to the matching network, promotes power matching from the output of the coil to the input of the preamplifier. Consequently, the preamplifier might be damaged.

Here we describe streamlined design techniques to develop a one-size-fits-all coil array for awake marmoset brain imaging. Matching network, coil clips and PLA cement were used to streamline the design and assembly process of the coil array, and a molded-in foam pad was used to increase the marmosets comfort. A specialized head-and-brain phantom was also proposed to help the development of the coil array. MR images of both the phantom and of the awake marmoset were used to evaluate the performance of the coil array.

Materials and methods

The marmoset head coil array was developed and tested on a 12-channel 7 Tesla Ultra Shielded Refrigerated pre-clinical MRI scanner (BioSpec 7T/30cm USR, Bruker Biospin MRI GmbH, Ettingen, Germany) interfaced to an Avance AVIII console (Bruker Biospin MRI GmbH, Ettingen, Germany). Only 10 out of the 12 receiving channels were used in this report. A previously developed [112] linear 16-rung birdcage coil with inner diameter of 110 mm was used as the transmitting volume coil. The helmet design for awake marmoset imaging was modified from the previous report [137] with minor improvements over the left-to-right symmetry. All *in vivo* marmoset imaging was performed under the

guidelines set by the Animal Care and Use Committee (ACUC) of National Institute of Neurological Disorders and Stroke (NINDS) in National Institutes of Health (NIH).

Construction of marmoset head-and-brain phantom

A head-and-brain phantom was developed and filled with 4.5 g/L saline and 0.5 mM Gadovist to help with the development and testing of the one-size-fits-all head coil array. The dimension and the shape of the phantom was based on a whole-head MRI of the largest marmoset in our colony using the volume coil and gradient echo sequence. The imaging parameters are shown in Table 3.

The 3D models of the head and the brain were individually generated using ITK-SNAP [139] (University of Pennsylvania, Philadelphia, PA, USA). Meshmixer (Autodesk, San Rafael, CA, USA) was used for further post processing. Small surface defects in the 3D models were smoothed, and the smoothed 3D models were mirrored to generate left-to-right symmetric 3D models. Shells of the head and the brain were generated with the wall thickness of 0.55 mm. The negative of the body-center-cubic structure was used to support the brain shell inside of the head shell. This structure consisted of cutouts of 6-mm spheres with 5.75 mm of distance between each sphere. Tubes were placed on the back of the head shell, and holes were placed on the brain shell at the occipital lobe, frontal lobe and brain stem to allow the dielectric solution to be filled inside of the brain shell. When the phantom was filled with the dielectric solution described above, the body-center-cubic structure inside of the phantom was used to help localize the volume of interest in the following imaging test. The phantom was printed on a Projet 3510 (3D Systems, Rockhill, SC, USA)

using VisiJet Crystal material at a resolution of 0.16 mm, and post-processed in a heated mineral oil bath to remove the internal wax used as support material. Figure 28(d) shows a cut-away view inside of the phantom, and (a-c) show the localizer MRI of the phantom. The brain shell was aligned along the AC-PC line and midline when all the repeated spherical pattern were of the same size on each localizer viewing plane.

Table 3. Imaging parameters for generating marmoset profiles and validation of coil performance.

Imaging Parameter	Generating head profile	Validation of coil performance	
		Phantom imaging	***In vivo brain imaging***
Sequence	3D FLASH[a], Flip angle = 30°	2D FLASH[a], Flip angle = 30°	2D RARE[b], RARE factor = 16
Repetition time (TR, ms)	15	700	9000
Echo time (TE, ms)	1.7	4.4	64
Average (NEX)	4	1	16
Field of view (FOV, mm^3)	76.8 x 76.8 x 76.8	51.2 x 51.2 x 24	40 x 32 x 30
Matrix size	160 x 160 x 160	256 x 256 x 24	200 x 160 x 60
Resolution (mm^3)	0.48 x 0.48 x 0.48	0.2 x 0.2 x 1	0.2 x 0.2 x 0.5
Total scan time	25 min 36 sec	2 min 59 sec	24 min 0 sec

[a] Fast low angle shot [140].

[b] Rapid acquisition with relaxation enhancement [141].

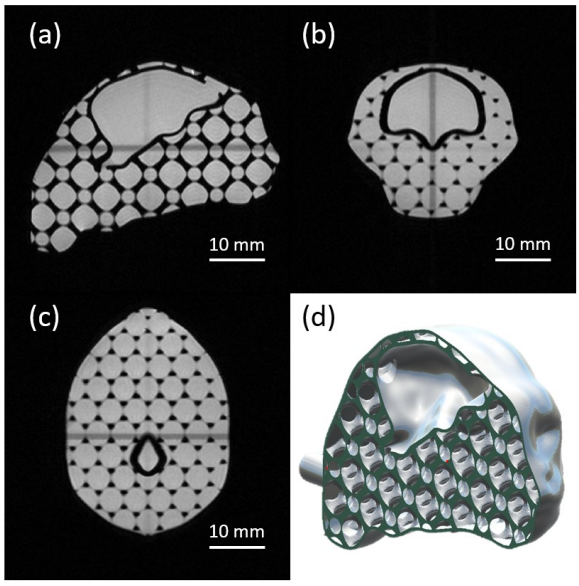

Figure 28. 3D model and MRI of head-and-brain phantom. (a-c) MR images of the custom phantom. When the ball pattern is aligned in 3 pilot views, the brain area is aligned with AC-PC line and midline. (d) Cross sectional view of the CAD design of the custom phantom. A "head shell" and a "brain shell" were derived from an MRI of a marmoset, and body-center-cubic structure was used to support the brain shell in the phantom. This phantom allowed us to localize the position of the brain area consistently and help evaluate SNR distribution inside of the brain area without the use of a marmoset.

Molded-in foam padding

An individualized helmet with molded-in foam padding was made for each marmoset. The outer profile of the helmet followed the design in our previous report [137]. The inner profile of the helmet was based on whole-head MRI of each individual marmoset using the same gradient echo sequence as shown in Table 3 and the following steps: ITK-SNAP was used to segment the head profile, and Meshmixer was used to smooth out minor surface defects of the head profile. Note that, contrary to the process that makes the head-and-brain phantom, the head profile was not mirrored here in order to better follow the

actual head profile of each individual marmoset. A mold plug was generated using the "Drape" command in Rhinoceros 3D (McNeel North America, Seattle, WA). The mold plug was isotropically enlarged by 2 mm, and therefore the inner profile of the helmet was generated in SolidWorks (Dassault Systèmes SolidWorks Corporation, Waltham, MA, USA). The helmet was 3D printed by a 3D printer (Replicator 2, MakerBot Industries, Brooklyn, NY) using polylactic acid material (PolyMax PLA, Polymaker, Shanghai, China) as shown in Figure 29.

Flow channels were added inside of the original mold plug, before 2-mm isotropic enlargement, using SolidWorks, and the mold plug was printed by a 3D printer (Dreamer, Flashforge, Jinhua, Zhejiang, China) using water-soluble polyvinyl alcohol material (PVA, LD Products Inc., Long Beach, CA, USA). The PVA mold plug was placed under the helmet, and a mixing syringe was used to inject two-part urethane foam (Flexible Foam, Alumilite, Kalamazoo, Michigan, USA) into the flow channel and eventually filled up the space in between. Once the foam padding was cured, the entire assembly was soaked in water to remove the PVA mold plug. After the foam was dried and trimmed, the conforming 2-mm thick foam padding was embedded under the custom-made helmet. Because part of the urethane foam entered the porous 3D-printed helmet, the urethane foam lining and the helmet became inseparable after the urethane foam was cured. Figure 29(d) shows the helmet with embedded urethane foam lining after the PVA mold was dissolved and excessive foam padding was removed.

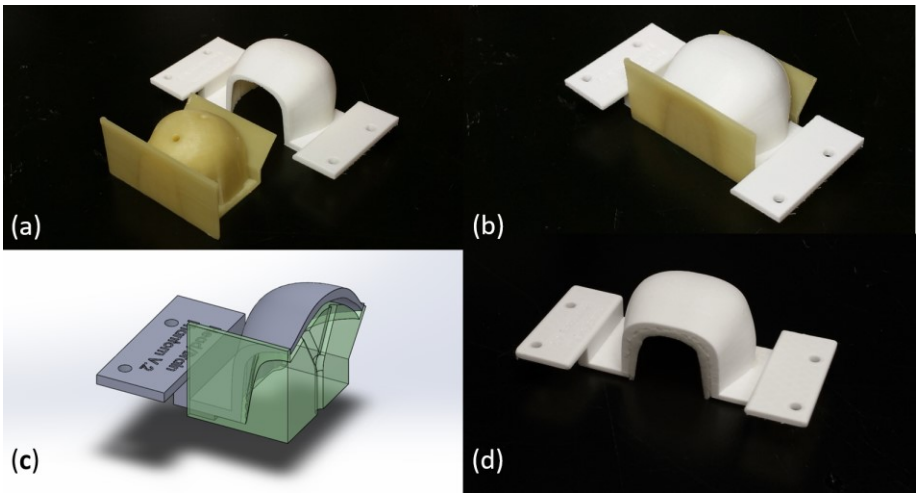

Figure 29. Marmoset head helmet with molded-in foam padding. (a) A marmoset helmet was 3D printed using a Replicator 2 3D printer and PolyMax PLA material in white. The mold plug in yellow was 3D printed using a Dreamer 3D printer and water-soluble PVA material. (b) The PVA was placed centered and under the PLA helmet waiting for the injection of two-part urethane foam. (c) The cut-away view shows the y-shape injection channels. The excessive urethane foam exits from the small gaps between the mold plug and the helmet at the back. (d) Because the PLA helmet is porous, part of the urethane entered the helmet before it is cured. Once the urethane is cured, the foam padding and the helmet became inseparable. After the foam padding is dried and trimmed, the inside of the helmet is embedded with urethane foam.

Matching network

A circuit diagram of the receive-only coil elements is proposed in Figure 30(b). Each receiving coil was tuned to 300.35 MHz and noise matched individually before the coils were mounted on the coil former. Fixed-value capacitors C_{t1}, C_{t2} (Passive Plus, Huntington, NY) and variable capacitor C_{tv} (1-5 pF, 9402-1, Johanson Manufacturing, Boonton, NJ, USA) were used to tune the coil frequency, and C_m‘ was used for noise match. The inductor L_d was used to form an active detune trap with the fixed tuning capacitors C_{t2} when the PIN diode (MA4P7470F-1072T, M/A-COM Tech, Lowell, MA,

USA) was forward biased. Two RF chokes (0805CS-681X, Coilcraft, Cary, IL, USA) were placed orthogonal to each other and provided 50 dB isolation between the RF line and the PIN diode signal line. L_p and C_p were added in conjunction with a coaxial cable connecting the coil to the preamplifier for proper preamplifier decoupling.

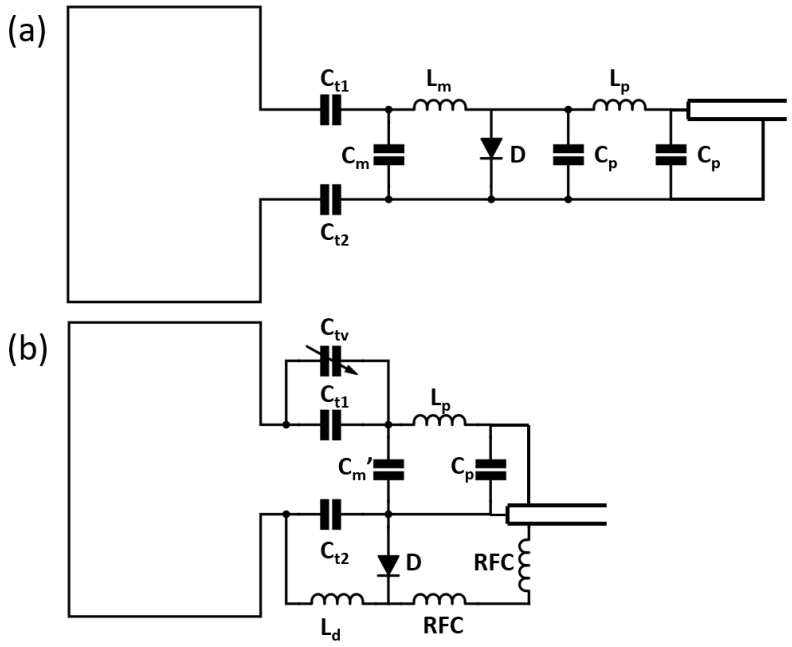

Figure 30. Comparison of the previous and the proposed matching network. (a) Our previous design. (b) The proposed circuit diagram of the coil. Previously, L_m is used for both matching and active detuning trap. However, because L_m is usually very small (~3 nH) when the coil is matched to 50 Ohms, performance of the active detuning circuit is low. A common solution is to sacrifice matching by increasing the value of L_m for better active detuning. In the new design, tuning, matching, active detuning and phase shifter can be adjusted independently, so that no compromises are necessary and optimal coil performance can be achieved. Component values: trimmer capacitor C_{tv} = 1-5 pF, tuning capacitor C_{t1} = 10 pF and C_{t2} = 12 pF, matching capacitor $C_m = C_m' - C_p$ = 33-68 pF. Component values of Lp and Cp of the phase shifter were determined for proper preamplifier decoupling.

Single-coil comparison using traditional and proposed matching network

Three wire-based coils of the same dimension were made with the traditional, the proposed and the control matching networks individually. All coils were made out of the same AWG16 wire, and the same set of stamping tools were used to bend the wire into the same shape. The matching networks were designed in EAGLE with the same trace width, similar sizes of soldering pads and similar distance between each passive components. The networks were produced by a milling machine (MDX-40A, Roland DG Corporation, Japan) with the same sets of milling bits. All three wire loops were soldered on the traditional, the proposed and the controlled networks individually.

For the traditional matching network, one can only prioritize either proper noise matching or a better active detune trap because C_m and L_m are used for both purposes as shown in Figure 30(a). Although choosing larger L_m and smaller C_m can achieve better active detune, the noise matching would suffer. As a compromise, we focused on sufficient active detune over proper noise matching because better active detune is more desirable for the development of coil arrays. For one, better active detune trap is needed to adjusting preamplifier decoupling of each individual receiving coil. Secondly, better active detune reduces the noise contributed from the transmitting coil. We chose L_m = 5.5 nH and C_m = 30 pF and achieved active detune = 21 dB. Increasing L_m would yield even better performance on the active detune trap, but it would also have made the noise matching even worse. A variable capacitor C_{tv} (1-5 pF, 9402-1, Johanson Manufacturing, Boonton, NJ, USA) was added parallel to the fixed-value tuning capacitor C_{t1} for the convenience

of tuning the frequency of the coil, and The S_{11} was -1.9 dB when the coil was fine tuned to the Larmor frequency of 300.35 MHz.

For the proposed matching network, components were chosen to adjust for the frequency tuning, noise matching and active detune trap. The control matching network used the same design as the proposed one, except that the matching capacitor $C_m \approx C_m$‘ was replaced with the same 30 pF capacitor used on the traditional matching network instead of the 75 pF capacitor used on the proposed one.

Phase shifters were still adjusted on all three coils for proper preamplifier decoupling to compare the performance of preamplifier decoupling between different matching networks. The component values used on the three coils are shown in Table 4.

Table 4. Components used for single-coil comparison using traditional and proposed matching networks.

Matching network	C_{tv} (pF)	C_{t1} (pF)	C_{t2} (pF)	C_m or C_m‘ (pF)	L_m (pF)	C_p (pF)	L_p (pF)	L_d (nH)	Cable length (cm)
Traditional	1-5	15	12	30	5.5	1.8	8.9	N/A	21
Proposed	1-5	12	12	75	N/A	1.8	8.9	19.4	24
Control	1-5	15	12	30	N/A	1.8	8.9	19.4	26.5

Unloaded-versus-loaded Q ratio was measured using a pair of decoupled (< -75 dB) loop probes and a 5-cm ball phantom filled with 0.5 mM Gadovist and 4.5 g/L saline. The coils were resonated at 300.35 MHz without connecting the phase shifters and cables. The coil was placed directly on the top of the phantom under the loaded condition.

Another pair of decoupled loop probes were mounted with mounting tape (Scotch Extreme Mounting Tape, 3M, St. Paul, MN, USA) on the coil former, and S-parameters were used to measure the performance of preamplifier decoupling and active detune traps. The head-and-brain phantom described above was used as the load of the receiving coils to be tested. Different amount of probe-probe decoupling and averages on the network analyzer were used for the measurement of preamplifier decoupling (< -90 dB and 200 averages) and active detune trap (< -98 dB and 500 averages). The preamplifier decoupling was measured through the difference of S_{21} when a coil was connected to a 50 Ω load and the preamplifier. When performing these bench comparisons, three coils were individually mounted and aligned with the fiducial mark on the coil former between the two decoupled loop probes.

Phantom imaging was used to compare the SNR performance of the three matching networks. Coils were mounted and aligned on the coil former in the same manner as the setup of the bench comparison except that the decoupled probes were removed before the imaging.

Construction of receiving coil array

To build a one-size-fits-all head array coil, the coil former was designed to conform to our previously reported head-restraining helmets [137]. In this report, a soccer ball pattern [142] of the 10-element receiving coil array was projected onto the coil former as fiducial marks in SolidWorks as shown in Figure 31. The actual dimension of the fiducial marks (20 and 27 mm for the pentagonal patch and hexagonal patch respectively) was determined to achieve optimal geometric decoupling. The pentagonal patch of the soccer ball was placed on the top of the helmet. With this arrangement, 3 coils exceeded the boundary of the helmet and therefore the circular-shaped loop coils had to be truncated. As a result, one non-circular loop had to be used on the top of the forehead and two more on both sides of the cheeks. We noticed that it was necessary to change the amount of overlap between the non-circular coil element and its neighboring element for geometric decoupling. To this end without perturbing the general location and dimension of the coil array, we adjusted the amount of overlap locally by 1 to 2 mm between these non-circular loop elements and their neighboring coils. Note that it was also possible to place the hexagonal patch of the soccer ball on the top of the helmet and thus form an 11-element receiving coil array. However, this arrangement would have resulted in two more non-circular loop elements which made the 11-element design less desirable.

To follow the natural shape of a marmoset head, AWG 14 wire was used for constructing Coil 1, 2, 9 and 10, as shown in Figure 31, and AWG 16 wire was used for the remaining 6 coils. The nominal size of the smaller coils was 2 cm, and the size of the larger coils was 2.7 cm. Custom stamping tools were 3D printed using PLA material, and each coil body was shaped by its own set of stamping tools to form the coil bridges where the coil elements overlap. All coil elements were fully populated, except the phase shifters, before individual coils were mounted on the coil former.

The coil former was 3D printed by Replicator 2 using PolyMax PLA material. The top enclosure of the coil was printed by Fortus 360mc (Stratasys Inc., Eden Prairie, MN, USA) using polycarbonate building material and SR-100 soluble support material. The outer surface of the coil former and the top enclosure was painted with MR compatible paint (EPO-TEK 301, Epoxy Technology Inc., Billerica, MA, USA) to seal the porous surface and the ease of cleaning.

3D-printed PLA coil clips were used to mount the coils by fusing the clips onto the coil former with tetrahydrofuran solvent. The ~0.2 mm tolerance of the coil clips allowed fine adjustment for the optimization of geometric decoupling. PLA cement was made by dissolving recycled PLA material into tetrahydrofuran, and the cement was applied on the coil clips to permanently secure the coils after the geometric decoupling was optimized as seen in Figure 32.

To ease the challenge of geometric decoupling in confined space, an outside-in approach was used to mount the 10 receiving coils on the coil former. The outer elements Coil 1

and 9 were installed first and followed by Coil 2 and 10. The rest of the elements were installed in the spiraled-in fashion with the order of Coil 3, 4, 8, 7, 5 and 6. This maintained the left-to-right symmetry and achieved geometric decoupling without iteration.

Small floating cable traps (outer diameter/length = 8 mm/12 mm) [143] were installed on coaxial cables (Temp-Flex 50CX-41, Molex, Lisle, IL, USA) close to the matching network of each coil, and large floating cable traps (outer diameter/length = 22.9 mm/35 mm) were installed at every quarter-wave length. Multi-pin RF connectors (ODU GmbH & Co. KG, Pregelstraße, Germany) were used to connect the coil array to our in-house developed preamplifier modules.

The matching capacitors were adjusted after all 10 coil elements were secured on the coil former, and the coils were tuned back to 300.35 MHz using the 1-5 pF variable capacitors. Phase shifters were added for proper preamplifier decoupling.

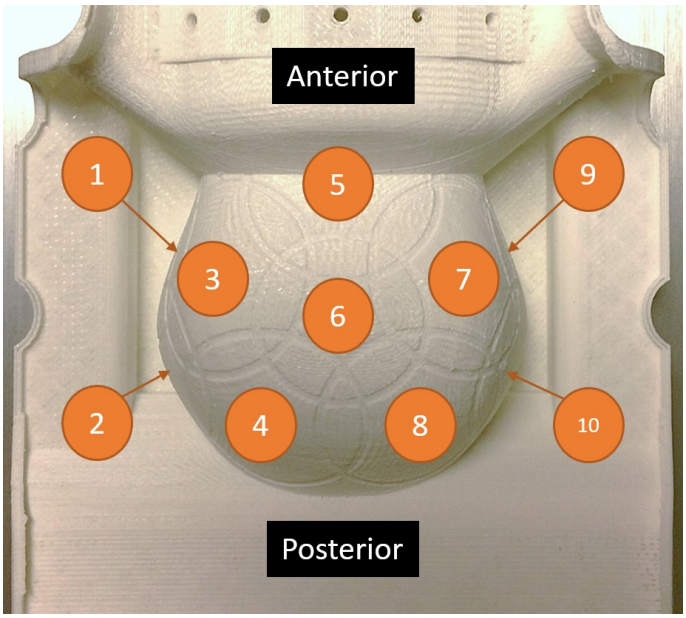

Figure 31. Spatial arrangement of 10-channel marmoset head coil array. Coil 6 corresponds to the pentagonal patch of a soccer ball. It is placed on the top the marmoset head. The dimension of each circular loop is determined for optimal geometric decoupling. Coil 1, 5 and 9 used non-circular loops because they were placed at the boundaries of the coil former. The amount of geometric decoupling between these non-circular loops and their neighboring elements need to be adjusted because the amount of magnetic flux going through these loop elements is changed.

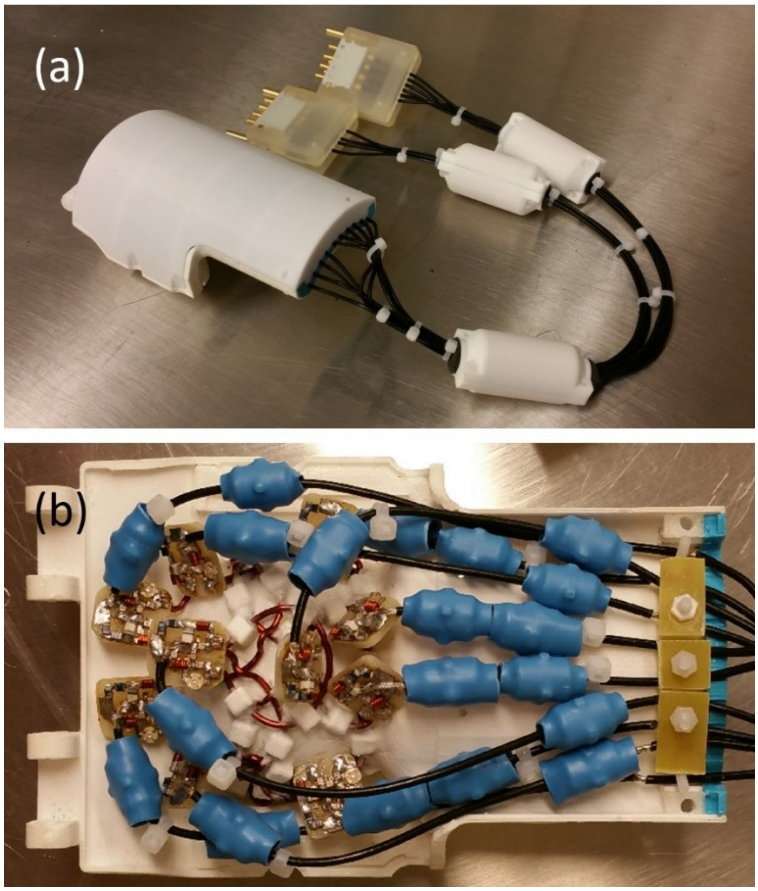

Figure 32. 10-channel head coil array for *in vivo* marmoset brain imaging. (a) Photo of 10-channel head coil array with large floating cable traps placed at every quarter-wave. (b) The lid of the coil enclosure is removed to show the soccer ball construction. Small floating cable traps were wrapped by blue heat-shrink tubes. Each receiving coil was mounted by using 3D printed cable clips. Each clip was first fused with the coil former by tetrahydrofuran solvent, and the gap between the clip and the coil was filled by PLA cement after geometric decoupling was optimized. This technique allowed streamlined construction of coil array in the space-limited application.

Bench measurements of receiving coil array

A custom-made testing rig and a network analyzer (Agilent Technology, Santa Clara, CA, USA) were used for bench measurements. Coils were connected to in-house developed preamplifier modules via ODU multi-pin connectors. Preamplifiers were connected to the

custom rig which provides 10 V power to the preamplifiers, 50 Ωterminations for the preamplifier outputs, and PIN diode signals to enable/disable individual coils. Tuning and noise matching were performed when the coil array was loaded with the proposed head-and-brain phantom, and an individual coil was connected to the network analyzer while other coils were active detuned through the custom testing rig. The performance of the active detune trap was measured using the difference of S_{11} measurements before and after the PIN diode on the coil was forward (+5 V) biased.

A geometrically decoupled (<-75 dB) double-loop probe was used for S_{21} measurements. The unloaded to loaded Q ratio of a resonated loop coil without matching network was measured using the double-loop probe. The Q ratio of each coil was measured again when the coil array was fully populated and non-testing coils were actively detuned. The performance of the preamplifier decoupling was measured by the difference of S_{21}measurements before and after each coil was power matched (connected to a 50 Ωtermination) and noise matched (low-input impedance preamplifier termination) [144].

Phantom and in vivo imaging

The coil performance was evaluated on a phantom and a marmoset *in vivo* using a fast low angle shot (FLASH) and spin-echo sequences respectively. The imaging parameters are shown in Table 3.

Noise correlation matrix was used to validate the coil-to-coil isolation. The coil array was loaded with the proposed phantom, and noise-only images n_i and n_j of the *i*-th and *j*-th

coils were acquired without RF excitation [110] to calculate the noise covariance coefficient

$$\Psi_{i,j} = \langle (n_i - \mu_i) \cdot (n_j - \mu_j)^* \rangle,$$

where μ_i and μ_j are the complex mean of images n_i and n_j. The noise correlation between coils was calculated using

$$\Psi_{ij}^{corr} = \Psi_{ij} \left(\Psi_{ii} \Psi_{jj} \right)^{-1/2}.$$

The calculation of noise correlation stated above was implemented on an in-house developed MATLAB script and the built-in CORRCOEF function.

The performance of signal-to-noise ratio (SNR) of the proposed 10-channel marmoset head coil array with soccer ball arrangement was compared to our previously reported [137] 8-channel marmoset head coil array. Both coil arrays were developed to work with our helmet system for awake marmoset brain imaging. Phantom imaging was used to calculate the SNR maps of these two coil arrays. G-factor maps with acceleration factors of 2X, 3X and 4X along anterior-posterior (A-P) and left-right (L-R) directions were used to evaluate the distribution of increased noise under different acceleration conditions.

Results and discussions

The proposed design allowed independent development of frequency tuning, noise matching, active detune trap and phase shifter. When the coil elements were installed on the coil former and copper loading was increased, matching capacitors were replaced to

maintain noise matching. The variable capacitor was used to adjust the frequency of the coil back to 300.35 MHz. Unlike the traditional matching network shown in Figure 30(a), these adjustments did not affect the performance of the active detune trap, therefore L_d did not need to be changed. Phase shifters were added to each individual coil for preamp decoupling, which transformed the low input impedance of the preamplifier to a shunt inductance to form high impedance across the shunt matching capacitor. This reduced the current flowing on the coil induced by inductive coupling from adjacent coils. The added phase shifters did not affect the detuning, matching or the active detune trap.

Note that C_m' was shared between noise matching and phase shifter, but this did not affect the streamlined design process. $C_m' = C_m + C_p$ where C_m was the matching capacitor and C_p was the capacitor used for the phase shifter. Sometimes $C_m >> C_p$, depending on the angle of the phase shifter, and C_m does not need to be replaced with C_m' to maintain proper noise matching. For other times, C_p was simply soldered on top of C_m without replacing C_m with C_m'.

Single-coil comparison using traditional and proposed matching network

As shown in Table 4, similar component values were chosen for all three matching networks to reduce variations from the passive components. The cable lengths of the three coils were slightly different to adapt for the preamplifier decoupling, but the difference of cable loss should be minimal.

The bench comparison of traditional and proposed matching network is shown in Table 5. The traditional, proposed and control matching network showed similar unloaded-versus-

loaded Q ratio before they were matched and connected to a 50 Ω termination. This indicated good consistency of the coil dimension, and the subsequent differences of bench measurements should not be related to the body of the coil.

Because both the traditional and the control matching networks were not matched to 50 Ω, their S_{11} measurement was similarly underperformed. On the other hand, the proposed matching network showed S_{11} = -25 dB which indicates good matching. While the 6-dB bandwidths of preamplifier decoupling were similar among three networks, the preamplifier decoupling of the proposed matching network was slightly lower while the performance of traditional and the control matching network were similar. This was the result of the higher shunt capacitor used on the proposed network (75 pF) versus the lower shunt capacitor (30 pF) used on both the traditional and the control networks. Nonetheless, proposed matching network still showed very usable preamplifier decoupling of 22 dB. However, the proposed matching network showed significantly smaller distance between horns of preamplifier decoupling. This difference was again because of the choice of shunt capacitors used on the 3 matching networks. This means that the matching network uses a large-value capacitor requires more precise tuning of the phase shifter to ensure the preamplifier decoupling works properly.

Single-channel imaging test showed that the coil made out of proposed matching network showed generally higher SNR in Figure 33. In Figure 34, one-dimensional SNR comparison showed 28±6.2% and 24±4.1% of SNR increase in the brain region when the proposed matching network was used.

Table 5. Single-channel comparison of traditional and proposed matching network.

Bench measurement	Traditional	Proposed	Control
Q_{ul}/Q_l	2.22	2.24	2.29
S_{11} (dB)	-1.9	-25	-2.2
Active detune (dB)	45	50	44
Preamplifier decoupling (dB)	25	22	26
Preamplifier decoupling: 6-dB bandwidth[a] (MHz)	2.1	2.0	1.8
Preamplifier decoupling: distance between horns[b] (MHz)	16.3	4	17.4

[a] 6-dB bandwidth: distance between frequency points which are 6 dB higher than the mid-frequency which has the highest preamplifier decoupling/lowest S_{21} value.

[b] Distance between horns: distance between frequency points which are the highest peaks on the S_{21} plot when measurement of preamplifier decoupling is performed.

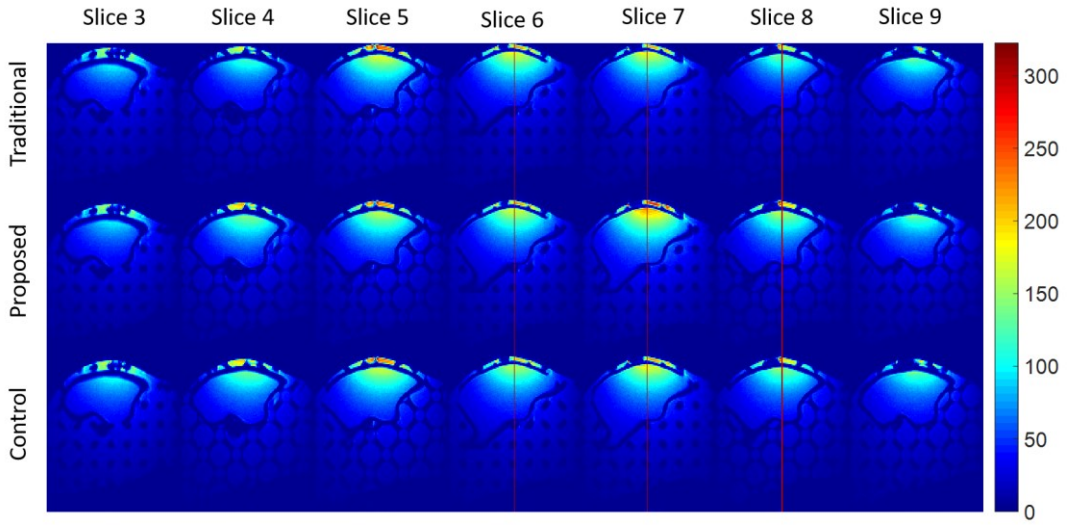

Figure 33. Comparison of SNR maps between coils using traditional, proposed and control matching networks. Phantom images were acquired to comparison the SNR maps at sagittal view. The distance between each sagittal SNR map is 2 mm. The red lines on Slice 6 to 8 indicate the location of 1D comparison of SNR distribution among coils made with these three different matching networks. The coil with proposed matching network showed generally higher SNR from Slice 4 to Slice 8 which are -5 mm and 5 mm from the center slice respectively.

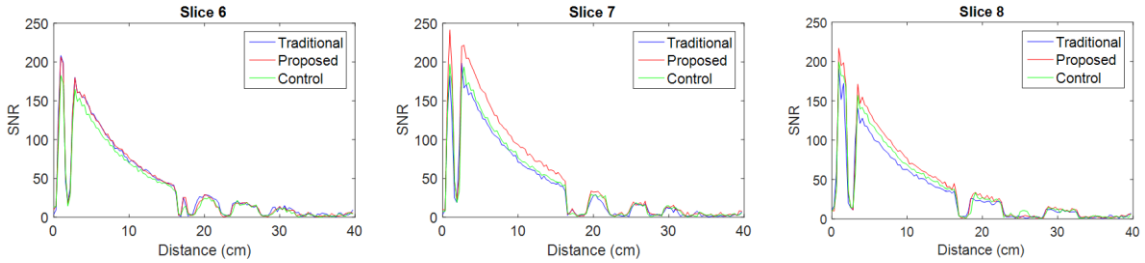

Figure 34. Comparison of SNR distribution among coils made with traditional, proposed and control matching network. One-dimensional SNR distribution is plotted. Note that the horizontal axis, Distance (cm), is plotted from the edge of the field of view, instead from the location of the coil. The coil is roughly 5 mm away from the edge of the FOV. Slice 6 is the center slice, Slice 7 and Slice 8 are 2 mm and 5 mm away from Slice 6 respectively. The location of brain on Slice 6, 7 and 8 are 2.81 to 15.94 cm, 2.5 to 16.25 cm and 3.44 cm to 16.25 cm respectively. The three coils showed similar SNR performance at the center images, and the coil with the proposed matching network showed 1.28±0.06 and 1.24±0.04 times of SNR in the brain region when compared to the coil with traditional matching network on images 2 mm and 5 mm away from the center image.

Performance of head coil array

Because the proposed matching network allowed individual adjustments of tuning, matching, active detune trap and phase shifter, the proposed matching network largely reduced the tedious and iterative work throughout the fabrication of the 10-channel marmoset coil array. In addition, because the PIN diode was moved away from the main RF signal path and isolated by RF chokes, the matching network would not power match to the preamplifier when some of the passive components failed. This helps to prevent the preamplifiers from being damaged when failure mode occurs. The physical length of the new circuit design was also shorter, and the reduced length helped with fitting extra coil elements in the limited space. All 10 coil elements were tuned to 300.35 MHz and noise matched to 50 Ω (S_{11} < - 21 dB) when the array was loaded with the phantom. The active detune trap achieved an uncompromised performance of 45 dB isolation when a 22 nH inductor was used to resonate with the 12 pF tuning capacitor. Phase shifters were installed to achieve 24±5.7 dB of preamp decoupling among all 10 receiving coils. Unloaded-to-loaded Q ratios were measured (Coil 1 to 10): 1.19, 1.15, 1.13, 1.10, 1.07, 1.09, 1.10, 1.14, 1.13 and 1.2, down from 1.23 and 1.20 when single coils made out of AWG14 and AWG 16 wire. This showed that the coil elements at the center of the head coil array suffered more from the inductive loss. Note that the measurement of unloaded-to-loaded Q ratios of the single coils were a lot lower than the ones (2.22 to 2.29) showed in Table 5. This was because the unloaded-to-loaded Q ratio here was measured when the single coil and the phantom was separated by a coil former, a helmet and one layer of molded urethane foam, while the unloaded-to-loaded Q ratio in Table 5 was done when the single coil was

mounted directed on top of the phantom. This comparison also showed the amount of sacrifice we made for animals comfort over the coil performance in awake marmoset brain imaging.

The noise correlation matrix showed satisfactory coil isolation in Figure 35. This confirmed the efficacy of geometric decoupling and preamplifier decoupling with the proposed matching network.

Phantom images showed that the 10-channel coil array present 1.83, 1.70, 1.87, 2.37and 2.62 times SNR over the transmitting volume coil at the center of the brain, occipital, temporal, frontal, and parietal lobe areas, respectively. When compared to our previously reported 8-channel marmoset head coil array as shown in Figure 36, the proposed 10-channel head coil array showed 17±0.69% of SNR improvement at the center of the brain area. SNR was improved by 27±14% at cortical areas except occipital lobe where the proposed array showed almost no SNR improvements. This was because, for both coil arrays, the occipital lobe was far away from the posterior coil elements, and the posterior coil elements were placed closely perpendicular to the direction of B_0 field.

G-factor maps and GRAPPA images showed minimal SNR reduction when 3X acceleration was used along the right-left or the anterior-posterior direction as shown in Figure 37. This confirmed the good coil isolation provided by geometric decoupling and preamplifier decoupling. This also demonstrated the benefit of increased coil number in the accelerated imaging which is important for awake marmoset brain imaging.

To demonstrate the efficacy of the 10-channel marmoset brain coil array, awake marmoset brain images (Figure 38) showed good sensitivity and contrast over the entire marmoset brain without noticeable motion artifact.

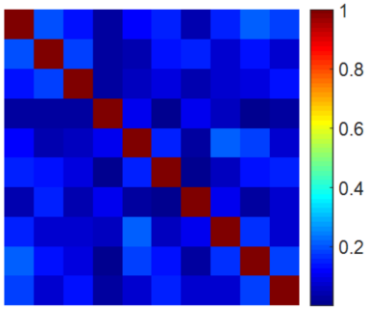

Figure 35. Noise correlation matrix of the 10-channel marmoset head coil array.

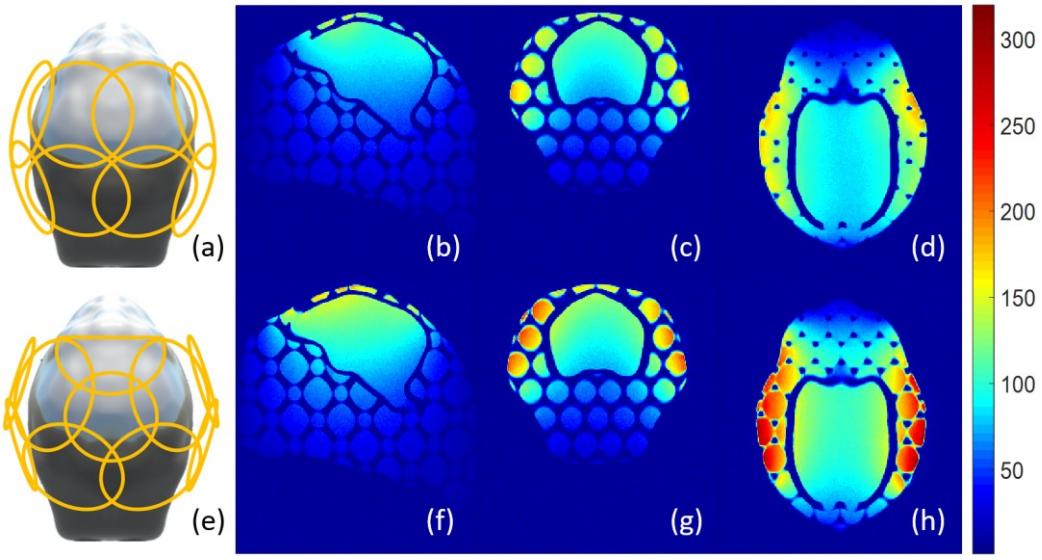

Figure 36. Comparison of SNR maps between previously reported 8-channel marmoset head coil array and the proposed 10-channel coil array with soccer ball arrangement. (a and e) are the cartoon illustrations of the arrangement of coil elements of the previous 8-channel coil array and the proposed 10-channel coil array relative to a marmoset head. (b-d) and (f-h) are sagittal, coronal and axial views of SNR maps of the previously reported 8-channel array and the proposed 10-channel coil array.

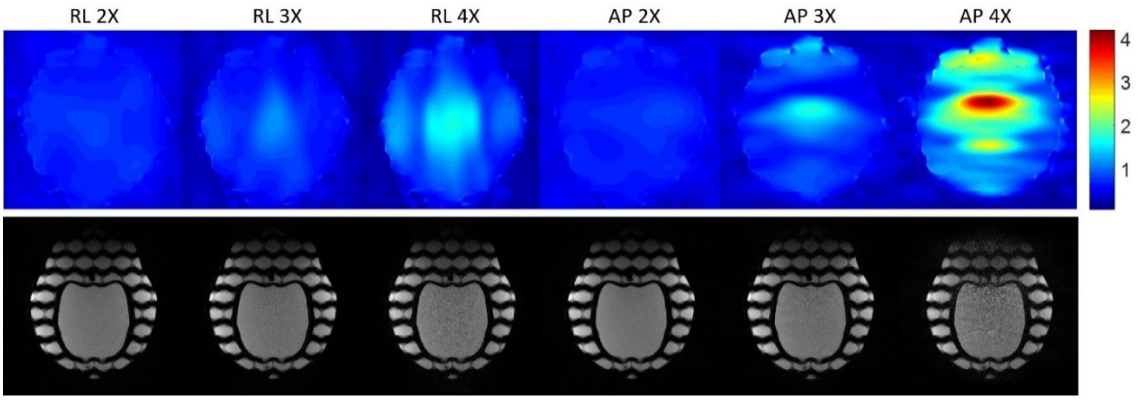

Figure 37. Axial views of g-factor maps with 2, 3 and 4 acceleration factors along right-left and anterior-posterior directions and their corresponding GRAPPA reconstruction. 3X acceleration along R-L and A-P directions show a satisfactory compromise between acceleration and minimal SNR reduction.

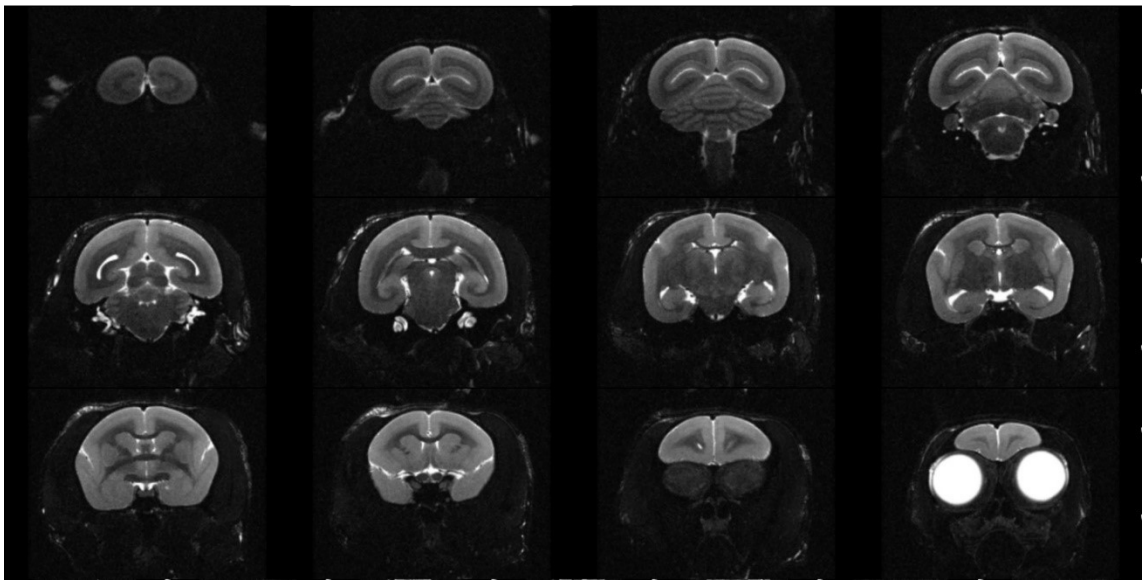

Figure 38. *In vivo* marmoset brain imaging shows excellent sensitivity and homogeneity over the entire marmoset brain.

Conclusion

Because phased array coils for small-animal imaging are usually built in tight spaces, iterating capacitor/inductor values throughout the fabrication of the array is difficult. With the streamlined design developed here, replacing components throughout the process of coil development is largely reduced, and the performance of each individual element is not compromised. The new molded-in foam padding does not shrink and provides perfect fit for the marmoset every time, and increases the marmosets' comfort.

As a result, the proposed design showed better decoupling among coil elements and thus enabled better accelerated parallel imaging compared to that of our previous coil array [137]. This work will greatly improve the quality of awake marmoset brain imaging for ongoing neurovascular studies.

CHAPTER VI

12-CHANNEL ARRAY COIL FOR MARMOSET SPINE IMAGING

Synopsis

A 12-channel receive-only coil array was developed for *in vivo* imaging of marmoset whose spinal cords were being studied as disease models of multiple sclerosis, tumor and spinal injuries. The array is comprised of 6 shifted pairs of loop and butterfly elements arranged in an anatomically conforming coil former. Shifting the elements within each pair reduced inductive coupling and produced consistent sensitivity throughout the entire spinal cord—including cervical, thoracic and lumbar areas. The substantial increase of SNR enabled high-resolution *in vivo* imaging of marmoset spinal cords. The design of coil former also increased animal safety and reduced setup time over 80%.

Introduction

Common marmosets (*Callithrix jacchus*), a type of New World monkey, are gaining popularity due to their features of smaller body size, shorter time to maturity, shorter gestation period and easier breeding. Compared with mice, marmosets also have longer lifespans [20-29]. In addition, using marmosets as a pre-clinical research model can be advantageous in studies, such as those involving the spinal cord, because the neural functions and anatomies of non-human primates are more similar to humans than rodents [145-152]. Further, Kanehiro *et al.* reported that transplantation of human neural progenitor cells into a damaged marmoset spinal cord promotes functional recovery [153]. This suggests the compatibility of neural progenitor cells between marmosets and humans.

In addition, marmosets are naturally occurring bone marrow chimeras, therefore they are tolerant of each other's bone marrow-derived cells even though the animals are genetically different [152, 154]. This feature is important for developing disease models such as multiple sclerosis in the spinal cord and alleviates the problem of individual phylogenetic differences because non-human primates are usually outbred [152].

To study the integrity of spinal cords in disease models or spinal cord injury (SCI), the conventional trace-based method is highly invasive [145, 147, 155]. Magnetic resonance imaging (MRI) offers a non-invasive method and provides a variety of contrast mechanisms and versatile imaging functionalities that are powerful both in human and animal studies. *In vivo* T1-/T2-weighted imaging [146, 153, 156-158] and diffusion tensor imaging (DTI) [145, 151] of marmosets have been used for evaluation of SCI including hemorrhage, edema and cavity formation. However, only the cervical area was imaged by MRI in these reports. Kelley *et al.* reported *ex vivo* DTI of the entire spinal cord, which was segmented and flat mounted on a surface coil, on a 9.4 Tesla system. However, *ex vivo* imaging is limited in longitudinal studies of recovery from SCI.

Various MRI coils have previously been developed for studying human spinal cords. The earliest quadrature pair for imaging the human lumbar spine was reported in 1988 [159]. Roemer et al. demonstrated the first MRI phased array that images the entire human spine [37]. The phased array consists of 4 receiving loop elements which increases signal sensitivity and spatial coverage. Later, a 12-element coil array consisting of six loop-butterfly pairs was used to image the entire human spine [160]. The signal of each pair of

loop and butterfly elements is combined by a quadrature hybrid, and different parts of the spine also can be selectively imaged through the control of PIN diode signals.

While marmoset models of spinal cord lesions are promising [145, 146, 151-154, 156-158, 161-163], to date there are no specialized coil arrays available for high-resolution imaging of the entire marmoset spinal cord *in vivo*. More importantly, when engineering MRI hardware for small animal models, the design and finished product should help streamline animal experiments and meet the ever changing needs of the research community. To this end, the design and implementation of a 12-channel receive-only RF coil array is described. Furthermore, a whole-body conforming coil former was developed to streamline the experimental setup and reduce the risk of anesthesia-induced hypothermia.

Materials and methods

The marmoset spine coil array was developed and tested on a 12-channel 7 Tesla Ultra Shielded Refrigerated pre-clinical MRI scanner (BioSpec 7T/30cm USR, Bruker Biospin MRI GmbH, Ettingen, Germany) interfaced to an Avance AVIII console (Bruker Biospin MRI GmbH, Ettingen, Germany). All *in vivo* marmoset imaging was performed under the guidelines set by the Animal Care and Use Committee (ACUC) of National Institute of Neurological Disorders and Stroke (NINDS) in National Institutes of Health (NIH).

Construction of marmoset body-and-spine phantom and coil former

A body-and-spine phantom was designed and filled with 4.5 g/L saline and 0.5 mM Gadovist to help with the development and testing of the one-size-fits-all spine coil array.

The dimension and the shape of the phantom was based on a whole-body MRI of one of the largest marmosets in our colony. The anesthetized marmoset was laid in the most relaxing and stable supine position on stacks of cotton pads. The neck of the marmoset was elevated to follow the shape of the intubation tube and accommodate the isoflurane connections. The lumbar area was also elevated to help stabilize the position of the marmoset body. The MRI scan was performed using a 3D-FLASH sequence [140] (Table 6) and the previously developed [112] linear 16-rung birdcage coil with inner diameter of 108 mm. Because of the limitation of the diameter spherical volume (DSV), the top, middle and bottom segments of the marmoset body were scanned separately, and the 3 segments were stitched into one whole-body data set manually using Mipav [164] (National Institutes of Health, Bethesda, MD, USA).

Using ITK-SNAP [139] (University of Pennsylvania, Philadelphia, PA, USA), the body and the central nervous system (CNS) were segmented into separate binary masks. The masks were imported into Mipav and converted to 3D surfaces using a surface extraction algorithm.

The 3D surfaces were imported into Netfabb Professional (Autodesk, San Rafael, CA, USA) and surface repair and smoothing algorithms were applied. The body was then cut down the midline and mirrored to create a right-to-left symmetric body. In Meshmixer (Autodesk, San Rafael, CA, USA) a pattern of tiled spheres (10 mm diameter, 9.5 mm spacing, regular/Cartesian pattern) was subtracted from the solid marmoset body. The resultant grid of empty spheres was then combined with a hollow, 1.5 mm offset, body

shell and converted to a solid part. This creates a grid of regular hollow spheres inside of the body shell, of which the CNS 3D surface was then subtracted. The result of this subtraction is then combined with a 1 mm offset, hollow shell of the CNS surface and converted to a solid part. To allow for proper filling and sealing of the phantom, 6 tubes (3.3 mm inner diameter, 5.8mm outer diameter, 1 screw in the brain cavity, 1 in the lumbar spine, 2 in the head shell, 2 in the lower body) were added to accommodate #4 screws. The resulting phantom is 172.5 mm x 60.8 mm x 58.75 mm. The phantom was printed on a Projet 3510 (3D Systems, Rockhill, SC, USA) using VisiJet Crystal material at a resolution of 0.16 mm, and post-processed in a heated mineral oil bath to remove wax support material.

To design the coil former, the same 3D model of the marmoset body was used. The coil former was designed according to the 3D body model with the body size expanded by 5 mm laterally in SolidWorks (Dassault Systèmes SolidWorks Corporation, Waltham, MA). This extra space allowed us to further maintain the body temperature by wrapping a cotton sheet under the marmoset body. The fiducial marks were etched on the coil former to guide the assembly of the coil array. The coil former was 3D printed by Replicator 2 (MakerBot Industries, Brooklyn, NY) using polylactic acid material (PolyMax PLA, Polymaker, Shanghai, China). The coil cover was 3D printed by Fortus 360mc (Stratasys Inc., Eden Prairie, MN, USA) using polycarbonate building material and SR-100 soluble support material.

Table 6. MRI parameters for generating whole-body marmoset profile and for validation of coil performance.

		Validating coil performance				
			In vivo spine imaging			
				Axial		
Imaging Parameter	**Generating phantom and coil former (all 3 segments)**	***Phantom imaging (all 3 segment)***	***Sagittal (all 3 segment)***	***Top segment***	***Mid segment***	***Lower segment***
Sequence	3D FLASH[a], Flip angle = 30˚	2D RARE[b], RARE factor = 2	2D RARE[b], RARE factor = 2	2D RARE[b], RARE factor = 2	2D RARE[b], RARE factor = 2	2D RARE[b], RARE factor = 2
Repetition time (TR, ms)	50	700	3500	3500	3500	3500
Echo time (TE, ms)	3	10	15	15	15	15
Average (NEX)	1	1	4	4	4	4
Field of view (FOV, mm^2)	102.4 x 102.4	64 x 62	50 x 32	26 x 39	24 x 32	24 x 32
Matrix size	128 x 128	256 x 256	400 x 256	192 x 288	192 x 256	192 x 256
In-plane Resolution (mm^2)	0.8 x 0.8	0.25 x 0.25	0.125 x 0.125	0.135 x 0.135	0.125 x 0.125	0.125 x 0.125
Slice thickness (mm)	0.8	0.6	0.6	0.6	0.6	0.6
Distance b/t slices (mm)	0.8	0.6	0.6	0.6	1.2	0.6
Number of slice	96	8	10	16	16	16
Total scan time	10 min 40 sec	1 m 29 sec	29 min 52 sec	33 min 36 sec	29 min 52 sec	29 min 52 sec

[a] Fast low angle shot [140].

[b] Rapid acquisition with relaxation enhancement [141].

Construction of spine coil array

The design of the 12-element whole-spine coil array for marmosets was based on an early human spine coil that employs six pairs of loop-butterfly elements [160], but with an important difference: the loop elements were displaced from the butterfly elements by

one-half of a coil length, so that the loop and butterfly conductors were not overlapping (Figure 39). There are two reasons for this design: first, mutual inductance and electric field coupling among coil elements were minimized because the wire of the loop and the butterfly elements are orthogonal to each other. Second, while it is necessary to place the butterfly coil at the middle of the neck region to maximize the sensitivity of the cervical spinal cord, the shifted-pair design avoided placing a loop coil element at the middle of the neck region where the coil axis would be in a direction close to that of B_0. Furthermore, compared with Guclu *et al.*'s design [160], the MRI signal from each coil was acquired independently without the use of quadrature combiners. The coils were formed using AWG 16 wire instead of printed circuit boards, and the coils were assembled on an anatomically conforming curved former that follows the natural shape of a large marmoset. The matching network of the loop and butterfly coils are shown in Figure 40.

3D-printed PLA coil clips were used to mount the coils by fusing the clips onto the coil former with tetrahydrofuran solvent. The approximately 0.2 mm tolerance of the coil clips allowed fine adjustment for the optimization of geometric decoupling. PLA cement was made by dissolving recycled PLA material into tetrahydrofuran, and the cement was applied on the coil clips to permanently secure the coils after the geometric decoupling was optimized as seen in Figure 41.

Small floating cable traps (outer diameter/length = 8 mm/12 mm) [143] were installed on coaxial cables (Temp-Flex 50CX-41, Molex, Lisle, IL, USA) close to the matching network of each coil, and large floating cable traps (outer diameter/length = 22.9 mm/35

mm) were installed at every quarter-wave length. Multi-pin RF connectors (ODU GmbH & Co. KG, Mühldorf a. Inn, Bavaria, Germany) were used to connect the coil array to our in-house developed preamplifier modules. The cable lengths and phase shifters of each receiving coils are adjusted to transform the low input impedance to shunt reactance for preamplifier decoupling.

The total length of a marmoset spinal cord from cervical, thoracic, lumbar to sacral parts is typically 98 [165] to 150 [166] mm. To cover the entire region, a 12-element coil array was built. Before the coil array was deformed to follow the natural shape of the marmoset spine, as shown in Figure 39, the dimension of the coil array was 179 mm (L) x 30 mm (W). The length of the coil array where the loop coils and the butterfly coils overlap was 154 mm. The first loop coil was placed under the cerebellum, and the last loop coil was placed under the L4 segment of spine.

To provide a comparison, a 4-element linear loop coil array (diameter = 21 mm and length = 65 mm) was used. A full-scale 12-element linear loop coil array consisting of the same size of loop coils would be approximately of the same length of the proposed 12-element coil array with shifted loop-butterfly elements.

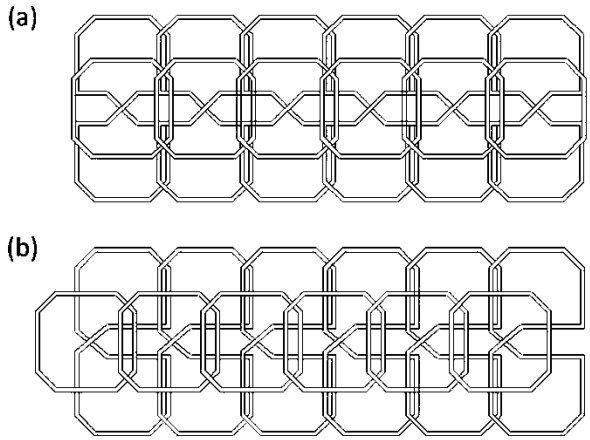

Figure 39. Comparison of traditional and proposed coil arrangements. (a) Human spinal cord coil array featuring loop and butterfly elements with a traditional quadrature arrangement.[2] (b) Proposed 12-channel design with shifted pairs of loop and butterfly coil elements that minimized inductive coupling between the elements. The center of the first loop coil on the left is placed at the beginning of the cervical segment of the spinal cord, and the center of the last loop coil on the right is placed at the end of the lumbar segment. Dimensions of the coil array: 179 mm (L) x 30 mm (W).

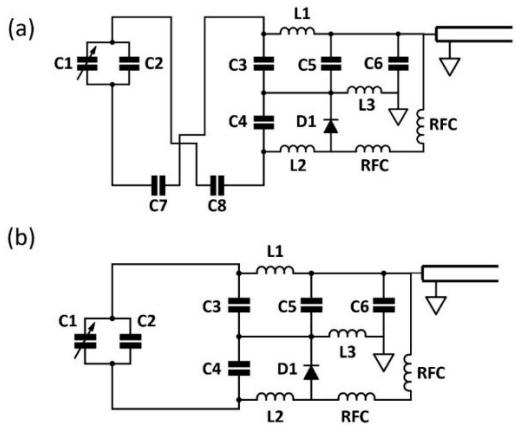

Figure 40. Circuit diagrams of loop and butterfly coil used on the 12-channel marmoset spine coil array. Circuit diagram schematics of (a) butterfly and (b) loop coil elements. A variable capacitor (C1) is used for tuning, and a fixed inductor (L1) is used for noise matching. The inductors L1 (for matching), L2 (for active detune) and L3 (for phase shifter) are arranged in a way that maximizes the spatial distance between them. Two RF chokes (RFC) provide 50 dB of isolation between the PIN diode signal line and the RF line.

Bench measurements

A custom-made testing rig and a network analyzer (Agilent Technology, Santa Clara, CA, USA) were used for bench measurements. Coils were connected to in-house developed preamplifier modules via ODU (ODU GmbH & Co. KG, Mühldorf a. Inn, Bavaria, Germany) multi-pin connectors. Preamplifiers were connected to the custom rig which provides 10 V power to the preamplifiers, 50 Ω terminations for the preamplifier outputs, and PIN diode signals to enable/disable individual coils. Tuning and noise matching were performed when the coil array was loaded with the proposed head-and-brain phantom, and an individual coil was connected to the network analyzer while other coils were active detuned through the custom testing rig. The performance of the active detune trap was measured using the difference of S_{11} measurements before and after the PIN diode on the coil was forward (+5 V) biased.

A geometrically decoupled (<-75 dB) double-loop probe was used for S_{21} measurements. The ratio of unloaded to loaded quality factor (Q_u-to-Q_l ratio) of a resonated loop coil without matching network was measured using the double-loop probe. A 4-mm spacer was used to separate the coil from a bag of normal saline as the loaded condition. The Q_u-to-Q_l ratio of a resonated butterfly coil was also measured in the same method. The Q ratio of each coil was measured again when the coil array was fully populated and non-testing coils were actively detuned. The performance of the preamplifier decoupling was measured by the difference of S_{21} measurements before and after each coil was power matched (connected to a 50 Ω termination) and noise matched (low-input impedance preamplifier termination) [144].

Phantom and in vivo imaging

The coil performance was evaluated on a phantom and a marmoset *in vivo* using 3D fast low angle shot (FLASH) and spin-echo sequences, respectively. The imaging parameters are shown in Table 6.

When the coil array was loaded with the proposed phantom, noise-only images n_i and n_j of the *i*-th and *j*-th coils were acquired without RF excitation [110] to calculate the noise covariance matrix

$$\Psi_{i,j} = \langle n_i \cdot n_j^* \rangle.$$

The noise correlation matrix between coils was computed using

$$\Psi_{ij}^{corr} = \Psi_{ij}\left(\Psi_{ii}\Psi_{jj}\right)^{-1/2}.$$

SNR and signal homogeneity of the high-resolution spinal cord images were evaluated for the performance of the spine coil array.

Results and discussions

The 12-channel coil array connected to two preamplifier modules is shown in Figure 41. The Q_u-to-Q_l ratios of individual loop and butterfly coils were 7.5 and 6.2 respectively. This demonstrated good sample-loss dominance.

All coils were tuned to 300.128 MHz and noise matched close to 50 Ω (S_{11} < -19 dB) when the array was loaded with two different anesthetized marmosets. In addition to geometric decoupling, low input impedance preamplifiers provided additional decoupling

of 23±2.3 dB. Unloaded to loaded Q ratios were measured with a decoupled double probe when the array was loaded with normal saline (from head to tail): 5.17, 3.28, 2.48, 2.13, 2.87, 2.60, 3.86, 2.46, 3.43, 4.04, 5.00 and 5.48. The reduced Q_u-to-Q_l ratios suggest inductive loss from adjacent copper and wire. Nonetheless, all receive coils present satisfactory sample-loss dominance.

The noise correlation matrix obtained from noise-only images is shown in Figure 42. The maximum noise correlation was 34%, the minimum noise correlation was 1.0%, and the average noise correlation was 14%. This demonstrated satisfactory isolation between each receive coil elements.

MRI images of the phantom are shown in Figure 43. The images received by individual images confirmed good coil-to-coil isolation. Compared to a previously built generic 4-channel loop array, the 12-element coil array presented an SNR gain of 5.3 fold at the cervical spinal cord area. Spinal cord images obtained *in vivo* are shown in Figure 44 and Figure 45. Notice the detailed delineation of spinal cords and nerve roots in sagittal and axial views. Analysis of the high-resolution *in vivo* spinal cord images obtained in both sagittal and axial views showed complete coverage of the spinal cord and SNR of 30 in spinal cord areas. Compared with the previous setup using the generic 4-channel loop array, the new conformal 12-element design reduced the setup time from 90 minutes to 15 minutes and enabled imaging experiments in time frames that were previously unattainable for high-resolution *in vivo* imaging.

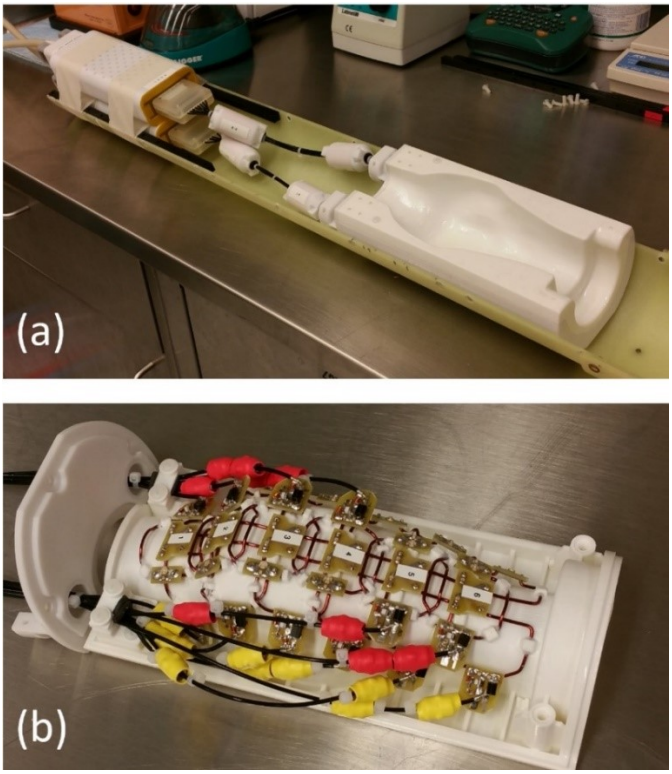

Figure 41. 12-channel marmoset spine coil array using shifted loop-butterfly pairs. (a) Picture of the anatomically conforming coil former showing the coaxial cables connecting the spinal cord coil array to the preamplifiers. The former was designed to fit marmosets of all sizes while keeping the spine straight. Additional padding may be used to accommodate smaller marmosets. (b) Open view of the coil former revealing the layout of the coil elements, which are placed to follow the natural shape of the marmoset back. Floating cable traps are shown in red and yellow heat-shrink insulation tubing.

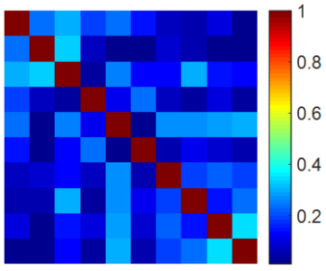

Figure 42. Noise correlation matrix of the 12-channel spine coil array. Maximum noise correlation coefficient is 34%, the minimum noise correlation coefficient is 1.0%, and the average noise correlation coefficient is 14%.

(a)

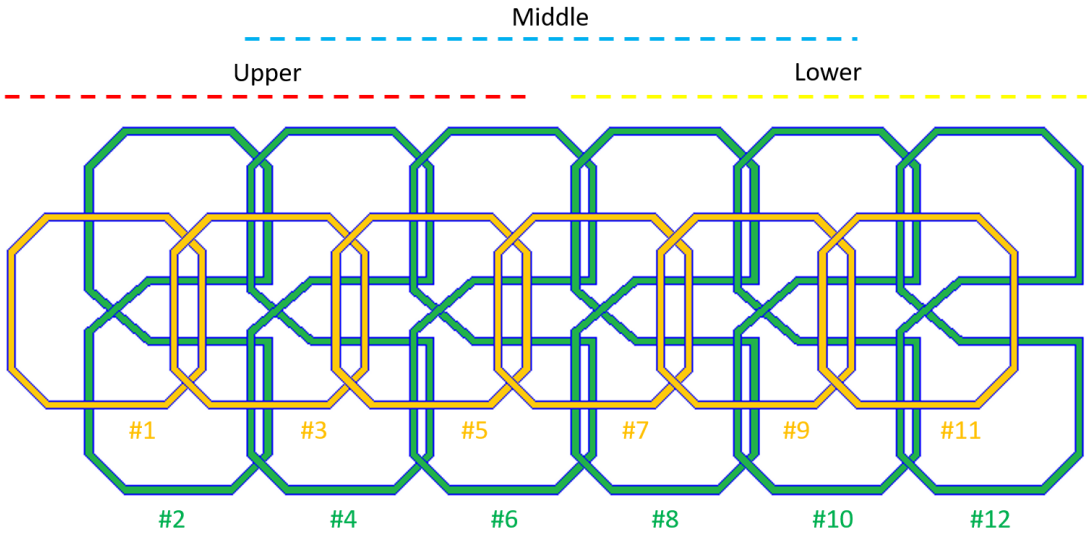

Figure 43. MR images of the body-and-spine phantom acquired by the 12-channel spine coil array. Because of a limitation of the gradient diameter spherical volume (DSV), the upper, middle and lower segments (which focuses on cervical, thoracic and lumbar areas) of the spinal cord have to be imaged separately. (a) The spatial arrangement of the 6 loop coils (orange) and the 6 butterfly coils (green) is illustrated. Coil #1 is placed under the marmoset head, and Coil #12 is placed at the end of the lumbar part of the spinal cord. Although all the receiving coils are enabled during receive, only signals from part of the coil array are combined to slightly improve the SNR. Coil #1 to #5 (red) are used for the image reconstruction of the upper part of the spinal cord, Coil #4 to #9 (blue) are used for the middle part of the spinal cord, and Coil #8 to #12 (yellow) are for the lower part of the spinal cord.

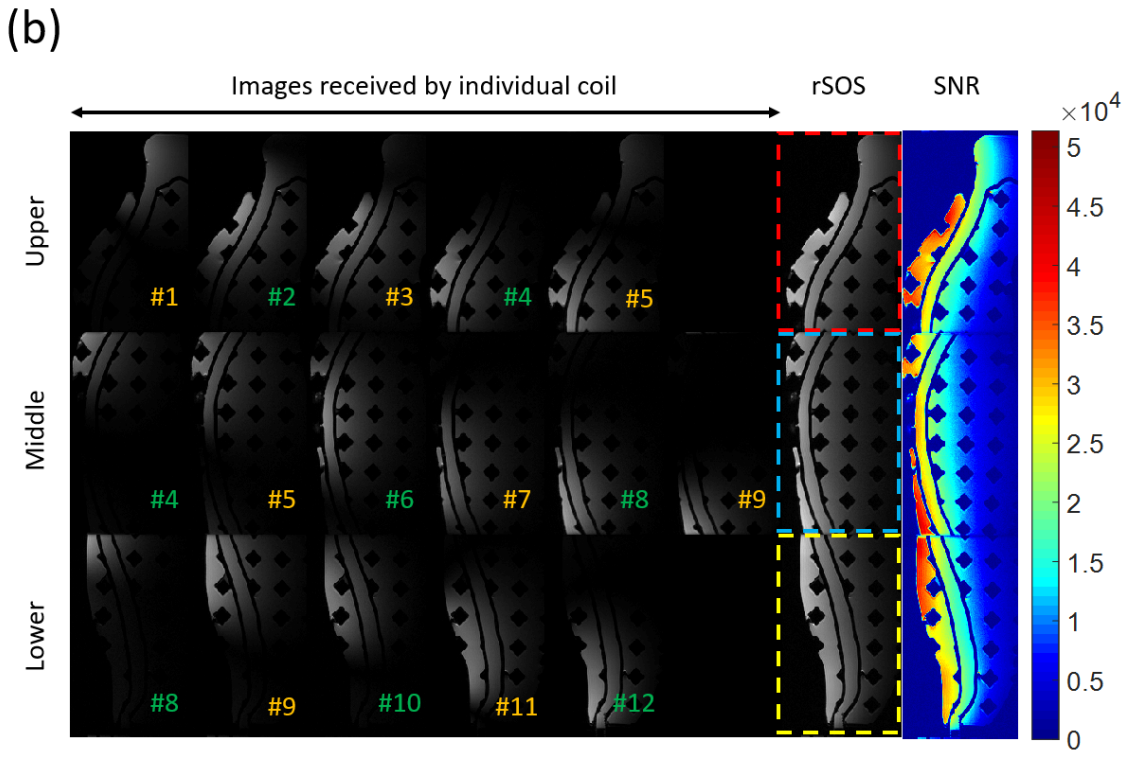

Figure 43. Continued. (b) The images received by individual coils for the upper, middle and lower part of the phantom is shown on the left side. The combined image of each segment is reconstructed through the square root of the sum-of-square images (rSOS). The SNR of each segment is shown on the right side.

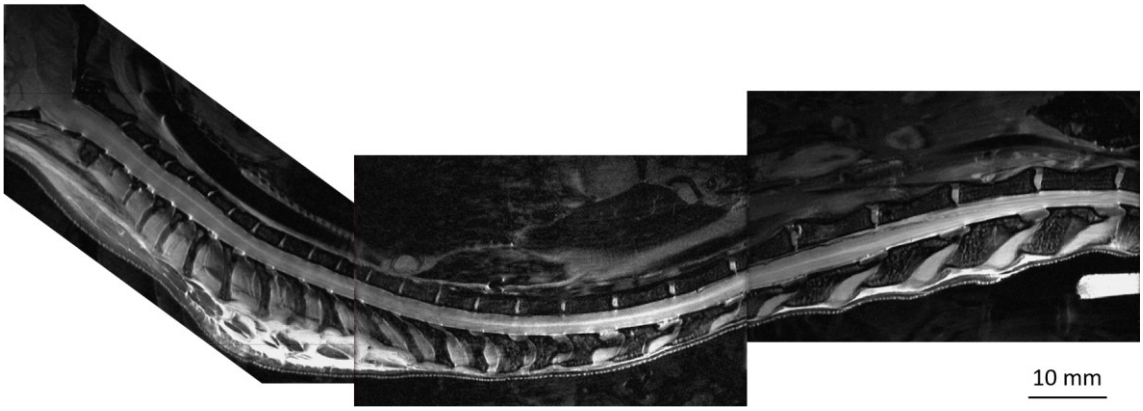

Figure 44. *In vivo* MRI of one entire marmoset spinal cord. Three segments of one marmoset spinal cord are imaged one-at-a-time due to the limitation of the diameter spherical volume. The montage of these three segments presents the overall spinal profile when the marmoset is placed inside of the proposed 12-channel spinal coil array. Fast spin echo sequence (RARE factor = 2, NEX = 4, TR/TE = 3500/15 ms, in-plane resolution: 125 µm x 125 µm, slice thickness = 0.6 mm, slice number = 10) is used to acquire sagittal images which cover the cervical, thoracic and lumbar segments of the marmoset spinal cord *in vivo*. The gray matter is shown in white and white matter is shown in gray inside of the spinal cord. The thin white line inside of the spinal cord serves as the indication that the spine is generally self-aligned when the marmoset is placed inside of the proposed 12-channel coil array.

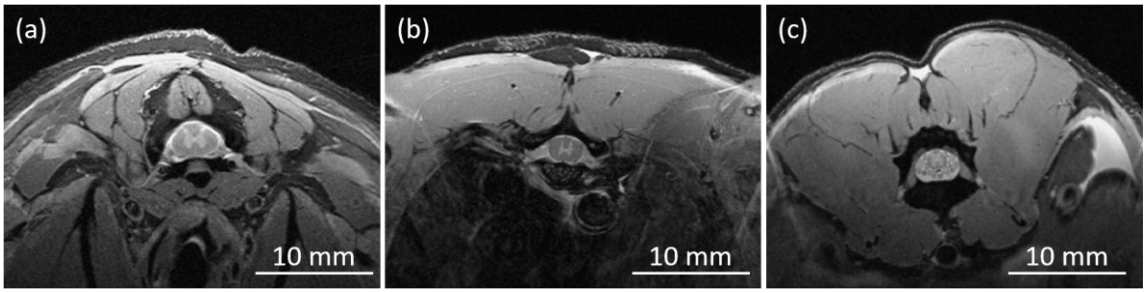

Figure 45. Axial view of *in vivo* MRI of marmoset spinal cords on cervical, thoracic and lumbar segments. Imaging parameters: fast spin echo sequence, RARE factor = 2, NEX = 4, TR/TE = 3500/15 msec, slice thickness = 0.6 mm, slice number = 16. The in-plane resolution of cervical segment (a) is 135 µm x 135 µm. Because of the smaller size of a spinal cord in the thoracic segment and the finer feature of longitudinal nerve roots in the lumbar segment, the in-plane resolution is increased to 125 µm x 125 µm in images of thoracic (b) and lumbar (c) segments.

Conclusion

The unloaded to loaded Q ratios showed good overall sample-noise dominance over the entire length of the array. The reduced Q ratio of the coil elements located around the thoracic segment of the spinal cord suggests copper-induced losses from neighboring coils. This is almost unavoidable considering the size of the coils. The phantom imaging showed satisfactory channel-to-channel isolation and consistent sensitivity throughout the entire spinal cord, and the improved SNR allowed a substantial reduction in scan-time. In additional to respiratory/cardiac gating and anesthesia, motion artifacts were also greatly reduced with use of the anatomically conforming coil former. Warming is absolutely necessary to prevent hypothermia when anesthesia is used [167, 168]. We found that, with the help of the conforming coil former and a heated water pad, keeping the body temperature stable correlated with more stable heart rate, SpO_2 and CO_2 levels, suggesting improved animal comfort and safety. The 12-channel coil array will substantially improve ongoing and future studies of marmoset models of multiple-sclerosis, spinal cord tumors and spinal cord injuries.

CHAPTER VII

SUMMARY OF DESIGN TECHNIQUES FOR SMALL ANIMAL COIL ARRAYS

Streamlined design strategy and streamlined experimental setup

Four small-animal coil arrays were developed using streamlined strategies to create high performance coil arrays with reduced iterations. Experimental setups for mouse and marmoset scans were also streamlined by design. Here is the summary:

Main concept

Space limitations, necessary equipment, routing of cables and tubes and workflow of experimental setup were all planned as one system at the beginning of the design phase. Computer-aided design (CAD) software, 3D printing and smaller scale prototypes were used to validate clearance, coil performance and experimental setup prior to the full-scale hardware implementation.

Enabling tools

Various tools were developed to streamline the design of small coil arrays. Here is the summary of tools developed in this dissertation:

(1) Matching networks that allow independent development of tuning, noise matching, active detune traps and phase shifters. Figure 15, Figure 30 and Figure 40 present three different matching networks, all of which allow optimization of each functional block while exerting minimal effects on others. This feature allows streamlined development of coil arrays with less time spent on iterations. Note that

each variable capacitor with small tuning range is paired with a fixed-value capacitor to allow adjustability and stability.

(2) Preamplifier modules: for coil arrays without integrated preamplifiers, modular preamplifiers were used as shown in Figure 46. The multi-pin connectors of the input and the output ports of the preamplifier module and the non-magnetic latching mechanism (Figure 47) were used to streamline the experimental setup.

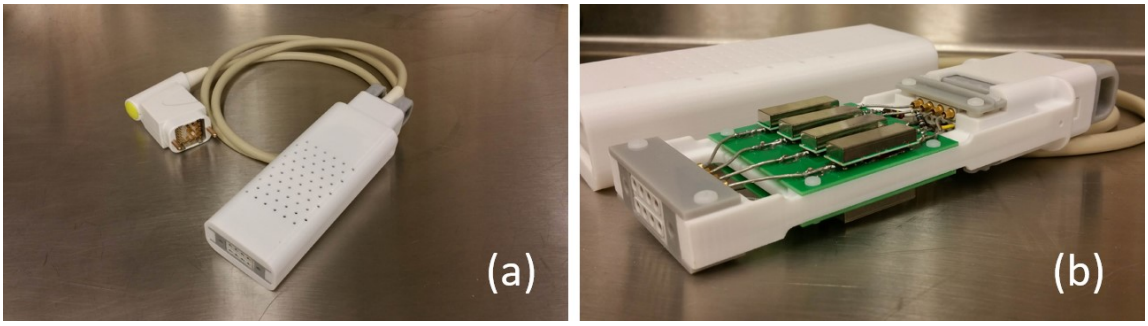

Figure 46. Modular preamplifier with multi-pin input and output ports. (a) Overview of the modular preamplifier. The enclosure has ventilation holes to reduce potential accumulation of heat during long scans. (b) Internal view of the preamplifier module. Semi-rigid cables were used to connect the ODU connectors to the input/output of the shielded preamplifiers. Cable traps were installed on the shield of the cables to suppress common mode. Bias-tees and lowpass filters were used to mix PIN diode control signals to the input of the preamplifiers.

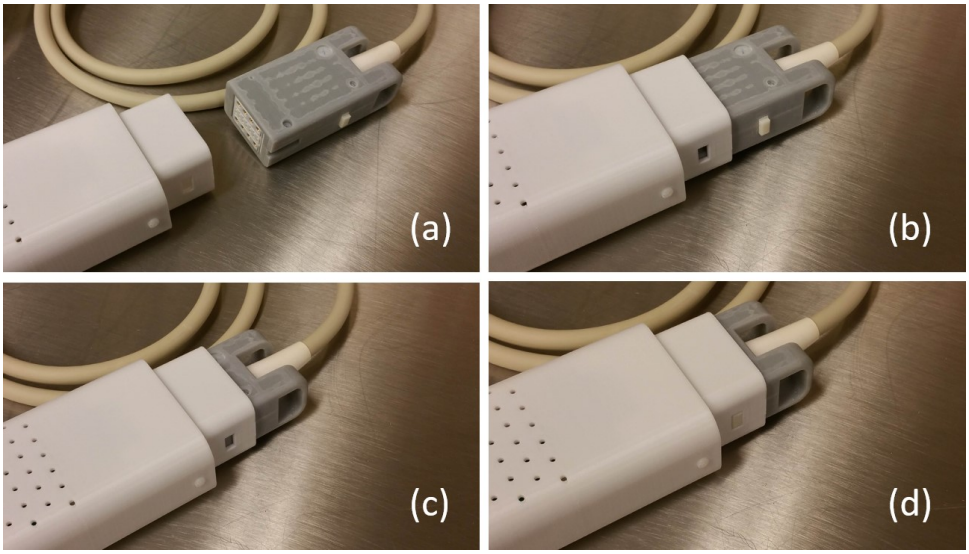

Figure 47. Latching mechanism of modular preamplifier. This non-magnetic latching mechanism connects the system cable to the preamplifier module to streamline the experiment setup. This allows the preamplifiers to be connected to the receiver without feeding the system cable through the narrow bore of the scanner.

(3) Coil shaping tools: Coils made out of wire have less copper related loss than coils made out of microstrips. Coil shaping tools enabled the routine use of wire on the development of coil arrays in a consistent way. Figure 48 and Figure 49 show how wired loop and butterfly coil arrays are built using a “winding tool” and a “bending tool” to form the shapes and the bridges of a coil.

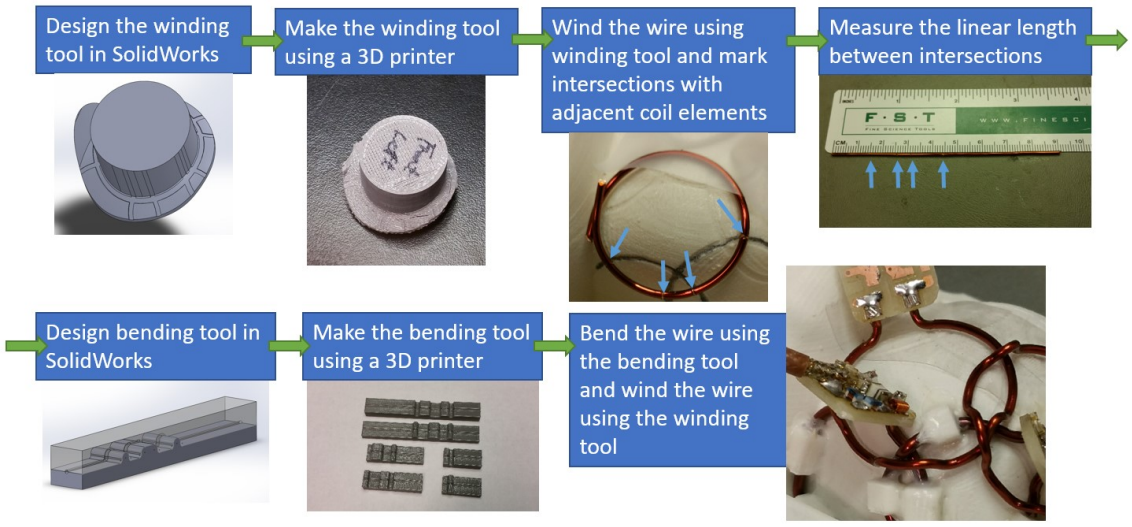

Figure 48. Flow chart of constructing a loop coil array using coil shaping tools.

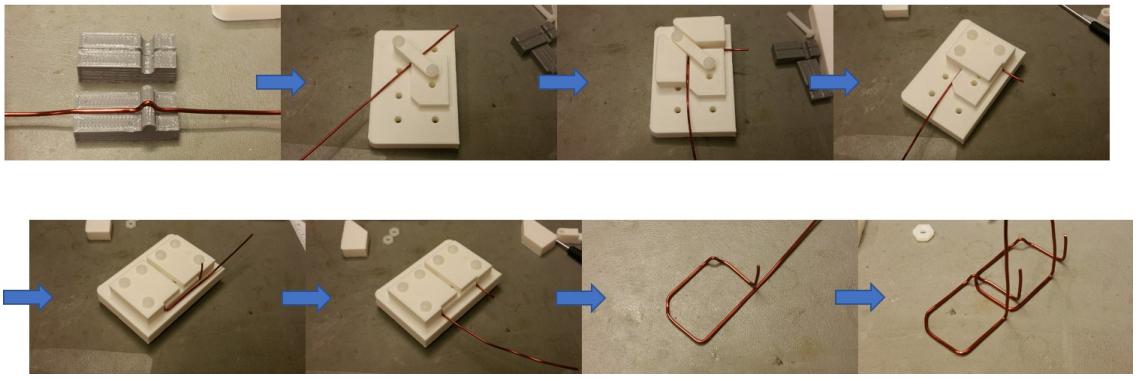

Figure 49. Example of constructing a butterfly coil array using coil shaping tools. One side of the butterfly coils are demonstrated here.

(4) 3D printing, coil clips and PLA cement: 3D printing is very useful for making parts of a complicated shape without the limitations of traditional manufacturing methods. It also makes engraving fiducial marks of coil arrays on the coil former easier. When the coil former is printed by PLA material, 3D printed coil clips and

PLA cement can be used to mount coils on the former with high accuracy and stability as shown in Figure 50.

Figure 50. Using coil clips and PLA cement to help assemble coil arrays on a coil former of irregular shape in a space-restricted environment. (a) 3D printed coil clips made of PLA material. (b) PLA cement made by dissolving recycled PLA material in tetrahydrofuran solvent. (c) A coil mounted on the coil former by fusing coil clips with tetrahydrofuran. The gaps between the coil and the coil clips were filled with PLA cement. As is demonstrated in (c), all components except the phase shifter were able to be soldered on the coil before the coil was mounted on the coil former, because of the streamlined circuit design. This negated the need to solder small components in confined spaces.

(5) Customized phantoms: Multi-compartment phantoms can help measure the SNR of specific areas of interests without requiring the use of real animals. Figure 28 and Figure 51 show a head-and-brain phantom and a body-and-spine phantom, respectively. The regular lattice pattern inside of the phantom serves as the support of the inner compartment as well as the guide for slice planning. The SNR inside of volume of interest, i.e. the brain or CNS, can be calculated easily using phantom images without the use of marmosets.

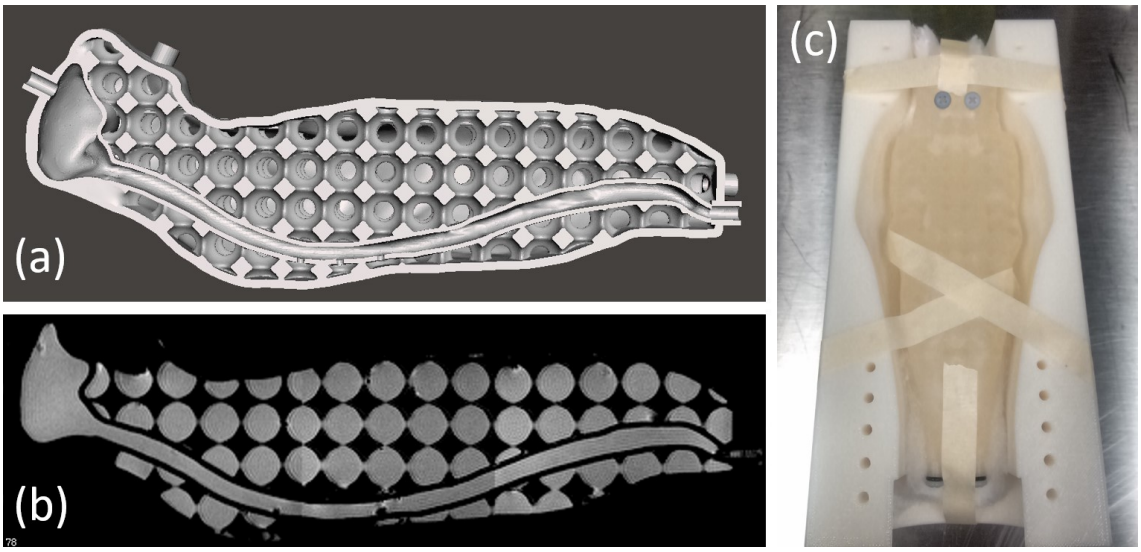

Figure 51. Marmoset body-and-spine phantom. (a) 3D model of the phantom consisted of the body shell, CNS shell and the regular lattice pattern which supports the CNS shell. (b) MRI of the phantom in sagittal view. The regular lattice pattern serves as the guide for imaging. The slice orientation is aligned with the phantom when the size of the circular discs are the same. (c) The 3D printed phantom inside of a prototype cradle.

(6) Simulated scanner interface for coil tuning, noise matching, active detune and preamplifier decoupling: A piece of custom hardware was built to simulate the scanner interface of the Bruker system as shown in Figure 52. The interface simulated the power supply to the preamplifiers and 50 Ω terminations at the output of the preamplifiers. Each 50 Ω termination consisted of 4 pairs of one large-value capacitor (as DC block) and one 200 Ω resistor (as a distributed load). RF outputs of the preamplifiers had shared ground and isolated 50 Ω loads. The power source was isolated from the RF outputs of the preamplifiers using distributed RF chokes (next to each MCX connector and the power input on the board) to prevent hidden RF paths. Two controller boards were used to control the

PIN diode signals. Coils connected to the preamplifier modules could be detuned individually using pin headers on one of the controller boards.

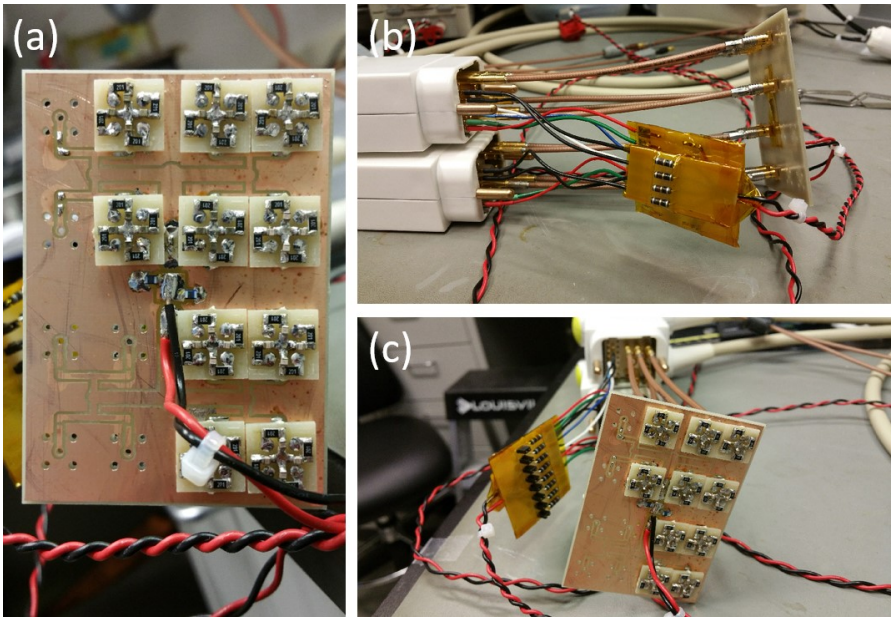

Figure 52. Simulated scanner interface for Bruker system. (a) The Interface board which supports power to the preamplifiers and provides 50 Ω terminations. (b and c) System connectors are connected to the interface board and the PIN diode controller board.

(7) Molded foam pads: Foam padding is important for animal MRI coils to provide for the comfort and thermal insulation of animals. Moldable foam enables custom-shaped foam padding to be used on any kinds of application. Figure 29 shows the application of molded foam padding used inside of a marmoset helmet for awake brain imaging.

Decoupling between receiving elements

Decoupling between receiving elements is crucial for MRI. Here is the summary of designs and techniques developed/used in this dissertation:

(1) Special coil array: some special coil elements, such as DPP and DPPX coils are naturally decoupled from neighboring elements. Figure 4 shows the proposed DPPX coil.

(2) Loop/butterfly coil arrays: Loop and butterfly coils are commonly used in the construction of coil arrays. These coils need to overlap by a critical amount of distance to reduce the magnetic field between two adjacent coils and thus achieve geometric decoupling. Two streamlined strategies for geometric decoupling of these two types of coil arrays were used:

    a. 1D array or 2D array with regular mesh: small scale prototype and 3D printing were used to streamline the process of geometric decoupling as described in 0. Once the size and amount of overlap between a pair of adjacent coils was determined with the help of 3D printed coil formers, the rest of the coils were populated using coil bending tools and coil winding tools as shown in Figure 48 and Figure 49. Figure 14 shows an example of the geometric decoupling of a 6-channel loop coil array using this strategy. Figure 53 shows an example of the geometric decoupling of a 6-channel butterfly coil array.

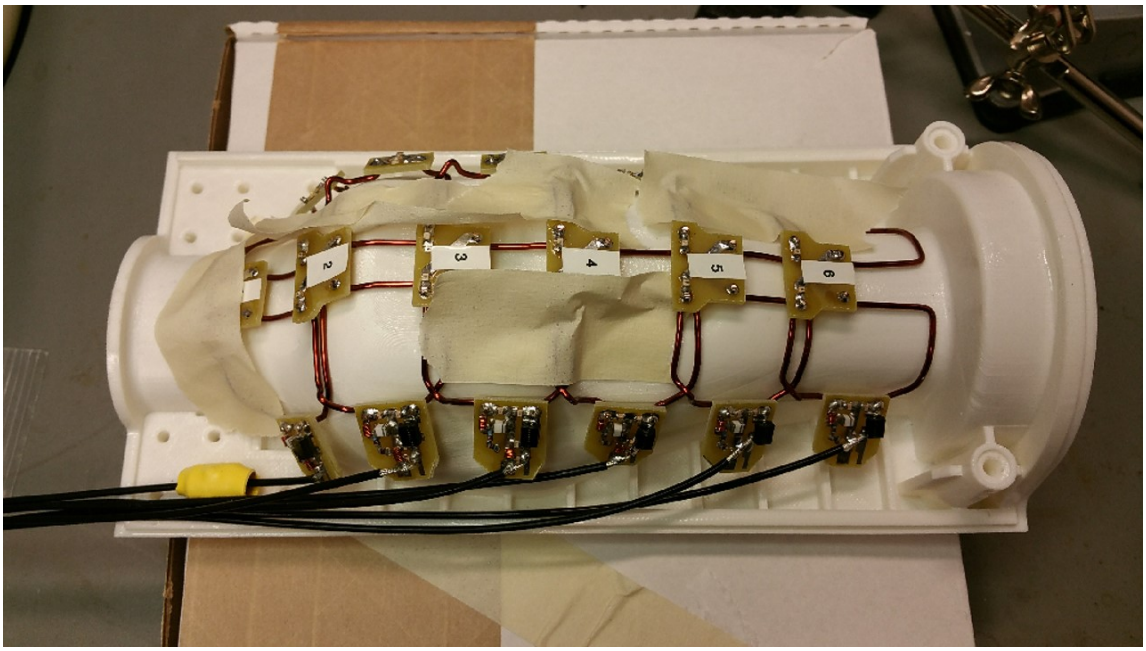

Figure 53. Geometric decoupling of a butterfly coil array for imaging marmoset spinal cords. The photo was taken before the coils were permanently mounted on the coil former.

b. Soccer ball: For building a coil array using soccer ball arrangement, the "outside-in," "local-bend" and "coil clips and PLA cement" approaches were proposed to streamline the development: "Outside-in approach", as shown in Figure 54, means to start building the coil elements from the outer ones which are close to the edge of the coil former, and continue building by spiraling-in to the center of the soccer ball pattern. This strategy reduces the number of neighboring elements of each new coil being mounted. "Local-bend strategy," as shown in Figure 55, was used to optimize geometric decoupling between neighboring elements while exerting minimal effect on the global arrangement of the soccer ball pattern or on

the locations of other coils. In addition, right-left symmetry was preserved. Note that the optimization of geometric decoupling was done with the presence of un-resonated copper traces around the coil to be mounted to simulate the condition of the final coil construction. With “outside-in” and “local-bend” strategies, the iteration for geometric decoupling for soccer ball coil arrays was eliminated. “Coil clips and PLA cement” were used to help with mounting the coils and to optimize geometric decoupling accurately on a strong structure.

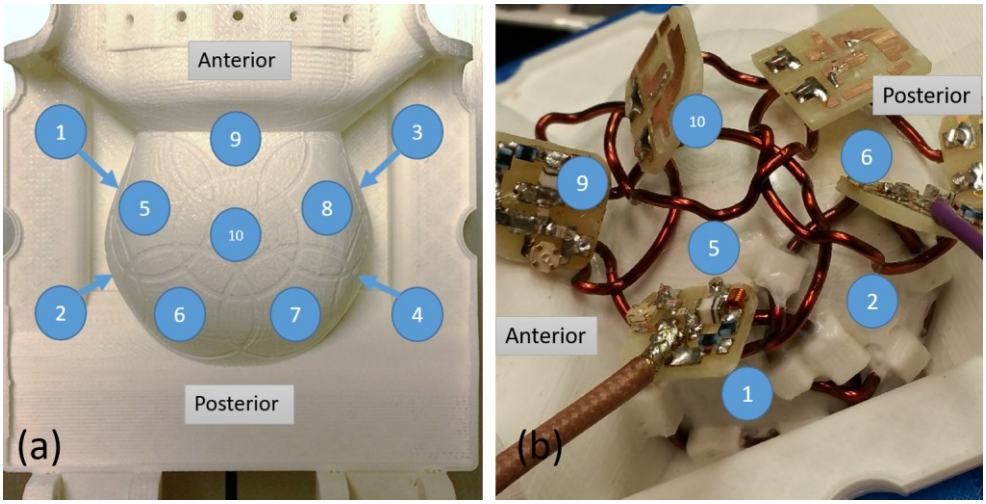

Figure 54. "Outside-in" strategy for streamlining the development of coil arrays with soccer ball arrangement. (a) Number 1 to 10 indicate the order of coil construction—from the outer elements toward the center of the soccer ball arrangement. (b) After Coil 1&2 have been installed, determining the geometric decoupling between Coil 5 and Coil 1/2 needs the presence of the other surrounding Coil 6, 9 and 10 to simulate the environment of the final coil array. With this streamlined strategy, the iteration for geometric decoupling is eliminated.

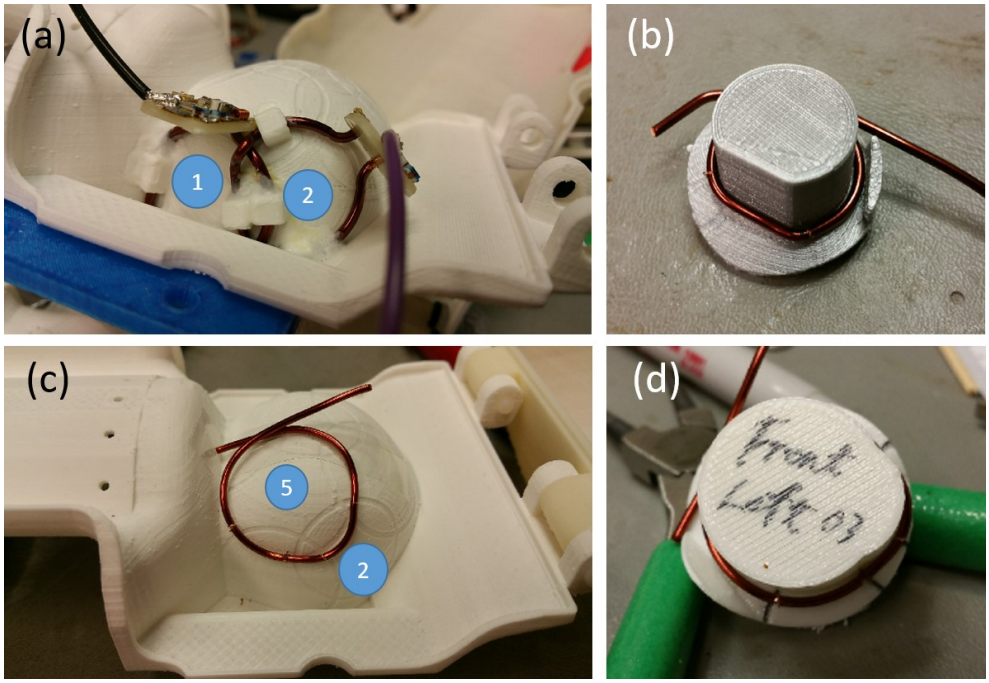

Figure 55. "Local-bend" strategy for streamlining the geometric decoupling between loop elements. Local-bends are used to decrease the overlap (a and b) and increase the overlap (c and d) for the optimization of geometric decoupling. This strategy prevents the iteration for geometric decoupling and the propagation of geometrical changes to other coils.

Adaptation for size variation of research subjects

The size variation of animals makes optimization of tuning and matching of MRI coils difficult. Here is the summary of techniques developed in this dissertation:

(1) Adjustable mechanical design: Mechanical designs allowed the adjustment of coil positions to accommodate for the size variation of research subjects. Figure 5 shows the scissor-jack-like mechanism that moves the coil arrays to adapt for different sizes of mice while keeping the arrays parallel to the z-axis. This kind of

design requires coil elements that naturally do not couple to each other or high-performance preamplifier decoupling.

(2) Image-driven CAD design of models with flexible padding: Image-driven 3D models were used to design coil formers. MRI-derived 3D models mimicked the natural shape of the animal of interest, helped stabilize the position of the animal and streamlined experimental setup. Usually a larger animal was used to generate the 3D model. Therefore, to accommodate for smaller animals, and to increase animal comfort and thermal insulation, foam padding was used. Figure 29 shows the helmet with molded-in foam padding for awake marmoset brain imaging. Figure 32 and Figure 56 show the 10-channel marmoset head coil array built on a coil former which was derived from MRI of a large marmoset head. Figure 41 shows the 12-channel marmoset spine coil array built on a coil former which was derived from MRI of a large marmoset body.

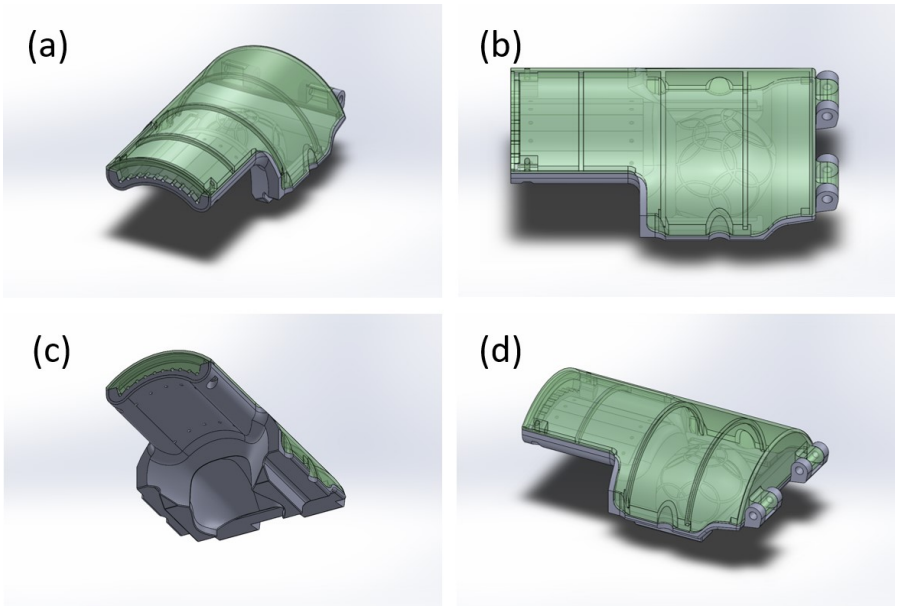

Figure 56. CAD design of a 10-channel marmoset head coil array.

Streamlining experimental setup

Streamlining experimental setup can reduce the burden of researchers, reduce experiment errors and promote animal safety. Here is the summary of techniques developed/used in this dissertation:

(1) Integrated connections, tubes, multi-pin connectors and design of coil shapes: Various designs were used to streamline experimental setups. Figure 18 shows a mouse bed design for loading a mouse efficiently. The integrated anesthesia and heating tubes streamline the experimental setup. Figure 20 shows the twist-n-lock mechanism of the mouse for inserting a mouse into the coil array easily. Figure 21 shows the design to quickly select the anatomy of interest to image different parts of a mouse. Multi-pin connectors help to connect multi-channel coil arrays into the

preamplifiers and receivers quickly as shown in Figure 57(b). Experimental setup was also streamlined by designing the coil shape to fit on the animal cradle and to house the animal body as shown in Figure 57(a).

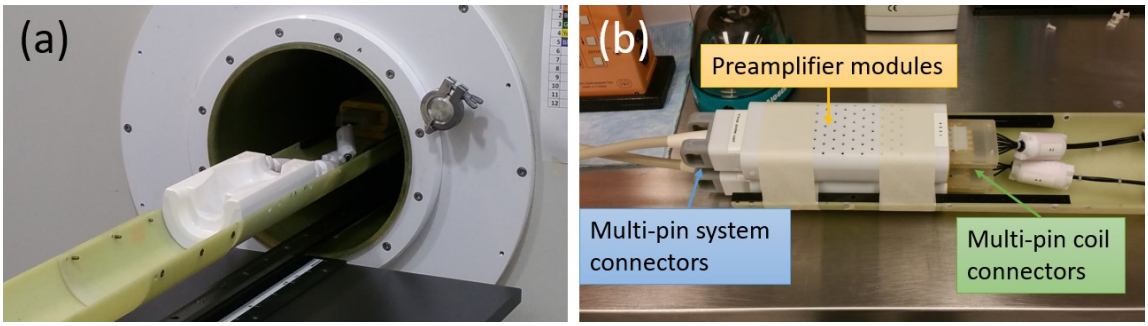

Figure 57. Design of coil shape and use of multi-pin connectors to streamline experimental setup. (a) The 12-channel spine coil array follows the shape of the half-cylindrical coil holder. (b) Multi-pin connectors streamline the connections of the coils and preamplifiers.

(2) Ease of cleaning: Disposable liners and 3D printed mouse beds helped to clean coils after animal experiments as shown in Figure 19. Non-magnetic paints, such as epoxy based paint (EPO-TEK 301, Epoxy Technology Inc., Billerica, MA, USA), rubber based paint (Performix F-717, Plesti Dip International, Blaine, MN, USA) and acrylic based paint (clear acrylic: gloss/matt, Aervoe Industries, Inc., Gardnerville, NV, USA) were used to seal/waterproof porous 3D printed parts for easier cleaning.

CHAPTER VIII

CONCLUSIONS AND FUTURE WORK

In conclusion, this doctoral work has examined the need to streamline the design and construction and increase the usability of array coils for small animal MRI. The performance of the various coil arrays described in this dissertation with respect to achieving this goal, in comparison to previous reports or commercial products, is summarized in Table 7.

Performance of coil arrays

Performance of coil arrays, in terms of streamlined design strategy and efficiency of streamlined experimental setups, are summarized in Table 7.

As the last coil array being developed in this work, the 12-channel coil array for *in vivo* marmoset spine imaging has the highest performance in terms of SNR, streamlined development and streamlined experimental setup. Serving as thermal insulation, the installation of carton pads was part of the coil design, therefore the coil array scored "better" in "streamlined experimental setup: temperature control." The coil former was designed to accommodate for the external tubing of anesthesia and heating, however, these tubes were not integrated into the coil. Therefore, in the category of "streamlined experimental setup: anesthesia and heating tubing," it only scored "acceptable/no improvements."

The 10-channel coil array for awake marmoset brain imaging performed well overall, especially for the excellent decoupling between array elements which enabled parallel imaging in both x- and z-directions. The streamlined design strategy successfully reduced iterations through the coil development. The SNR of the 10-channel coil array also showed 17-27% of SNR increase compared to the previous 8-channel design [137]. Previously, water-pad heating was used and no improvement was done on this part, therefore, "streamlined experiment: temperature control" was only "acceptable/no improvements." Because the 10-channel coil array was designed for awake brain imaging, anesthesia was not used and marked as "N/A."

The general-purpose 6-channel mouse loop coil array demonstrated high image quality, streamlined coil design and streamlined experimental setup through the use of innovative mouse handling design and integrated tubing for anesthesia and heating. With these improvements, the 6-channel coil array scored "better" in many of these categories.

However, both the 6-channel mouse loop coil array and the 10-channel mouse DPPX coil array scored "lower" in the category of "streamlined experimental setup: coil connection" because multi-pin connectors were not used. Instead, common BNC connectors were used. That being said, the connectors could be easily replaced with ODU multi-pin connectors, and the score of this category will be "acceptable/no difference" compared to industry standard. The 12-channel coil array for *in vivo* marmoset spine imaging and the 10-channel coil array for awake marmoset brain imaging both scored "better" in this category because both the input and the output of the preamplifier module used multi-pin connectors.

Commercial products do not use multi-pin connectors at the output of the preamplifier module. This design negated the need to feed the output cable of the preamplifier module through the narrow bore and streamlined the imaging setup.

Commercial MRI coils use MR-compatible paint to make coil-cleaning easier. Both the 10-channel marmoset head coil array and the 12-channel marmoset spine coil array used similar design, therefore they score “acceptable/no difference” in the “ease of cleaning” category. The 6-channel mouse loop coil array and the 10-channel mouse DPPX coil array both scored “better” in this category because both used disposable liners and the later even used disposable 3D-printed mouse bed which minimizes the need of cleaning.

Although 10-channel mouse DPPX coil array did not meet our expectation in terms of the SNR at the center of the subject, this proprietary design had a lot of unique properties. The receiving coil array was able to decouple from the transmitting coil without the need of active detune traps which greatly streamlined the design of the coil and ultimately solved the problem of fitting components and cable routing into a confined space. The geometry of the coil element also straightforwardly prevented the coupling of neighboring elements. The scissor-jack mechanism allowed unique size adjustment in a confined space. It is possible to increase the sensitivity of the coil array if the distance between the signal line and the crisscrossed return paths is increased in the future.

Table 7. Comparison of performance of coil arrays: SNR, streamlined coil designs and streamlined experimental setups.

		Streamlined coil design		Streamlined experimental setup				
Coil array	**SNR**	***circuit network***	***geometric decoupling***	***Animal handling***	***Coil connection***	***Anesthesia and heating tubing***	***Temperature control***	***Ease of cleaning***
12-ch marmoset spine coil array	◊ (5.3X SNR over 4-ch array)	◊	○ (-15dB to adjacent Rx coil)	◊ (reduced 75 - 225 min prep time)	◊ (both input/output of preamplifier are modular)	○	◊	○
10-ch marmoset head coil array	◊ (17 - 27% increase over 8-ch array)	◊	○ (-15dB to adjacent Rx coil)	◊ (reduced 20 min prep time)	◊ (both input/output of preamplifier are modular)	N/A (no anesthesia used in awake imaging)	○	○
6-ch mouse loop coil array	◊ (1.21 - 4.08X over quad volume coil)	◊	○ (-15 dB to adjacent Rx coil)	◊ (reduced 20 min prep time)	● (individual BNC connectors)	◊ (integrated)	○	◊
10-ch mouse DPPX coil array	● (0.42 - 4.57X over Tx volume coil)	◊	◊ (-19 ~ -54dB to Tx coil)	○	● (individual BNC connectors)	○	○	◊

◊: better ○: acceptable/no difference ●: lower

Future work

As the development of electronic components slows down, researchers are looking for new materials to further improve SNR of MRI. High dielectric materials such as $BaTiO_3$, and special geometric arrangement of such materials, can manipulate the distribution of RF fields in three-dimensional space. One can use this feature to either reduce coil-to-coil coupling or to focus RF field into a region of interest. New materials can also be used to manufacture thin, yet strong, mechanical parts to reduce the distance between receiving coils and the research subject, leading to higher SNR. Cryo-cooled coils and preamplifiers are also candidates for increasing SNR.

Most pre-clinical MRI scanners have very small bore size, and the lack of space makes advanced pre-clinical imaging difficult. For example, in addition to the transmitting and receiving coils, fMRI of awake marmoset imaging also requires body-restraint accessories, audio/visual/tactile stimulation devices, and devices that monitor the safety of the marmoset. Another example is arterial spin labeling (ASL) which requires another set of spin-labeling coil(s) to be added on top of the imaging coils. In this doctoral dissertation, most of the challenges were solved by strategic planning and integration of various devices. Perhaps, a thinner and shorter transmitting coil which provides equal or larger homogenous region, is a more general solution. For marmoset brain imaging, the extra room provided by thinner transmitting coil can be used to image the marmoset in a more comfortable position by lowering the body of the marmoset. This would also expose the posterior part of the marmoset head, and more receiving coil elements could be added to increase the SNR in the occipital lobe of the brain. Extra coil elements could also be

added around a marmoset head on top of the 12-channel spine coil array, thereby allowing the brain and the spinal cord to be imaged in a single session. This would drastically reduce the image preparation time for multiple sclerosis studies which require longitudinal studies of the entire central nervous system. Currently, brain and spinal cord imaging have to be done separately. In addition, the ACUC of NIH limits the frequency of anesthetizing a marmoset to once per week, and this poses a problem for disease models, such as multiple sclerosis, which progress rapidly in certain stages, yet the brain and the spinal cord have to be imaged in alternating weeks.

The complexity of hardware required for current pre-clinical studies is restrained by either space or system limitations. For example, when a dedicated arterial spin labeling coil is used with the proposed 10-channel receiving head coil array, all four system sockets provided by a Bruker MRI scanner are used. We were able to fit one infrared camera with infrared light source to monitor the marmoset's safety, but we ran out of space for our visual stimulation device. We also ran out of space and system sockets for additional arterial spin labeling coils.

Therefore, custom-made accessories are also needed for future pre-clinical MRI studies. For example, one can integrate a miniature visual stimulation display with infrared camera to save space and streamline the setup of animal imaging. To reduce system complexity, the ultimate solution is to connect coils and devices either through optic fibers or wireless links to keep up with the pace of the increasing complexity of pre-clinical imaging. This

would also require the advancement of non-magnetic miniature optical transceivers and RF power amplifiers.

REFERENCES

[1] K. K. Frese and D. A. Tuveson, "Maximizing mouse cancer models," *Nat Rev Cancer,* vol. 7, pp. 645-58, Sep 2007.

[2] J. Gehrmann, P. E. Hammer, C. T. Maguire, H. Wakimoto, J. K. Triedman, and C. I. Berul, "Phenotypic screening for heart rate variability in the mouse," *Am J Physiol Heart Circ Physiol,* vol. 279, pp. H733-40, Aug 2000.

[3] B. D. Hoit, "New approaches to phenotypic analysis in adult mice," *J Mol Cell Cardiol,* vol. 33, pp. 27-35, Jan 2001.

[4] B. J. Janssen and J. F. Smits, "Autonomic control of blood pressure in mice: basic physiology and effects of genetic modification," *Am J Physiol Regul Integr Comp Physiol,* vol. 282, pp. R1545-64, Jun 2002.

[5] G. A. MacGowan, C. Du, D. B. Cowan, C. Stamm, F. X. McGowan, R. J. Solaro*, et al.*, "Ischemic dysfunction in transgenic mice expressing troponin I lacking protein kinase C phosphorylation sites," *Am J Physiol Heart Circ Physiol,* vol. 280, pp. H835-43, Feb 2001.

[6] C. A. Milano, L. F. Allen, H. A. Rockman, P. C. Dolber, T. R. McMinn, K. R. Chien*, et al.*, "Enhanced myocardial function in transgenic mice overexpressing the beta 2-adrenergic receptor," *Science,* vol. 264, pp. 582-6, Apr 22 1994.

[7] P. Carmeliet and D. Collen, "Transgenic mouse models in angiogenesis and cardiovascular disease," *The Journal of pathology,* vol. 190, pp. 387-405, 2000.

[8] F. H. Epstein, "MR in mouse models of cardiac disease," *NMR in Biomedicine,* vol. 20, pp. 238-255, 2007.

[9] C. J. Goergen, K. N. Barr, D. T. Huynh, J. R. Eastham-Anderson, G. Choi, M. Hedehus*, et al.*, "In vivo quantification of murine aortic cyclic strain, motion, and curvature: implications for abdominal aortic aneurysm growth," *Journal of Magnetic Resonance Imaging,* vol. 32, pp. 847-858, 2010.

[10] S. Ogawa, D. W. Tank, R. Menon, J. M. Ellermann, S. G. Kim, H. Merkle*, et al.*, "Intrinsic signal changes accompanying sensory stimulation: functional brain mapping with magnetic resonance imaging," *Proc Natl Acad Sci U S A,* vol. 89, pp. 5951-5, Jul 1 1992.

[11] P. A. Bandettini, "Twenty years of functional MRI: the science and the stories," *Neuroimage,* vol. 62, pp. 575-88, Aug 15 2012.

[12] A. H. Andersen, Z. Zhang, T. Barber, W. S. Rayens, J. Zhang, R. Grondin*, et al.*, "Functional MRI studies in awake rhesus monkeys: methodological and analytical strategies," *J Neurosci Methods,* vol. 118, pp. 141-52, Aug 30 2002.

[13] P. D. Gamlin, M. K. Ward, M. S. Bolding, J. K. Grossmann, and D. B. Twieg, "Developing functional magnetic resonance imaging techniques for alert macaque monkeys," *Methods,* vol. 38, pp. 210-20, Mar 2006.

[14] J. B. Goense, K. Whittingstall, and N. K. Logothetis, "Functional magnetic resonance imaging of awake behaving macaques," *Methods,* vol. 50, pp. 178-88, Mar 2010.

[15] J. E. Joseph, D. K. Powell, A. H. Andersen, R. S. Bhatt, M. K. Dunlap, S. T. Foldes*, et al.*, "fMRI in alert, behaving monkeys: an adaptation of the human infant familiarization novelty preference procedure," *J Neurosci Methods,* vol. 157, pp. 10-24, Oct 15 2006.

[16] G. A. Keliris, A. Shmuel, S. P. Ku, J. Pfeuffer, A. Oeltermann, T. Steudel*, et al.*, "Robust controlled functional MRI in alert monkeys at high magnetic field: effects of jaw and body movements," *Neuroimage,* vol. 36, pp. 550-70, Jul 1 2007.

[17] N. K. Logothetis, H. Guggenberger, S. Peled, and J. Pauls, "Functional imaging of the monkey brain," *Nat Neurosci,* vol. 2, pp. 555-62, Jun 1999.

[18] K. S. Murnane and L. L. Howell, "Development of an apparatus and methodology for conducting functional magnetic resonance imaging (fMRI) with pharmacological stimuli in conscious rhesus monkeys," *J Neurosci Methods,* vol. 191, pp. 11-20, Aug 15 2010.

[19] J. Pfeuffer, A. Shmuel, G. A. Keliris, T. Steudel, H. Merkle, and N. K. Logothetis, "Functional MR imaging in the awake monkey: effects of motion on dynamic off-resonance and processing strategies," *Magn Reson Imaging,* vol. 25, pp. 869-82, Jul 2007.

[20] S. Boretius, B. Schmelting, T. Watanabe, D. Merkler, R. Tammer, B. Czeh*, et al.*, "Monitoring of EAE onset and progression in the common marmoset monkey by sequential high-resolution 3D MRI," *NMR Biomed,* vol. 19, pp. 41-9, Feb 2006.

[21] B. Demain, C. Davoust, B. Plas, F. Bolan, K. Boulanouar, L. Renaud*, et al.*, "Corticospinal Tract Tracing in the Marmoset with a Clinical Whole-Body 3T Scanner Using Manganese-Enhanced MRI," *PLoS One,* vol. 10, p. e0138308, 2015.

[22] R. Diem, I. Demmer, S. Boretius, D. Merkler, B. Schmelting, S. K. Williams*, et al.*, "Autoimmune optic neuritis in the common marmoset monkey: comparison of

visual evoked potentials with MRI and histopathology," *Invest Ophthalmol Vis Sci,* vol. 49, pp. 3707-14, Aug 2008.

[23] E. Garea-Rodriguez, C. Schlumbohm, B. Czeh, J. Konig, G. Helms, C. Heckmann*, et al.*, "Visualizing dopamine transporter integrity with iodine-123-FP-CIT SPECT in combination with high resolution MRI in the brain of the common marmoset monkey," *J Neurosci Methods,* vol. 210, pp. 195-201, Sep 30 2012.

[24] G. Helms, E. Garea-Rodriguez, C. Schlumbohm, J. Konig, P. Dechent, E. Fuchs*, et al.*, "Structural and quantitative neuroimaging of the common marmoset monkey using a clinical MRI system," *J Neurosci Methods,* vol. 215, pp. 121-31, Apr 30 2013.

[25] C. Hung, J. Day-Cooney, B. Russ, C. Yen, L. Notardonato, A. Silva*, et al.*, "Neural responses to naturalistic movies in the common marmoset using electrocorticography and fMRI," *J Vis,* vol. 15, p. 580, 2015.

[26] C. C. Hung, C. C. Yen, J. L. Ciuchta, D. Papoti, N. A. Bock, D. A. Leopold*, et al.*, "Functional MRI of visual responses in the awake, behaving marmoset," *Neuroimage,* vol. 120, pp. 1-11, Oct 15 2015.

[27] J. V. Liu, Y. Hirano, G. C. Nascimento, B. Stefanovic, D. A. Leopold, and A. C. Silva, "fMRI in the awake marmoset: somatosensory-evoked responses, functional connectivity, and comparison with propofol anesthesia," *Neuroimage,* vol. 78, pp. 186-95, Sep 2013.

[28] J. D. Newman, W. M. Kenkel, E. C. Aronoff, N. A. Bock, M. R. Zametkin, and A. C. Silva, "A combined histological and MRI brain atlas of the common marmoset monkey, Callithrix jacchus," *Brain Res Rev,* vol. 62, pp. 1-18, Dec 11 2009.

[29] J. R. Tenney, P. C. Marshall, J. A. King, and C. F. Ferris, "fMRI of generalized absence status epilepticus in conscious marmoset monkeys reveals corticothalamic activation," *Epilepsia,* vol. 45, pp. 1240-7, Oct 2004.

[30] G. A. Johnson, G. P. Cofer, B. Fubara, S. L. Gewalt, L. W. Hedlund, and R. R. Maronpot, "Magnetic resonance histology for morphologic phenotyping," *Journal of Magnetic Resonance Imaging,* vol. 16, pp. 423-429, 2002.

[31] A. Kumar, W. A. Edelstein, and P. A. Bottomley, "Noise figure limits for circular loop MR coils," *Magn Reson Med,* vol. 61, pp. 1201-9, May 2009.

[32] G. R. Duensing, H. R. Brooker, and J. R. Fitzsimmons, "Maximizing signal-to-noise ratio in the presence of coil coupling," *J Magn Reson B,* vol. 111, pp. 230-5, Jun 1996.

[33] M. A. Ohliger and D. K. Sodickson, "An introduction to coil array design for parallel MRI," *NMR Biomed,* vol. 19, pp. 300-15, May 2006.

[34] K. P. Pruessmann, M. Weiger, P. Bornert, and P. Boesiger, "Advances in sensitivity encoding with arbitrary k-space trajectories," *Magn Reson Med,* vol. 46, pp. 638-51, Oct 2001.

[35] K. P. Pruessmann, M. Weiger, M. B. Scheidegger, and P. Boesiger, "SENSE: sensitivity encoding for fast MRI," *Magn Reson Med,* vol. 42, pp. 952-62, Nov 1999.

[36] C. Findeklee, "Array noise matching—generalization, proof and analogy to power matching," *IEEE Transactions on Antennas and Propagation,* vol. 59, pp. 452-459, 2011.

[37] P. Roemer, W. Edelstein, C. Hayes, S. Souza, and O. Mueller, "The NMR phased array," *Magnetic resonance in medicine,* vol. 16, pp. 192-225, 1990.

[38] W. Schnell, W. Renz, M. Vester, and H. Ermert, "Ultimate signal-to-noise-ratio of surface and body antennas for magnetic resonance imaging," *IEEE Transactions on Antennas and Propagation,* vol. 48, pp. 418-428, 2000.

[39] J. Wang, A. Reykowski, and J. Dickas, "Calculation of the signal-to-noise ratio for simple surface coils and arrays of coils," *IEEE Trans Biomed Eng,* vol. 42, pp. 908-17, Sep 1995.

[40] S. M. Wright and L. L. Wald, "Theory and application of array coils in MR spectroscopy," *NMR in Biomedicine,* vol. 10, pp. 394-410, 1997.

[41] W. G. Duan Q, Zhang B, Lattanzi R, Stoeckel B, Sodickson DK., "SNR benefits of surface coil lift-off at high magnetic field strength," *Proceedings of the 17th Scientific Meeting of ISMRM; Honolulu, Hawaii, USA. 2009. ,* p. Abstract 4742, 2009.

[42] C. E. Hayes and L. Axel, "Noise performance of surface coils for magnetic resonance imaging at 1.5 T," *Med Phys,* vol. 12, pp. 604-7, Sep-Oct 1985.

[43] B. Keil and L. L. Wald, "Massively parallel MRI detector arrays," *J Magn Reson,* vol. 229, pp. 75-89, Apr 2013.

[44] E. L. Green, "Biology of the laboratory mouse," *Biology of the laboratory mouse,* 1966.

[45] C. R. Schnell and J. M. Wood, "Measurement of blood pressure and heart rate by telemetry in conscious unrestrained marmosets," *Lab Anim,* vol. 29, pp. 258-61, Jul 1995.

[46] Z. J. Bosnjak, A. Aggarwal, L. A. Turner, J. M. Kampine, and J. P. Kampine, "Differential effects of halothane, enflurane, and isoflurane on Ca2+ transients and papillary muscle tension in guinea pigs," *Anesthesiology,* vol. 76, pp. 123-31, Jan 1992.

[47] T. J. Connelly and R. Coronado, "Activation of the Ca2+ release channel of cardiac sarcoplasmic reticulum by volatile anesthetics," *Anesthesiology,* vol. 81, pp. 459-69, Aug 1994.

[48] C. Y. Hart, J. C. Burnett, Jr., and M. M. Redfield, "Effects of avertin versus xylazine-ketamine anesthesia on cardiac function in normal mice," *Am J Physiol Heart Circ Physiol,* vol. 281, pp. H1938-45, Nov 2001.

[49] Y. Matsuda, K. Ohsaka, H. Yamamoto, K. Jiyouraku, K. Natsume, S. Hirabayashi, *et al.*, "NARCOBIT: a newly developed inhalational anesthesia system for mice," *Exp Anim,* vol. 56, pp. 131-7, Apr 2007.

[50] S. T. Ohnishi, C. A. DiCamillo, M. Singer, and H. L. Price, "Correlation between halothane-induced myocardial depression and decreases in La3+-displaceable Ca2+ in cardiac muscle cells," *J Cardiovasc Pharmacol,* vol. 2, pp. 67-75, Jan-Feb 1980.

[51] P. S. Pagel, J. P. Kampine, W. T. Schmeling, and D. C. Warltier, "Influence of volatile anesthetics on myocardial contractility in vivo: desflurane versus isoflurane," *Anesthesiology,* vol. 74, pp. 900-7, May 1991.

[52] H. L. Price and S. T. Ohnishi, "Effects of anesthetics on the heart," *Fed Proc,* vol. 39, pp. 1575-9, Apr 1980.

[53] G. Szczesny, A. Veihelmann, S. Massberg, D. Nolte, and K. Messmer, "Long-term anaesthesia using inhalatory isoflurane in different strains of mice-the haemodynamic effects," *Lab Anim,* vol. 38, pp. 64-9, Jan 2004.

[54] C. Constantinides, R. Mean, and B. J. Janssen, "Effects of isoflurane anesthesia on the cardiovascular function of the C57BL/6 mouse," *ILAR J,* vol. 52, pp. e21-31, 2011.

[55] D. Attwell, A. M. Buchan, S. Charpak, M. Lauritzen, B. A. Macvicar, and E. A. Newman, "Glial and neuronal control of brain blood flow," *Nature,* vol. 468, pp. 232-43, Nov 11 2010.

[56] C. Iadecola, "Neurovascular regulation in the normal brain and in Alzheimer's disease," *Nat Rev Neurosci,* vol. 5, pp. 347-60, May 2004.

[57] D. Kleinfeld, P. Blinder, P. J. Drew, J. D. Driscoll, A. Muller, P. S. Tsai*, et al.*, "A guide to delineate the logic of neurovascular signaling in the brain," *Front Neuroenergetics,* vol. 3, p. 1, 2011.

[58] M. Lauritzen, "Relationship of spikes, synaptic activity, and local changes of cerebral blood flow," *J Cereb Blood Flow Metab,* vol. 21, pp. 1367-83, Dec 2001.

[59] K. Masamoto and I. Kanno, "Anesthesia and the quantitative evaluation of neurovascular coupling," *J Cereb Blood Flow Metab,* vol. 32, pp. 1233-47, Jul 2012.

[60] P. M. Cornett, J. A. Matta, and G. P. Ahern, "General anesthetics sensitize the capsaicin receptor transient receptor potential V1," *Mol Pharmacol,* vol. 74, pp. 1261-8, Nov 2008.

[61] S. Lambert, M. Arras, K. E. Vogt, and U. Rudolph, "Isoflurane-induced surgical tolerance mediated only in part by beta3-containing GABA(A) receptors," *Eur J Pharmacol,* vol. 516, pp. 23-7, May 23 2005.

[62] Y. Sato, N. Seo, and E. Kobayashi, "Genetic background differences between FVB and C57BL/6 mice affect hypnotic susceptibility to pentobarbital, ketamine and nitrous oxide, but not isoflurane," *Acta Anaesthesiol Scand,* vol. 50, pp. 553-6, May 2006.

[63] B. Chance, G. R. Williams, and G. Hollunger, "Inhibition of electron and energy transfer in mitochondria. I. Effects of Amytal, thiopental, rotenone, progesterone, and methylene glycol," *J Biol Chem,* vol. 238, pp. 418-31, Jan 1963.

[64] S. Kohro, Q. H. Hogan, Y. Nakae, M. Yamakage, and Z. J. Bosnjak, "Anesthetic effects on mitochondrial ATP-sensitive K channel," *Anesthesiology,* vol. 95, pp. 1435-340, Dec 2001.

[65] H. Rottenberg, "Uncoupling of oxidative phosphorylation in rat liver mitochondria by general anesthetics," *Proc Natl Acad Sci U S A,* vol. 80, pp. 3313-7, Jun 1983.

[66] M. A. Pisauro, N. T. Dhruv, M. Carandini, and A. Benucci, "Fast hemodynamic responses in the visual cortex of the awake mouse," *J Neurosci,* vol. 33, pp. 18343-51, Nov 13 2013.

[67] K. Clarke and L. Hall, "A survey of anaesthesia in small animal practice: AVA/BSAVA report," *Veterinary Anaesthesia and Analgesia,* vol. 17, pp. 4-10, 1990.

[68] D. Sawyer, K. Aziz, C. Backinger, E. Beers, A. Lowery, and S. Sykes, "An introduction to human factors in medical devices," *US Department of Health and Human Services, Public Health Service, Food and Drug Administration, Center for Devices and Radiological Health,* 1996.

[69] D. Cattano, C. Young, M. M. Straiko, and J. W. Olney, "Subanesthetic doses of propofol induce neuroapoptosis in the infant mouse brain," *Anesth Analg,* vol. 106, pp. 1712-4, Jun 2008.

[70] G. Liang, C. Ward, J. Peng, Y. Zhao, B. Huang, and H. Wei, "Isoflurane causes greater neurodegeneration than an equivalent exposure of sevoflurane in the developing brain of neonatal mice," *Anesthesiology,* vol. 112, pp. 1325-34, Jun 2010.

[71] W. Slikker, Jr., X. Zou, C. E. Hotchkiss, R. L. Divine, N. Sadovova, N. C. Twaddle*, et al.*, "Ketamine-induced neuronal cell death in the perinatal rhesus monkey," *Toxicol Sci,* vol. 98, pp. 145-58, Jul 2007.

[72] I. Vanzetta and A. Grinvald, "Coupling between neuronal activity and microcirculation: implications for functional brain imaging," *HFSP J,* vol. 2, pp. 79-98, Apr 2008.

[73] A. Villringer and U. Dirnagl, "Coupling of brain activity and cerebral blood flow: basis of functional neuroimaging," *Cerebrovasc Brain Metab Rev,* vol. 7, pp. 240-76, Fall 1995.

[74] K. M. Lahti, C. F. Ferris, F. Li, C. H. Sotak, and J. A. King, "Imaging brain activity in conscious animals using functional MRI," *J Neurosci Methods,* vol. 82, pp. 75-83, Jul 1 1998.

[75] K. M. Lahti, C. F. Ferris, F. Li, C. H. Sotak, and J. A. King, "Comparison of evoked cortical activity in conscious and propofol-anesthetized rats using functional MRI," *Magn Reson Med,* vol. 41, pp. 412-6, Feb 1999.

[76] J. Berwick, C. Martin, J. Martindale, M. Jones, D. Johnston, Y. Zheng*, et al.*, "Hemodynamic response in the unanesthetized rat: intrinsic optical imaging and spectroscopy of the barrel cortex," *J Cereb Blood Flow Metab,* vol. 22, pp. 670-9, Jun 2002.

[77] C. Martin, J. Berwick, D. Johnston, Y. Zheng, J. Martindale, M. Port*, et al.*, "Optical imaging spectroscopy in the unanaesthetised rat," *J Neurosci Methods,* vol. 120, pp. 25-34, Oct 15 2002.

[78] C. D. Harvey, F. Collman, D. A. Dombeck, and D. W. Tank, "Intracellular dynamics of hippocampal place cells during virtual navigation," *Nature,* vol. 461, pp. 941-6, Oct 15 2009.

[79] C. E. Hayes, "Radio frequency field coil for NMR," ed: Google Patents, 1987.

[80] C. E. Hayes, W. A. Edelstein, J. F. Schenck, O. M. Mueller, and M. Eash, "An efficient, highly homogeneous radiofrequency coil for whole-body NMR imaging at 1.5 T," *Journal of Magnetic Resonance (1969),* vol. 63, pp. 622-628, 1985.

[81] T. Vullo, R. T. Zipagan, R. Pascone, J. P. Whalen, and P. T. Cahill, "Experimental design and fabrication of birdcage resonators for magnetic resonance imaging," *Magnetic resonance in medicine,* vol. 24, pp. 243-252, 1992.

[82] J. Tropp, "The theory of the bird-cage resonator," *Journal of Magnetic Resonance (1969),* vol. 82, pp. 51-62, 1989.

[83] M. C. Leifer, "Resonant modes of the birdcage coil," *Journal of Magnetic Resonance,* vol. 124, pp. 51-60, 1997.

[84] C. L. Chin, C. M. Collins, S. Li, B. J. Dardzinski, and M. B. Smith, "BirdcageBuilder: Design of specified-geometry birdcage coils with desired current pattern and resonant frequency," *Concepts in Magnetic Resonance,* vol. 15, pp. 156-163, 2002.

[85] D. I. Hoult and R. Richards, "The signal-to-noise ratio of the nuclear magnetic resonance experiment," *Journal of Magnetic Resonance (1969),* vol. 24, pp. 71-85, 1976.

[86] L. Darrasse and J.-C. Ginefri, "Perspectives with cryogenic RF probes in biomedical MRI," *Biochimie,* vol. 85, pp. 915-937, 2003.

[87] G. C. Wiggins, J. R. Polimeni, A. Potthast, M. Schmitt, V. Alagappan, and L. L. Wald, "96-Channel receive-only head coil for 3 Tesla: Design optimization and evaluation," *Magnetic Resonance in Medicine,* vol. 62, pp. 754-762, 2009.

[88] V. J. Wedeen, R. E. Wendt, and M. Jerosch-Herold, "Motional phase artifacts in Fourier transform MRI," *Magnetic Resonance in Medicine,* vol. 11, pp. 114-120, 1989.

[89] L. Axel, R. Summers, H. Kressel, and C. Charles, "Respiratory effects in two-dimensional Fourier transform MR imaging," *Radiology,* vol. 160, pp. 795-801, 1986.

[90] P. G. Schmidt and E. N. Smith, "Physiological monitoring during NMR measurements of animals," *Journal of Magnetic Resonance (1969),* vol. 54, pp. 480-485, 1983.

[91] L.-G. Lindberg, H. Ugnell, and P. Öberg, "Monitoring of respiratory and heart rates using a fibre-optic sensor," *Medical and Biological Engineering and Computing,* vol. 30, pp. 533-537, 1992.

[92] C. K. McKibben and N. V. Reo, "A piezoelectric respiratory monitor for in vivo NMR," *Magnetic resonance in medicine,* vol. 27, pp. 338-342, 1992.

[93] N. G. Burdett, T. Adrian Carpenter, and L. D. Hall, "A simple device for respiratory gating for the MRI of laboratory animals," *Magnetic resonance imaging,* vol. 11, pp. 897-901, 1993.

[94] S. J. Wilson, I. M. Brereton, P. Hockings, W. Roffmann, and D. M. Doddrell, "Respiratory triggered imaging with an optical displacement sensor," *Magnetic resonance imaging,* vol. 11, pp. 1027-1032, 1993.

[95] S. K. Lemieux and G. H. Glover, "An infrared device for monitoring the respiration of small rodents during magnetic resonance imaging," *Journal of Magnetic Resonance Imaging,* vol. 6, pp. 561-564, 1996.

[96] K. R. Minard, R. A. Wind, and R. L. Phelps, "A compact respiratory-triggering device for routine microimaging of laboratory mice," *Journal of Magnetic Resonance Imaging,* vol. 8, pp. 1343-1348, 1998.

[97] S. E. Slawson, B. B. Roman, D. S. Williams, and A. P. Koretsky, "Cardiac MRI of the normal and hypertrophied mouse heart," *Magnetic resonance in medicine,* vol. 39, pp. 980-987, 1998.

[98] E. Rommel, J. Kuhstrebe, F. Wiesmann, M. Szimtenings, J. Streif, and A. Haase, "A double trigger unit for ECG and breath triggered mouse heart imaging," *MAGMA,* vol. 11, p. 568, 2000.

[99] K. W. Fishbein, P. McConville, and R. G. Spencer, "The lever-coil: a simple, inexpensive sensor for respiratory and cardiac motion in MRI experiments," *Magnetic resonance imaging,* vol. 19, pp. 881-889, 2001.

[100] A. Brau, C. T. Wheeler, L. W. Hedlund, and G. A. Johnson, "Fiber-optic stethoscope: A cardiac monitoring and gating system for magnetic resonance microscopy," *Magnetic resonance in medicine,* vol. 47, pp. 314-321, 2002.

[101] P. J. Cassidy, J. E. Schneider, S. M. Grieve, C. Lygate, S. Neubauer, and K. Clarke, "Assessment of motion gating strategies for mouse magnetic resonance at high

magnetic fields," *Journal of Magnetic Resonance Imaging,* vol. 19, pp. 229-237, 2004.

[102] R. L. Ehman and J. Felmlee, "Adaptive technique for high-definition MR imaging of moving structures," *Radiology,* vol. 173, pp. 255-263, 1989.

[103] Y. Wang, P. J. Rossman, R. C. Grimm, S. J. Riederer, and R. L. Ehman, "Navigator-echo-based real-time respiratory gating and triggering for reduction of respiration effects in three-dimensional coronary MR angiography," *Radiology,* vol. 198, pp. 55-60, 1996.

[104] O. Dietrich, T. Lanz, H. Reinl, F. Berger, M. Peller, M. Reiser*, et al.*, "Parallel imaging of mice on a clinical 3-Tesla MRI system with a dedicated 8-channel small-animal coil array," in *Proceedings 15th Scientific Meeting, International Society for Magnetic Resonance in Medicine*, Berlin, Germany, 2007, p. 1759.

[105] D. Gareis, T. Wichmann, T. Lanz, G. Melkus, M. Horn, and P. M. Jakob, "Mouse MRI using phased-array coils," *NMR Biomed,* vol. 20, pp. 326-34, May 2007.

[106] T. Lanz, M. Muller, H. Barnes, S. Neubauer, and J. E. Schneider, "A high-throughput eight-channel probe head for murine MRI at 9.4 T," *Magn Reson Med,* vol. 64, pp. 80-7, Jul 2010.

[107] M. S. Ramirez, E. Esparza-Coss, and J. A. Bankson, "Multiple-mouse MRI with multiple arrays of receive coils," *Magn Reson Med,* vol. 63, pp. 803-10, Mar 2010.

[108] M. S. Ramirez, S. Y. Lai, and J. A. Bankson, "A throughput-optimized array system for multiple-mouse MRI," *NMR Biomed,* vol. 26, pp. 237-47, Mar 2013.

[109] J. Wang, N. Tian, F. Robb, A. Chen, L. Friesen-Waldner, B. Rutt*, et al.*, "An 8-channel coil array for small animal 13C MR imaging," in *Proceedings 18th Scientific Meeting, International Society for Magnetic Resonance in Medicine*, Stockholm, Sweden, 2010, p. 1489.

[110] B. Keil, G. C. Wiggins, C. Triantafyllou, L. L. Wald, F. M. Meise, L. M. Schreiber*, et al.*, "A 20-channel receive-only mouse array coil for a 3 T clinical MRI system," *Magnetic Resonance in Medicine,* vol. 66, pp. 582-593, 2011.

[111] H. Merkle, J. Liu, Y. Hirano, and A. Silva, "A multi-element receive coil array for MRI/fMRI of awake behaving marmosets," in *Proceedings of the Joint Annual Meeting ISMRM-ESMRMB*, 2010, p. 3852.

[112] D. Papoti, C. C. Yen, J. B. Mackel, H. Merkle, and A. C. Silva, "An embedded four-channel receive-only RF coil array for fMRI experiments of the

somatosensory pathway in conscious awake marmosets," *NMR Biomed,* vol. 26, pp. 1395-402, Nov 2013.

[113] J. Davies, "Some aspects of the physiology of the anaesthetised marmoset," *Laboratory Animals,* vol. 3, pp. 151-156, 1969.

[114] M. S. Cohen, R. M. Weisskoff, R. R. Rzedzian, and H. L. Kantor, "Sensory stimulation by time-varying magnetic fields," *Magn Reson Med,* vol. 14, pp. 409-14, May 1990.

[115] C. L. Ham, J. M. Engels, G. T. van de Wiel, and A. Machielsen, "Peripheral nerve stimulation during MRI: effects of high gradient amplitudes and switching rates," *J Magn Reson Imaging,* vol. 7, pp. 933-7, Sep-Oct 1997.

[116] A. Hoffmann, S. C. Faber, K. J. Werhahn, L. Jager, and M. Reiser, "Electromyography in MRI--first recordings of peripheral nerve activation caused by fast magnetic field gradients," *Magn Reson Med,* vol. 43, pp. 534-9, Apr 2000.

[117] D. I. Hoult, C. N. Chen, and V. J. Sank, "The field dependence of NMR imaging. II. Arguments concerning an optimal field strength," *Magn Reson Med,* vol. 3, pp. 730-46, Oct 1986.

[118] D. K. Sodickson and W. J. Manning, "Simultaneous acquisition of spatial harmonics (SMASH): fast imaging with radiofrequency coil arrays," *Magn Reson Med,* vol. 38, pp. 591-603, Oct 1997.

[119] M. A. Griswold, P. M. Jakob, R. M. Heidemann, M. Nittka, V. Jellus, J. Wang*, et al.*, "Generalized autocalibrating partially parallel acquisitions (GRAPPA)," *Magn Reson Med,* vol. 47, pp. 1202-10, Jun 2002.

[120] F. A. Breuer, M. Blaimer, R. M. Heidemann, M. F. Mueller, M. A. Griswold, and P. M. Jakob, "Controlled aliasing in parallel imaging results in higher acceleration (CAIPIRINHA) for multi-slice imaging," *Magn Reson Med,* vol. 53, pp. 684-91, Mar 2005.

[121] F. A. Breuer, M. Blaimer, M. F. Mueller, N. Seiberlich, R. M. Heidemann, M. A. Griswold*, et al.*, "Controlled aliasing in volumetric parallel imaging (2D CAIPIRINHA)," *Magn Reson Med,* vol. 55, pp. 549-56, Mar 2006.

[122] W. Edelstein, C. Hardy, and O. Mueller, "Electronic decoupling of surface-coil receivers for NMR imaging and spectroscopy," *Journal of Magnetic Resonance (1969),* vol. 67, pp. 156-161, 1986.

[123] K. Moody, N. Hollingsworth, N. J-F, D. Noll, S. Wright, and M. McDougall, "RF transparent array for testing multi-channel transmit systems," in *Proceedings 18th*

Scientific Meeting, International Society for Magnetic Resonance in Medicine,, Stockholm, Sweden, 2010.

[124] M. P. McDougall, D. G. Brown, D. Spence, and S. M. Wright, "A low-pass trombone birdcage coil with broad tuning range," in *Proceedings 9th Scientific Meeting, International Society for Magnetic Resonance in Medicine*, Glasgow, Scotland, UK, 2001.

[125] Y. Xu and P. Tang, "Easy fabrication of a tunable high-pass birdcage resonator," *Magnetic resonance in medicine,* vol. 38, pp. 168-172, 1997.

[126] J. Jin, *Electromagnetic analysis and design in magnetic resonance imaging* vol. 1: CRC press, 1998.

[127] D. K. Spence and S. M. Wright, "2-D full wave solution for the analysis and design of birdcage coils," *Concepts in Magnetic Resonance Part B: Magnetic Resonance Engineering,* vol. 18, pp. 15-23, 2003.

[128] W. Y. Chiang and M. P. McDougall, "Geometric decoupling of a mouse array coil using a dual plane pair design with crisscrossed return paths and custom mounting fixture," *Conf Proc IEEE Eng Med Biol Soc,* vol. 2014, pp. 1394-7, 2014.

[129] L. Darrasse and G. Kassab, "Quick measurement of NMR-coil sensitivity with a dual-loop probe," *Review of scientific instruments,* vol. 64, pp. 1841-1844, 1993.

[130] S. M. Wright and M. P. McDougall, "Single echo acquisition MRI using RF encoding," *Nmr in Biomedicine,* vol. 22, pp. 982-993, Nov 2009.

[131] N. Kishi, K. Sato, E. Sasaki, and H. Okano, "Common marmoset as a new model animal for neuroscience research and genome editing technology," *Dev Growth Differ,* vol. 56, pp. 53-62, Jan 2014.

[132] H. Okano, K. Hikishima, A. Iriki, and E. Sasaki, "The common marmoset as a novel animal model system for biomedical and neuroscience research applications," *Semin Fetal Neonatal Med,* vol. 17, pp. 336-40, Dec 2012.

[133] S. G. Solomon and M. G. Rosa, "A simpler primate brain: the visual system of the marmoset monkey," *Front Neural Circuits,* vol. 8, p. 96, 2014.

[134] D. H. Abbott, D. K. Barnett, R. J. Colman, M. E. Yamamoto, and N. J. Schultz-Darken, "Aspects of common marmoset basic biology and life history important for biomedical research," *Comp Med,* vol. 53, pp. 339-50, Aug 2003.

[135] E. Leibovitch, J. E. Wohler, S. M. Cummings Macri, K. Motanic, E. Harberts, M. I. Gaitan*, et al.*, "Novel marmoset (Callithrix jacchus) model of human

Herpesvirus 6A and 6B infections: immunologic, virologic and radiologic characterization," *PLoS Pathog,* vol. 9, p. e1003138, Jan 2013.

[136] S. Ohta, Y. Ueda, M. Yaguchi, Y. Matsuzaki, M. Nakamura, Y. Toyama*, et al.*, "Isolation and characterization of dendritic cells from common marmosets for preclinical cell therapy studies," *Immunology,* vol. 123, pp. 566-74, Apr 2008.

[137] D. Papoti, C. C. Yen, C. C. Hung, J. Ciuchta, D. A. Leopold, and A. C. Silva, "Design and implementation of embedded 8-channel receive-only arrays for whole-brain MRI and fMRI of conscious awake marmosets," *Magn Reson Med,* Aug 8 2016.

[138] A. C. Silva, J. V. Liu, Y. Hirano, R. F. Leoni, H. Merkle, J. B. Mackel*, et al.*, "Longitudinal functional magnetic resonance imaging in animal models," *Methods Mol Biol,* vol. 711, pp. 281-302, 2011.

[139] P. A. Yushkevich, J. Piven, H. C. Hazlett, R. G. Smith, S. Ho, J. C. Gee*, et al.*, "User-guided 3D active contour segmentation of anatomical structures: significantly improved efficiency and reliability," *Neuroimage,* vol. 31, pp. 1116-28, Jul 1 2006.

[140] A. Haase, J. Frahm, D. Matthaei, W. Hanicke, and K.-D. Merboldt, "FLASH imaging. Rapid NMR imaging using low flip-angle pulses," *Journal of Magnetic Resonance (1969),* vol. 67, pp. 258-266, 1986.

[141] J. Hennig, A. Nauerth, and H. Friedburg, "RARE imaging: a fast imaging method for clinical MR," *Magnetic resonance in medicine,* vol. 3, pp. 823-833, 1986.

[142] G. C. Wiggins, C. Triantafyllou, A. Potthast, A. Reykowski, M. Nittka, and L. L. Wald, "32-channel 3 Tesla receive-only phased-array head coil with soccer-ball element geometry," *Magn Reson Med,* vol. 56, pp. 216-23, Jul 2006.

[143] D. Seeber, J. Jevtic, and A. Menon, "Floating shield current suppression trap," *Concepts in Magnetic Resonance Part B: Magnetic Resonance Engineering,* vol. 21, pp. 26-31, 2004.

[144] A. Reykowski, S. M. Wright, and J. R. Porter, "Design of matching networks for low noise preamplifiers," *Magn Reson Med,* vol. 33, pp. 848-52, Jun 1995.

[145] K. Fujiyoshi, M. Yamada, M. Nakamura, J. Yamane, H. Katoh, K. Kitamura*, et al.*, "In vivo tracing of neural tracts in the intact and injured spinal cord of marmosets by diffusion tensor tractography," *J Neurosci,* vol. 27, pp. 11991-8, Oct 31 2007.

[146] A. Iwanami, J. Yamane, H. Katoh, M. Nakamura, S. Momoshima, H. Ishii*, et al.*, "Establishment of graded spinal cord injury model in a nonhuman primate: the common marmoset," *J Neurosci Res,* vol. 80, pp. 172-81, Apr 15 2005.

[147] S. Lacroix, L. A. Havton, H. McKay, H. Yang, A. Brant, J. Roberts*, et al.*, "Bilateral corticospinal projections arise from each motor cortex in the macaque monkey: a quantitative study," *J Comp Neurol,* vol. 473, pp. 147-61, May 24 2004.

[148] R. N. Lemon, P. A. Kirkwood, M. A. Maier, K. Nakajima, and P. Nathan, "Direct and indirect pathways for corticospinal control of upper limb motoneurons in the primate," *Prog Brain Res,* vol. 143, pp. 263-79, 2004.

[149] Y. Qiu, Y. Wada, E. Otomo, and H. Tsukagoshi, "Morphometric study of cervical anterior horn cells and pyramidal tracts in medulla oblongata and the spinal cord in patients with cerebrovascular diseases," *J Neurol Sci,* vol. 102, pp. 137-43, Apr 1991.

[150] T. Terashima, T. Ochiishi, and T. Yamauchi, "Immunohistochemical detection of calcium/calmodulin-dependent protein kinase II in the spinal cord of the rat and monkey with special reference to the corticospinal tract," *J Comp Neurol,* vol. 340, pp. 469-79, Feb 22 1994.

[151] T. Konomi, K. Fujiyoshi, K. Hikishima, Y. Komaki, O. Tsuji, H. J. Okano*, et al.*, "Conditions for quantitative evaluation of injured spinal cord by in vivo diffusion tensor imaging and tractography: preclinical longitudinal study in common marmosets," *Neuroimage,* vol. 63, pp. 1841-53, Dec 2012.

[152] L. Massacesi, C. P. Genain, D. Lee-Parritz, N. L. Letvin, D. Canfield, and S. L. Hauser, "Active and passively induced experimental autoimmune encephalomyelitis in common marmosets: a new model for multiple sclerosis," *Ann Neurol,* vol. 37, pp. 519-30, Apr 1995.

[153] A. Iwanami, S. Kaneko, M. Nakamura, Y. Kanemura, H. Mori, S. Kobayashi*, et al.*, "Transplantation of human neural stem cells for spinal cord injury in primates," *J Neurosci Res,* vol. 80, pp. 182-90, Apr 15 2005.

[154] J. Picus, W. R. Aldrich, and N. L. Letvin, "A naturally occurring bone-marrow-chimeric primate. I. Integrity of its immune system," *Transplantation,* vol. 39, pp. 297-303, Mar 1985.

[155] D. D. Ralston and H. J. Ralston, 3rd, "The terminations of corticospinal tract axons in the macaque monkey," *J Comp Neurol,* vol. 242, pp. 325-37, Dec 15 1985.

[156] Y. Kobayashi, Y. Okada, G. Itakura, H. Iwai, S. Nishimura, A. Yasuda*, et al.*, "Pre-evaluated safe human iPSC-derived neural stem cells promote functional recovery

after spinal cord injury in common marmoset without tumorigenicity," *PLoS One,* vol. 7, p. e52787, 2012.

[157] J. Yamane, M. Nakamura, A. Iwanami, M. Sakaguchi, H. Katoh, M. Yamada*, et al.*, "Transplantation of galectin-1-expressing human neural stem cells into the injured spinal cord of adult common marmosets," *J Neurosci Res,* vol. 88, pp. 1394-405, May 15 2010.

[158] M. Yaguchi, M. Tabuse, S. Ohta, K. Ohkusu-Tsukada, T. Takeuchi, J. Yamane*, et al.*, "Transplantation of dendritic cells promotes functional recovery from spinal cord injury in common marmoset," *Neurosci Res,* vol. 65, pp. 384-92, Dec 2009.

[159] B. G. Nichols and E. Zepeda, "Quadrature imaging of the lumbar spine using a "table-top" mounted tranceiver and a surface coil receive only RF coil at 0.35 Tesla," *Society of Magnetic Resonance in Medicine, 7th annual meeting, San Francisco, California, USA.,* p. 260, August 20-26, 1988 1988.

[160] C. C. Guclu, E. Boskamp, T. Zheng, R. Becerra, and L. Blawat, "A method for preamplifier-decoupling improvement in quadrature phased-array coils," *J Magn Reson Imaging,* vol. 19, pp. 255-8, Feb 2004.

[161] K. Fouad, I. Klusman, and M. E. Schwab, "Regenerating corticospinal fibers in the Marmoset (Callitrix jacchus) after spinal cord lesion and treatment with the anti-Nogo-A antibody IN-1," *Eur J Neurosci,* vol. 20, pp. 2479-82, Nov 2004.

[162] B. J. Kelley, N. Y. Harel, C. Y. Kim, X. Papademetris, D. Coman, X. Wang*, et al.*, "Diffusion tensor imaging as a predictor of locomotor function after experimental spinal cord injury and recovery," *J Neurotrauma,* vol. 31, pp. 1362-73, Aug 1 2014.

[163] J. Picus, K. Holley, W. R. Aldrich, J. D. Griffin, and N. L. Letvin, "A naturally occurring bone marrow-chimeric primate. II. Environment dictates restriction on cytolytic T lymphocyte-target cell interactions," *J Exp Med,* vol. 162, pp. 2035-52, Dec 01 1985.

[164] M. J. McAuliffe, F. M. Lalonde, D. McGarry, W. Gandler, K. Csaky, and B. L. Trus, "Medical image processing, analysis and visualization in clinical research," in *Computer-Based Medical Systems, 2001. CBMS 2001. Proceedings. 14th IEEE Symposium on*, 2001, pp. 381-386.

[165] C. Watson, G. Sengul, I. Tanaka, Z. Rusznak, and H. Tokuno, "The spinal cord of the common marmoset (Callithrix jacchus)," *Neurosci Res,* vol. 93, pp. 164-75, Apr 2015.

[166] C. Casteleyn, J. Bakker, S. Breugelmans, I. Kondova, J. Saunders, J. A. Langermans*, et al.*, "Anatomical description and morphometry of the skeleton of the common marmoset (Callithrix jacchus)," *Lab Anim,* vol. 46, pp. 152-63, Apr 2012.

[167] M. Arras, P. Autenried, A. Rettich, D. Spaeni, and T. Rulicke, "Optimization of intraperitoneal injection anesthesia in mice: drugs, dosages, adverse effects, and anesthesia depth," *Comp Med,* vol. 51, pp. 443-56, Oct 2001.

[168] C. J. Green, *Animal anaesthesia*: Laboratory Animals Ltd., c/o Biochemical Society Book Depot, PO Box 32., 1979.